2017

Advanced Microscopy of Thermoelectric Materials

Jacob Byrnes
University of Wollongong

Advanced Microscopy of Thermoelectric Materials

A thesis completed as an important part of a postgraduate student's exposure to advanced experimental techniques and the scientific approach to research.

Submitted in fulfilment of the requirements for the award of the degree

MASTER OF PHILOSOPHY (MATERIALS ENGINEERING)

From

UNIVERSITY OF WOLLONGONG (UOW)

By

JACOB BYRNES

AUSTRALIAN INSTITUTE FOR INNOVATIVE MATERIALS (AIIM)

2017

CERTIFICATION

I, Jacob B. Byrnes, declare that this thesis, submitted in fulfilment of the requirements for the award of Master of Philosophy, in the Faculty of Engineering and Information Sciences, University of Wollongong, is completely my own work unless otherwise referenced or acknowledged. This document has not been submitted for qualifications at any other academic institution.

(Signature) Jacob Byrnes

Date

Acknowledgements

I'd first like to thank my supervisor Dr. Sima Aminorroaya-Yamini. When I first met Sima during my undergraduate years it was clear that she had an absolute passion for high quality research. From the moment I joined Sima's group she has continued to be a source of inspiration and guidance. Whenever I felt lost or unsure about any aspect of my project, a quick meeting with Sima was all it took to get me back on track. I'd similarly like to thank my co-supervisor, Dr. David Mitchell. Of course, David offered fantastic insight into the world of microscopy. But more importantly to me, he reassured me and gave me confidence that the path I'd chosen for my future was the right choice. For that I will forever be grateful.

Without a doubt I owe a great deal to the staff at the Electron Microscopy Centre; Mitchell Nancarrow, Azdiar Gazder, Tony Romeo and Gilberto Casillas. These men have continued to mentor me and given me the necessary skills to continue my future in microscopy. I had a fantastic time working in the EMC labs, and I like to think they didn't mind me bothering them all the time either. Without the team at the EMC I certainly wouldn't have segued into my career as smoothly as I have. Thank you.

To my colleagues (and great friends) in the thermoelectrics group; Rafael Santos, Andrew Manettas, Xavier Reales and Vaughan Patterson. These guys are responsible for teaching me the ins and outs of thermoelectrics. They were always there to help me with problems in and out of the lab space. Their great sense of humour, brutal honesty and willingness to help out whenever needed is certainly a core reason as to how I've made it this far. I hope each of you find your way in the future and that we make sure to stay in contact. I need some tour guides in Spain and Portugal, Xavi and Raf!

Finally, I must thank my family and friends for always being the supportive backbone that every research student needs. I often fall victim to believing I can handle everything on my own, but I know without your support I would've had great difficulty achieving my goals. I owe a great deal to my mother and father, who have supported my choices every step of the way. To my beautiful fiancé Keziah, I honestly don't know where I'd be without you. You are my rock, my counsellor, my motivator and my inspiration. Thank you for always believing in me and always pushing me to achieve the highest standard I'm capable of.

Abstract

Thermoelectric (TE) materials, capable of harvesting waste heat and converting this into electricity, have shown promise for use in power generation and refrigeration. The application of TE materials to energy hungry processes, such as the operation of combustion engines or industrial furnaces, provides an opportunity to improve the efficiency of our energy economy. The TE properties, and hence TE figure of merit (zT) of these materials can correlate strongly with the microstructural features of the material. The microstructure of TE materials is heavily related to the fabrication method employed, with further exposure to heat often causing evolution in the microstructure of the material. In order to understand how the observed microstructure of a TE material relates to its measured TE properties, various electron microscopy techniques can be employed.

This thesis investigates the application of advanced electron microscopy on the understanding of TE materials through the presentation of two case studies.

The primary case study presented utilises a suite of electron microscopy techniques to investigate the long term thermal stability of the microstructure in a recently developed high performance *p*-type quaternary lead chalcogenide $Pb_{0.97}Na_{0.03}Te_{0.65}S_{0.25}Se_{0.1}$, and discusses how this relates to the evolving TE properties of the material. When thermally aged at 823 K (simulating TE device operational temperatures) for up to 8 weeks, the TE efficiency of the alloy proved to be stable with a zT of ~1.7-1.9. The presence of nanoscale precipitates after 1-2 weeks of thermal ageing proved to have little impact on the thermal conductivity of the alloy. Dissolution of precipitates and redistribution of dopant between phases is understood to explain the increasing resistivity observed for samples with increasing thermal ageing time. Advanced electron microscopy was suitably used to gain a thorough understanding of the evolving microstructure in $Pb_{0.97}Na_{0.03}Te_{0.65}S_{0.25}Se_{0.1}$, proving its suitability for device application in correlation with TE property measurements.

The secondary case study presented focuses on the optimisation of a phase segmentation methodology capable of distinguishing the structurally similar yet chemically unique phases of Bi_2Te_3 and Bi_2Te_2S in the TE alloy system $Bi_2Te_{2.5}S_{0.5}$. Conventional electron backscatter diffraction spectroscopy (EBSD), capable of full characterisation of texture in anisotropic materials, typically segments phases based on differences in crystal structures present in the investigated phases. The phase segmentation methodology presented is comprehensively assessed, with key considerations required during its application discussed in detail. Segmented phase maps of Bi_2Te_3 and Bi_2Te_2S obtained via the optimised phase

segmentation methodology achieve an absolute error of ~5% in relation to a reference phase map, providing a reliable strategy to facilitate texture analysis in multiphase TE materials. This case study highlights the importance of continually developing and improving the methods we use to investigate the microstructures of these systems.

Table of Contents

List of Figures

phase distribution map of Bi_2Te_3 (black) and Bi_2Te_2S (white). In (c), LAGBs = silver, HAGBs = black. The map in (d) is the reference phase map used to calculate the absolute error in the phase map obtained from segmentation (Fig. 5.2e) on a per-pixel basis.

Figure 5.2: An example workflow for phase discrimination via segmentation. (a) The TIFF image of the map of relative distribution of sulphur-K counts imported into Gatan DigitalMicrograph. (b) Greyscaling of the image in (a). (c) Interactive thresholding between 200 and 255, binarising and inverting the contrast of the image in (b). (d) Applying a local neighbourhood density threshold of 1 white pixel in a 3×3 neighbourhood matrix of 8 first neighbour pixels to the image in (c). (e) Applying a median filter of size 3 to the image in (d). (f) Re-assigning white and black pixels as red (Bi_2Te_3) and blue (Bi_2Te_2S) for qualitative comparison with Fig. 5.1c. In (f), LAGBs = silver, HAGBs = black.

Figure 5.3: (a) The resultant absolute difference image obtained from Fig. 1d (the reference phase map) and Fig. 2e (the phase map from segmentation) on using the 'Image Calculator' function in ImageJ. (b) Zoomed-in views of regions highlighted in red in Figs. 1d (far left) and 2e (middle) that result in the absolute difference image (far right). The absolute difference image (far right) returns black pixels when the images on the far left and middle are equivalent and white pixels when they differ.

Figure 5.4: (a) A zoomed-in view of a region taken from the binarised reference phase map shown in Fig. 1d. (b, c) The equivalent region when a neighbourhood density threshold of 1, no dilation kernel, and a 5×5 and 7×7 neighbourhood matrix size are respectively used for phase segmentation. (d-f) The equivalent region when a 3×3 neighbourhood matrix size, no dilation kernel and a neighbourhood density threshold of 1, 2 and 3 are respectively used for phase segmentation. (g) The equivalent region when a neighbourhood density threshold of 3, a 3×3 neighbourhood matrix size and a dilation kernel size of 3 is used for phase segmentation. (h, i) The equivalent region when a neighbourhood density threshold of 1, a 3×3 neighbourhood matrix size and a dilation kernel size of 3 and 5 are respectively used for phase segmentation. A median of size 3 was applied to all maps shown.

List of Tables

List of Abbreviations

TE	Thermoelectric
XRD	X-ray Diffraction
SPS	Spark Plasma Sintering
LFA	Laser Flash Apparatus
LM	Light Microscopy
SEM	Scanning Electron Microscopy
TEM	Transmission Electron Microscopy
HRTEM	High Resolution Transmission Electron Microscopy
STEM	Scanning Transmission Electron Microscopy
FIB	Focussed Ion Beam
EBSD	Electron Backscatter Diffraction Spectroscopy
EDS	Energy Dispersive X-ray Spectroscopy
SAED	Selected Area Electron Diffraction
HAADF	High Angle Annular Dark-Field
DOS	Density of States
LAGB	Low Angle Grain Boundary
HAGB	High Angle Grain Boundary
zT	Thermoelectric figure of merit
α	Seebeck Coefficient
σ	Electrical Conductivity
ρ	Electrical Resistivity
κ_T	Total Thermal Conductivity
κ_E	Electronic thermal conductivity
κ_L	Lattice thermal conductivity
D_T	Thermal Diffusivity

Cp	Specific Heat Capacity
L	Lorenz Number
η	Conversion efficiency

Chapter 1

Introduction

The dependence of society on non-renewable fossil fuels for power generation has inspired research into clean and renewable energy resources. One approach to improving the sustainability of our generated electricity is to recover waste heat and convert it to electricity using thermoelectric (TE) generators. This is beneficial for improving the efficiency of energy hungry processes, such as the operation of internal combustion engines or industrial processes. TEs have long shown promise, but have been deemed too cost inefficient in many applications [1]. In recent years, the efficiencies of TE materials have steadily increased with a focus on optimising doping [2-4], alloying [5-7] and the introduction of nanoscale features to enhance TE performance [8-10]. Advanced microscopy has proven to be a useful tool in characterising TE materials [10, 11] and correlating dynamic structures with the properties of TEs [12, 13].

The aim of this project is to utilise advanced microscopy as a means to better understand the significance of structural inhomogeneity and nanostructures on the performance of TE materials. Two case studies are presented. The primary case study utilises analysis from light microscopy, scanning electron microscopy and transmission electron microscopy to correlate the microstructural properties of lead chalcogenides to their TE transport properties. The secondary case study instead presents and investigates the efficacy of a methodology designed to segment structurally similar phases for texture analysis via electron backscatter diffraction spectroscopy (EBSD). The former case study presents a case where advanced microscopy is utilised to further our understanding of TE systems, while the latter case study highlights the importance of continually developing and improving the methods we use to investigate the microstructures of these systems. Together these case studies highlight the importance of advanced microscopy for the ongoing research and development of high performance TE materials.

Chapters 2 first provides an overview of relevant concepts related to TE materials and key considerations when aiming to optimise the performance of TE materials. Comprehensive review of the strategies employed to enhance the performance of lead chalcogenides is then presented. Emphasis is placed on literature investigating the influence of nanostructuring on the performance of lead chalcogenides. This chapter is concluded with review of the key techniques in advanced microscopy employed to investigate TE materials.

Chapter 3 outlines the experimental procedures employed to fabricate and characterise the lead chalcogenide samples investigated in the primary case study. Techniques employed to measure the transport properties and analyse the microstructure of samples are described in terms of samples preparation and collection of relevant data.

The primary case study, presented in Chapter 4, investigates the change in TE performance of multiphase quaternary lead chalcogenides when thermally aged post fabrication (simulating TE device operational conditions). The microstructure of lead chalcogenide samples is comprehensively investigated to correlate observed changes in TE performance with the evolution of sample microstructure after 1 week, 2 weeks, 4 weeks and 8 weeks of thermal ageing at 823 K.

The secondary case study, presented in Chapter 5, investigates a methodology capable of discriminating structurally analogous phases for texture analysis via EBSD. The methodology is applied to the TE alloy $Bi_2Te_{2.5}S_{0.5}$ to segment the structurally similar yet chemically unique phases of Bi_2Te_3 and Bi_2Te_2S. The methodology is comprehensively assessed, with key considerations required when applying the methodology discussed in detail.

The thesis is concluded in Chapter 6.

Chapter 2

Literature Review

2.1 Thermoelectric Phenomena

TE properties are described by multiple phenomena. The Seebeck Effect describes the generation of electricity through an applied thermal gradient between dissimilar conducting materials. Contrary to this is the Peltier Effect, which describes the flow of phonons through a TE material when exposed to a potential difference [17].

2.1.2 The Seebeck Effect

The Seebeck effect is the result of thermal gradients across dissimilar conductors which give rise to an electrostatic potential (voltage). The phenomenon was first observed in 1821 by Thomas Johann Seebeck, who demonstrated the production of a voltage by introducing a thermal gradient across a junction between a pair of different electrical conductors [4, 18, 19]. Consider a module containing an *n*-type and a *p*-type semiconductor in electrical contact, as in Fig. 2.1a. When heat is applied to the semiconductor junction, the thermal energy of mobile charge carriers in the system are greater on the hot side of the module causing diffusion of charge carriers towards the cold side. This is analogous to the flow of electrons in a metal. This results in a build-up of electrons (e^-) at the cold end, or a net charge, which is responsible for producing a voltage. The process is reversible, meaning the flow of charge carriers is reversed if the temperature gradient is applied in the opposite direction. This phenomenon is the basis for TE power generation.

The Seebeck coefficient, α, is a material property defined by the magnitude of an induced voltage generated in an open circuit in direct response to a thermal gradient, as in Equation 2.1:

$$\alpha = \frac{\Delta V}{\Delta T} \tag{2.1}$$

2.1.3 The Peltier Effect

The Peltier effect is analogous to the Seebeck effect, though describes the heat differential generated when a voltage is supplied across dissimilar conductors [4, 18, 19]. We can again describe the phenomena if we consider two degenerate semiconductors in electrical contact, as in Fig. 2.1b. When a voltage is applied across the two conductors, heat is transferred with the movement of charge carriers from one junction to the other, cooling one junction and heating the other. This behaviour was first observed in 1834 by Jean Peltier.

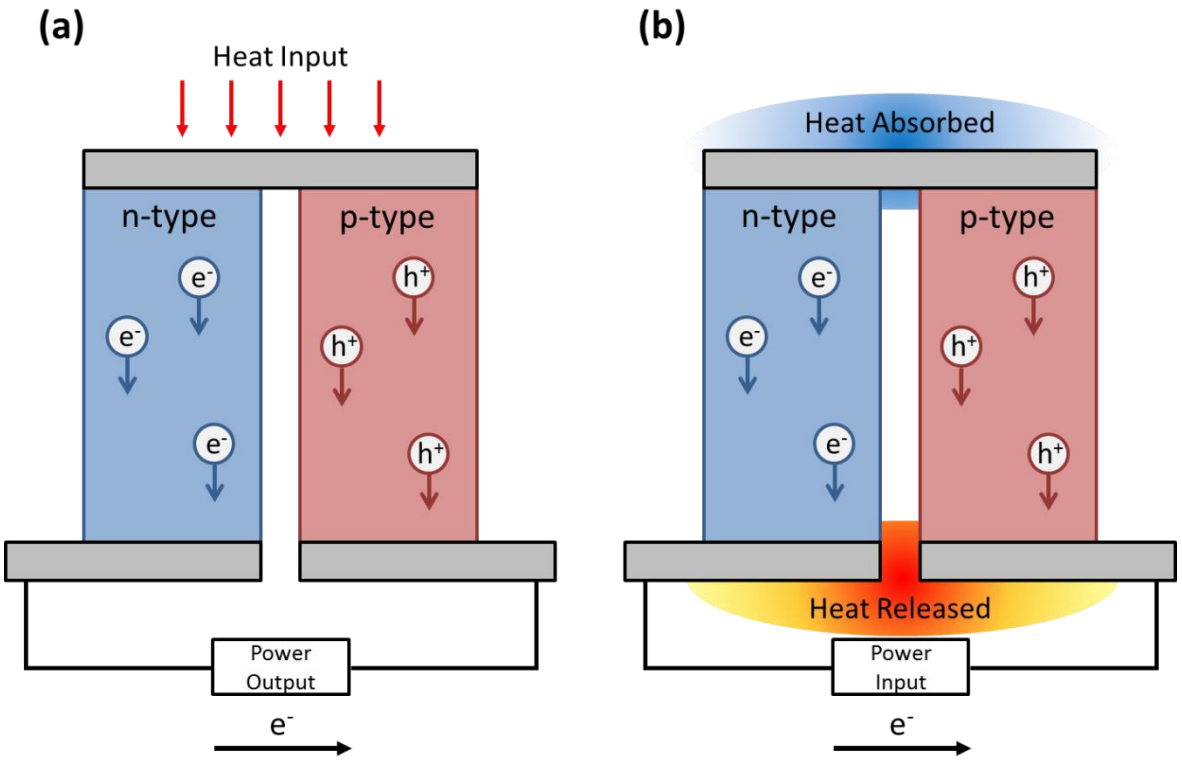

Figure 2.1: (a) Mobile charge carriers in a circuit containing dissimilar conductors (such as n-type and p-type semiconductors) diffuse from the hot junction to the cold junction when heat is applied to the system. *N*-type semiconductors contribute electrons to the system and *p*-type semiconductors contribute holes. (b) If a voltage is instead applied to the same system, the movement of charge carriers provides a temperature differential between the two junctions. This results in Peltier cooling or heating.

2.2 Thermoelectric Devices

TE devices are particularly appealing for energy recovery applications due to the relative simplicity of their design, requiring no moving parts and operating in silence. They are an environmentally friendly device that emits no hazardous waste during operation [20]. Further, TE devices have been successfully employed to provide power to the space probe *Voyager* in both terrestrial and extra-terrestrial settings. For such applications, solar radiance is too low to permit the use of solar panels [18]. While having many appealing traits, TE devices have seen limited use due to their low conversion efficiency. The efficiency of a device is directly related to the figure of merit (zT) the TE material:

$$\eta = \eta_c \frac{\sqrt{1+ZT}-1}{\sqrt{1+ZT}+T_c/T_h} \qquad 2.2$$

where η is the conversion efficiency of heat to electricity, T_c and T_h are the temperatures of the cold and hot sides of the device respectively, and η_c is the Carnot efficiency ($\eta_c = 1 - T_c/T_h$) [19, 20].

Doped semiconductors are the primary candidates for the functional material in a TE device. A typical TE couple (Fig. 2.2) consists of an *n*-type TE (rich in negative charge carriers) and a *p*-type TE (rich in positive charge carriers) connected via metallic contacts. A TE device consists of a large array of TE couples arranged electrically in series and thermally in parallel [19].

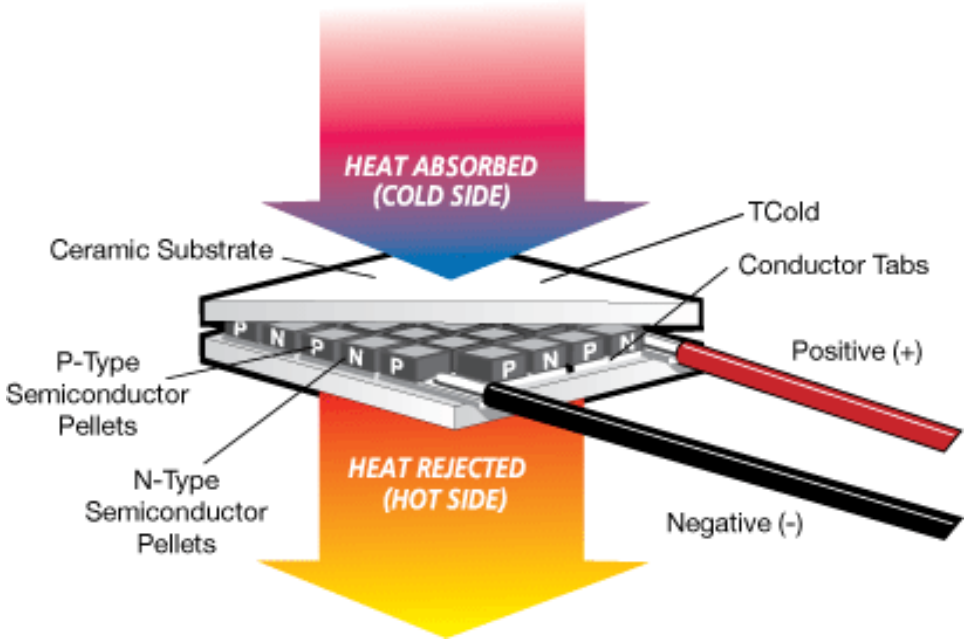

Figure 2.2: An example of a commercial TE module [1].

TE devices utilise TE phenomena differently depending on the application. When a temperature gradient is applied on either side of the device, the device is capable of recovering and converting waste heat into electricity due to the Seebeck effect. This effect also provides the basis for temperature sensing via thermocouples. Converse to this, the Peltier effect is utilised by supplying a potential difference across the devices, providing active cooling to one side [18, 21]. The operation temperature of a device dictates its application, and the operation temperature is dependent on the TE material chosen.

2.3 Thermoelectric Materials

The application of a TE material is best determined by its temperature range of operation. Fig. 2.3 shows the temperature dependent zT of the most common classes of TEs. At

low temperature ranges of up to 500 K, Bi_2Te_3 alloys demonstrate the best performance. These alloys are well studied, and have seen use in commercial Peltier cooling devices [4]. Lead chalcogenides show most promise as midrange temperature TEs, with *z*Ts typically peaking at ~600-900 K. High temperature TEs that show peak performance at temperatures over 1200 K are typically silicon-germanium alloys.

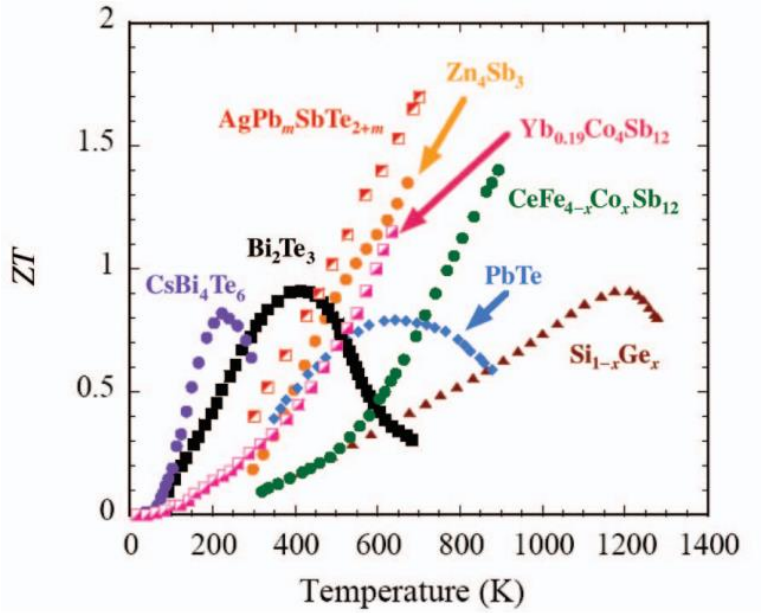

Figure 2.3: Temperature dependent *z*T of several bulk TE materials [2].

Fig. 2.4 expands upon the details shown in Fig. 2.3, making note of the most significant improvements to *z*T made since the year 2000 for bulk TEs. Of particular interest are the many lead chalcogenide alloys reaching *z*Ts ~2. Lead chalcogenides are particularly appealing for waste heat recovery in the automobile industry due to their peak *z*Ts coinciding with typical operation temperatures of internal combustion engines.[4] The following section will describe the methods used to optimise the *z*T of lead chalcogenides in detail.

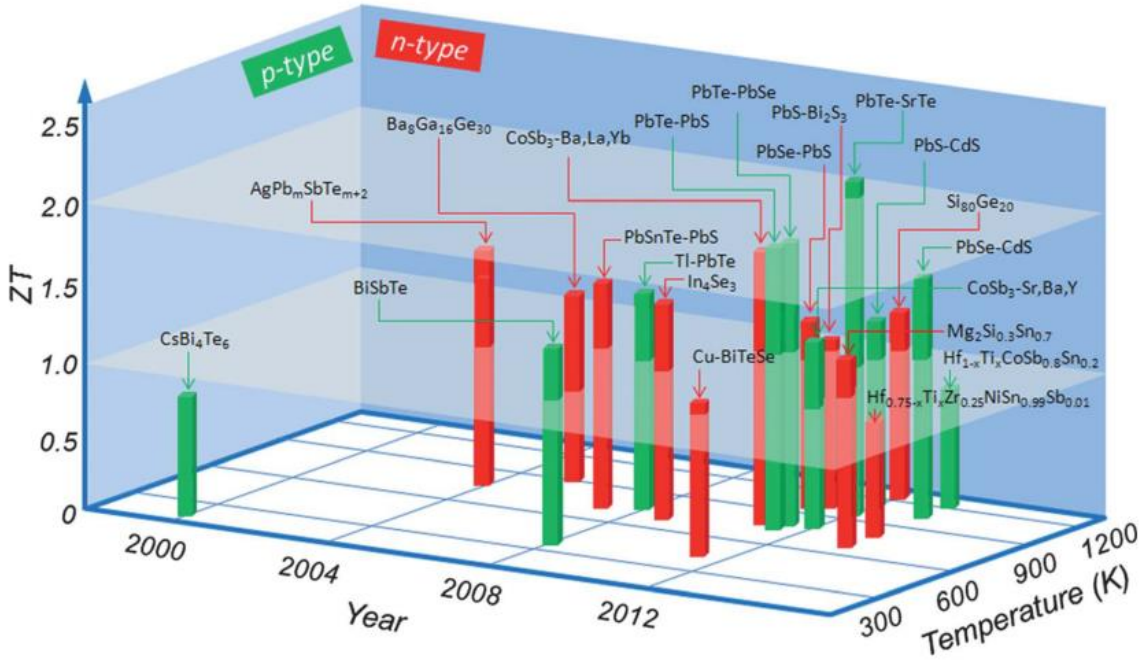

Figure 2.4: The many classes of bulk TE materials with their highest achieved zT, the year it was achieved and the temperature at which it was measured. Both n-type and p-type TEs are included [3].

2.4 Optimising Thermoelectric Materials

2.4.1 Maximising the conversion efficiency of thermoelectric materials

The performance of a TE device is directly related to the TE material of choice. To assess the potential of a material for TE applications, a dimensionless figure of merit (zT) is used [4]. The zT considers the Seebeck coefficient (α), electrical conductivity (σ) and the thermal conductivity (κ) of the material:

$$zT = \frac{\alpha^2 \sigma}{\kappa} T \qquad 2.3$$

Improving the zT of a material is a challenging task due to the conflicting nature of materials properties that must be optimised. In order to do so, the thermopower (absolute value of the Seebeck coefficient) and electrical conductivity must be improved while limiting the thermal conductivity of a material. Due to the conflicting nature of materials properties that need optimisation, a careful balance must be achieved between each. Fig. 2.5 highlights how the Seebeck coefficient, electrical conductivity and thermal conductivity are balanced with respect to carrier concentration to achieve high zTs in Bi_2Te_3 (though the concept applies similarly to all TE materials) [4].

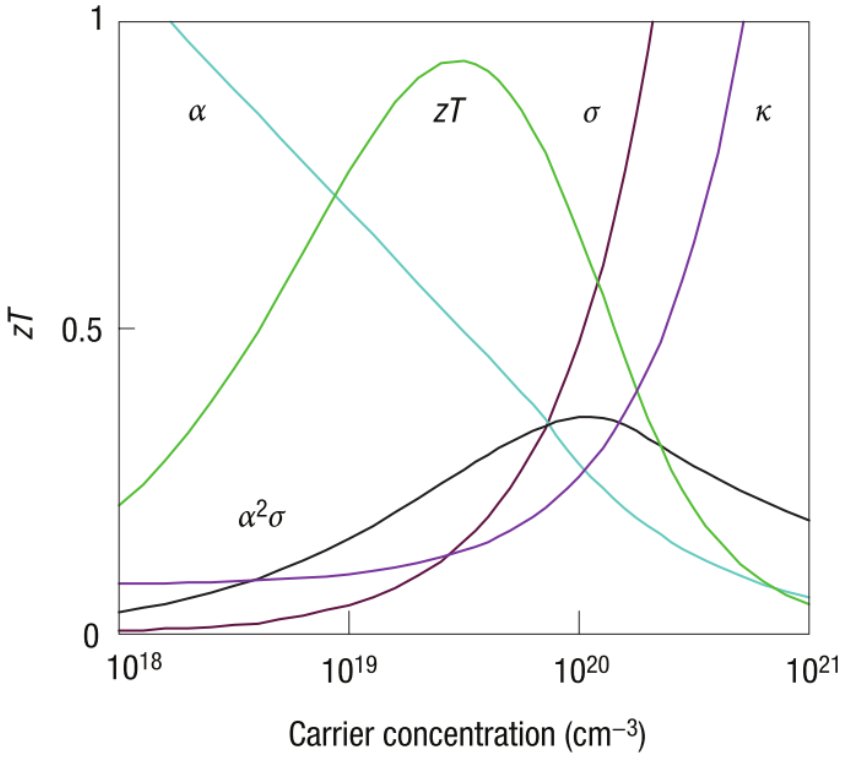

Figure 2.5: Optimising *z*T through carrier concentration tuning. A balance must be achieved between thermal conductivity and Seebeck coefficient with electrical conductivity. Good TE materials typically have carrier concentrations between 10^{19} and 10^{21} carriers/cm^3 [4].

2.4.2 Lead Chalcogenides

Lead chalcogenides have been understood for their potential in TE applications since the early 20th century [22]. Early semiconducting cooling units were made from PbTe and ZnSb, but were later replaced by Bi_2Te_3-type materials due to their higher efficiencies at lower temperatures. While Bi_2Te_3 has seen great success as a room temperature TE material [23, 24], lead chalcogenides demonstrate remarkable performance at a high temperature range (500-900 K) [25-27].

Lead chalcogenides have been desirable TE materials due to their exceptional base TE performance. They have NaCl structured face centred cubic crystals, with lattice constants of 5.94, 6.12 and 6.50 Å and densities of 7.61, 8.27 and 8.24 gcm^{-2} for PbS, PbSe and PbTe respectively [22, 28]. Lead chalcogenides exhibit low thermal conductivities at high temperatures, which has been attributed to strongly anharmonic lattice dynamics, large cation disorder [29, 30] and thermally induced lattice distortions [31], each of which contribute phonon-scattering mechanisms. The temperature dependent electronic band structure for PbTe

is shown in Fig. 2.6 and consists of two valence bands, the light-hole band and lower energy heavy-hole band at the *L* and Σ points of the Brillouin zone, respectively. At high temperatures the two bands converge, allowing the heavy-hole band to contribute to conduction. PbS and PbSe bare similar band structures, and can influence the position of the bands when alloyed with PbTe. The red and blue lines in Fig. 2.6 represent a shift of the light and heavy-hole valence bands to lower energies when alloyed with PbS. This complex structure and the contribution of a high density of states (DOS) heavy-hole band are understood to be responsible for the naturally high Seebeck coefficient of lead chalcogenides [32, 33].

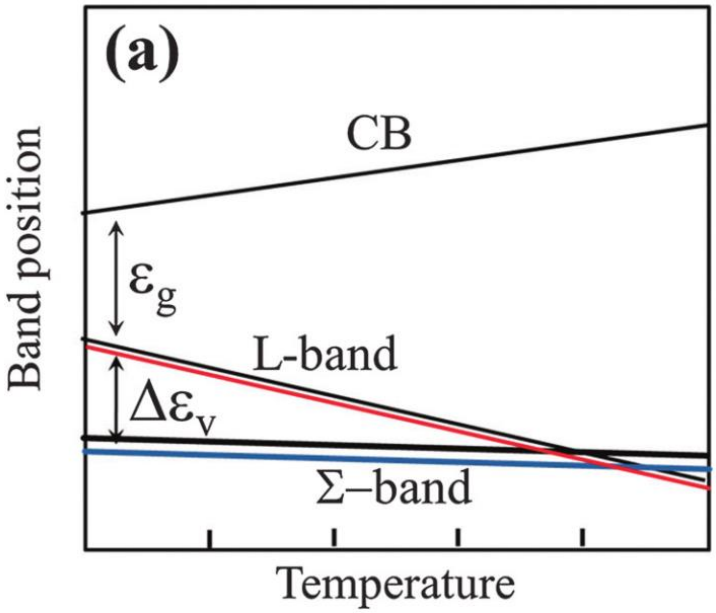

Figure 2.6: Temperature dependent band energies of the conduction band, the light and heavy-hole valence bands for PbTe. ε_g shows the room temperature band gap and $\Delta\varepsilon_v$ shows the energy offset between the light and heavy valence bands. The red and blue lines show the valence bands shift to lower energies when alloyed with PbS [5].

2.4.3 Optimising carrier concentration (doping) of Lead Chalcogenides

Carrier concentration is typically tuned through doping with impurities. Dopants introduced to PbQ (Q = S, Se, Te) substitutes with Pb^{2+} or Q^{2-}, causing *n*-type or *p*-type conduction depending on the valence of the dopant and the replaced atom. Enhanced charge carrier concentration is desirable for enhancing electric conductivity though, as previously described, is not without limitations. At high dopant concentrations the Fermi level can be altered such that the Seebeck coefficient is reduced and the electrical conductivity amplified. Hence, carrier concentrations of 10^{19} – 10^{21} carriers per cm^3 are typically desirable for a good

TE [4]. The most common dopants used for lead chalcogenides and their achievable carrier concentrations are summarised in Table 2.1.

Table 2.1: Typical dopants used in lead chalcogenide TEs [2, 4, 34].

	Dopant	**Achievable Carrier Concentration in PbTe (cm^{-3})**
***n*-type**	Cl, Br, I	$\sim 2 \times 10^{20}$
	Bi, Sb	$\sim 10^{20}$
***p*-type**	Na, Li, Tl, K	$\sim 1.5 \times 10^{20}$

Several studies have focussed on enhancing the performance of single phase lead chalcogenides via both *n*-type and *p*-type doping. PbTe is known to have high TE performance when heavily doped, achieving *z*T's of ~1.4 and 1.2 for both *p*-type and *n*-type samples respectively [35-37]. Heavy doping of PbTe with sodium has been shown to enhance the Seebeck coefficient (with respect to *n*-type PbTe) due to a high density of states near the Fermi level, resulting in charge carrying holes with high effective mass [35]. This is possible due to the temperature dependence of the band offset between the light and heavy-hole valence bands. The energy of the light valence band is reduced with increasing temperature until it reaches the heavy hole band edge [5]. Above 400 K the heavy-hole band (higher density of states) becomes the main contributor of charge carriers, resulting in an enhanced Seebeck coefficient. This behaviour is not observed in *n*-type PbTe due to a lack of a heavy hole band, meaning the Seebeck coefficient is proportional to absolute temperature [38].

Single phase PbS and PbSe have also been shown to boast similar TE efficiencies to PbTe (maximum reported *z*Ts for *n*-type samples of ~0.8 [39] and ~1.2 [40] respectively). PbS and PbSe are cheaper and more abundant alternatives to PbTe, resulting in a strong effort to further understand and enhance the achievable *z*Ts for these compounds [39, 41]. One of the most promising approaches is to develop lead chalcogenide alloys.

2.4.4 Alloying Lead Chalcogenides

Alloying PbTe with PbS or PbSe has provided an effective means to limit the dependence on expensive tellurium while allowing further improvements in TE performance. Solid solutions of *n*-type $(PbTe)_{1-x}(PbSe)_x$ were prepared by Wang *et al.*[42] and were found to have a reduced thermal conductivity with respect to its constituents. PbSe is known to have unlimited solubility

in both PbS and PbTe [6]. When forming a solid solution with PbTe, atomic disorder produces scattering centres for phonons causing a reduction in lattice thermal conductivity. Consequently, the same disorder causes local potential energy fluctuations which scatter charge carriers, reducing mobility.

A high zT of ~1.8 has been achieved for Na-doped $PbTe_{1-x}Se_x$ by combining the effects of alloy scattering and valley degeneracy. It is believed that heavy Na doping of the alloy promotes convergence of the light and heavy-hole bands, allowing the heavy-hole band to contribute a higher DOS for conduction. The combination of mechanisms simultaneously enhancing electrical conductivity and thermopower while reducing the lattice thermal conductivity allowed a significant enhancement of the TE performance [43].

An alternative approach is to alloy PbTe with PbS. This pseudo-binary system shows very limited solubility and contains a continuous miscibility gap, of which a secondary phase can form via nucleation and growth or spinodal decomposition [6]. Fig. 2.7 shows that a solid solution forms above ~1075 K for all compositions. Engineering bulk PbTe-PbS compounds to form nanoprecipitates has been an appealing strategy to further reduce the lattice thermal conductivity and enhance TE performance [44-47]. This occurs due to the introduction of a secondary phase enhancing phonon scattering at grain boundaries. The influence of nanostructures on TE performance in $PbTe_{0.92}PbS_{0.08}$ has been investigated [9]. Solid solution samples were prepared by homogenising then quenching the melt. Nucleation of PbS precipitates was observed in the 400-500 K range, coinciding with an increase in electron mobility and concentration. This suggests a reduction in electrons scattered by ionised impurities with more electrons available for conduction. A reduction of lattice thermal conductivity by ~60% to ~0.4 W/mK was observed, suggesting nanostructuring was responsible for the improved performance.

The introduction of PbTe nanostructures into the PbS matrix has also been explored [48]. Enhancements of zT up to ~50% were achieved when compared to pure PbS for n-type $PbS_{0.97}PbTe_{0.03}$ (zT ~0.8 @ 910 K), with 16% reductions in lattice thermal conductivity. While not as significant as the improvements made for the $PbTe_{0.92}PbS_{0.08}$, it is a more cost effective alternative providing sufficient TE performance. PbS-PbSe alloys were also found to have some improvement in performance with the formation of PbS nanostructures [49], despite previous understanding that mutual unlimited solubility existed in this system [6]. The degree of performance enhancement due to nanostructuring was not as significant as that observed in the PbTe-PbS system, likely due to significant contributions of optical phonon excitations in PbSe and PbS, though a zT of ~1.3 was achieved at 900 K.

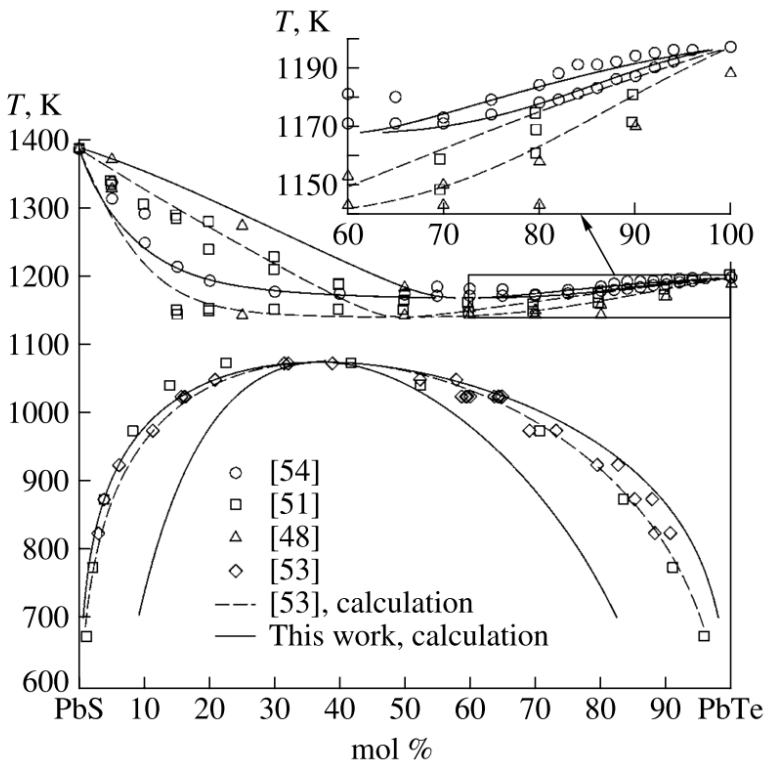

Figure 2.7: Phase diagram of the PbTe-PbS system [6].

A recent focus on quaternary lead chalcogenides (PbTe-PbSe-PbS systems) has allowed further optimization of zT in single phase alloys [5]. Alloying PbTe-PbS with PbSe increases the solubility limit of PbS in PbTe, allowing band gap tuning with PbSe, a larger DOS effective mass and a reduced lattice thermal conductivity due to phonon scattering at point defects. The Seebeck coefficient of *p*-type $PbTe_{0.85}PbSe_{0.1}PbS_{0.5}$ was also larger than its ternary analogues, and achieved a *z*T of ~ 1.6 at ~750 K. A later investigation [7] into nanostructured $(PbTe)_{0.65}(PbSe)_{0.1}(PbS)_{0.25}$ showed a loss in TE performance compared to the single phase compound at all temperatures. The lattice thermal conductivity of Na-doped $(PbTe)_{(0.9-x)}(PbSe)_{0.1}(PbS)_x$ for x = 0, 0.05, 0.1, 0.15, 0.2, and 0.25 are compared in Table 2.2. All compositions show similar lattice thermal conductivities at 850 K, suggesting that the measured low thermal conductivity is dominated by atomic mass contrast scattering and not the introduction of nanoprecipitates. The *z*T's of each composition are compared in Fig. 2.8, highlighting that the single phase compound (x = 0.05) outperforms the nanostructured compounds. Further analysis [50] of the precipitates took place via microscopy techniques to further elucidate this anomaly, and will be discussed in a later section.

Table 2.2: The total and lattice thermal conductivity of 1 at.% Na-doped $(PbTe)_{(0.9-x)}(PbSe)_{0.1}(PbS)_x$ for x = 0, 0.05, 0.1, 0.15, 0.2, and 0.25 at room temperature and 850 K. All values are in units W/mK [7].

Sample	Room-temperature lattice thermal conductivity	Room-temperature total thermal conductivity	Lattice thermal conductivity at 850 K
$x = 0$	1.4	3.3	0.7
$x = 0.05$	1.26	2.5	0.6
$x = 0.10$	1.2	2.3	0.6
$x = 0.15$	1.2	2.2	0.6
$x = 0.20$	1.4	2.3	0.6
$x = 0.25$	1.5	2.4	0.6

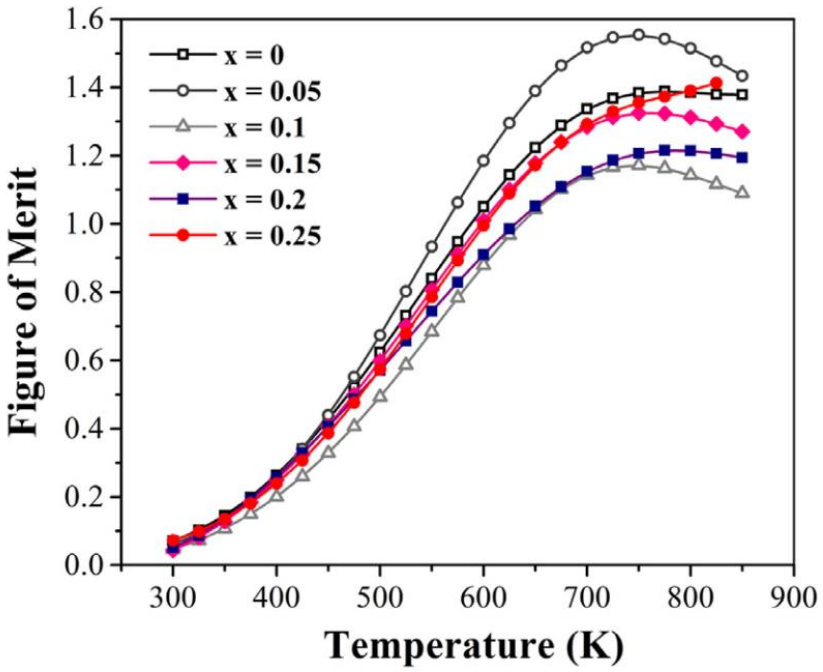

Figure 2.8: Temperature dependence of zT for 1 at.% Na-doped $(PbTe)_{(0.9-x)}(PbSe)_{0.1}(PbS)_x$ for x = 0, 0.05, 0.1, 0.15, 0.2, and 0.25 [7].

It is clear that multiple routes can be taken to optimise the performance of a TE material. Manipulating the composition of the lead alloy and selective doping are common means to improve zT through tuning the band structure [26]. Introducing nanostructures into bulk material is also a possibility, and has garnered much interest in recent years due to its ability to further reduce measured lattice thermal conductivity [14, 51, 52]. Combining the effects of alloying, doping and nanostructuring, an approach recently termed the panoscopic approach [53], can allow for simultaneous enhancement of the Seebeck coefficient and electrical

conductivity while limiting the thermal conductivity. As such, it is imperative to understand entirely how this approach influences each TE system and how best to adapt this approach for commercial use. Microscopy techniques are an essential tool that allows the assessment of precipitate growth and morphology, distribution of dopants between phases and analysis of strain fields from features such as grain boundaries and dislocations. The following section will detail progress made in understanding the complexities behind hierarchical TE design and the benefits and limitations of what has been explored.

2.5 Nanostructures in Bulk Thermoelectric Materials

2.5.1 Bulk Nanostructured Lead Chalcogenides

The field of TEs saw its first functioning devices come to fruition in the 1950's and 1960's [4]. Devices had an average ZT ~ 1.0, and are now considered 'first generation' TEs. These were deemed too inefficient to justify their use, causing research in the field to stagnate [3]. It was not until the mid-1990s when Dresselhaus proposed utilising quantum-well superlattice structures to enhance the zT of TE materials [54]. The idea of utilising nanostructured features to reduce the lattice thermal conductivity of TEs stimulated much experimental research in the coming decades. Of particular relevance to the lead chalcogenide family of TEs is the concept of purposely introducing nanoscale precipitates, defects and compositional inhomogeneity into the bulk material to enhance phonon scattering [7, 23, 46, 55, 56]. Unsurprisingly, recent experiments have utilised a knowledge of band engineering in tandem with nanostructuring to achieve reported zT's of up to 2.2 for *p*-type PbTe [57]. The thermal stability of a TE is as important as the performance in a commercial device, so it also important to consider the stability of these materials following TE measurements. Thermal treatment of these materials promotes diffusion of elements, which can compromise TE performance through growth of secondary phase precipitates or via diffusion of dopants between phases [11, 15]. Deliberate engineering of the dislocation structure also has potential if applied to lead chalcogenides, though needs further investigating to understand its significance [55].

The following section will investigate much of the recent progress made utilising nanostructuring in bulk lead chalcogenides and their derivatives. Particular attention will be payed to the composition and fabrication methods of the described experiments, to assess the feasibility of converting the compound into a device. Recent progress made to better understand diffusion processes and the influence of dislocations will also be considered.

2.5.2 Fabricating Nanostructured Materials

It has been explained above that nanostructuring of bulk TEs has shown enhancement of TE performance in some systems due to a reduction in lattice thermal conductivity. Scattering is typically caused by the interaction of phonons with strain fields introduced via point defects, interstitial atoms, anti-site defects, impurities and phase or grain boundaries [3, 8]. Phase boundaries are most commonly associated with scattering mid-to-long wavelength phonons, whereas point defects are more effective at scattering short wavelength phonons. Meso-scale grain boundaries effectively scatter long wavelength phonons, allowing a broader spectrum of phonon scattering if each type of phonon scattering mechanism is present. Fig. 2.9 shows the contributions to phonon scattering by atomic, nano and meso-scale structure on various phonon mean free paths in PbTe [8]. It suggests that 55% of the lattice thermal conductivity of PbTe is contributed by phonon modes with mean free paths from 5 to 100 nm, which are most effectively scattered by nanoparticles.

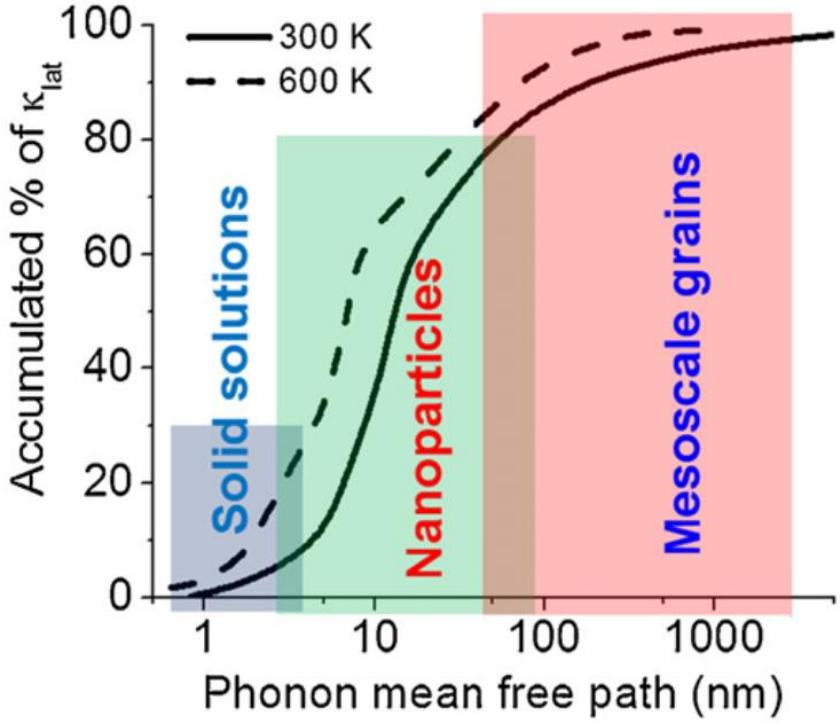

Figure 2.9: The percentage contribution of phonon mean free path to the lattice thermal conductivity of PbTe at 300 K and 600 K. Solid solution, nanoparticles and meso-scale grains effectively scatter phonons with short, medium and long mean free paths respectively [8].

Nanoscale precipitates can be introduced into bulk TEs by carefully controlling the composition and fabrication method of the TE material. Typically the secondary phase is introduced through nucleation and growth, though some have reported controlled spinodal

decomposition as a means to lower thermal conductivity [10]. For these cases the secondary phase must be completely soluble in the liquid state but have limited or no solubility in the solid state. When a melt is quenched rapidly, the secondary phase will precipitate if it exceeds the solid state solution limit. Here, the precipitation mechanism is explained by using the pseudo-binary system of PbTe-PbS as an example. Fig. 2.10a shows a ternary phase diagram for a system containing a continuous series of solid solutions between components A and B. This is analogous to the PbTe-PbS phase diagram shown in Fig. 2.10b. Fig. 2.10b highlights the phase separation mechanisms in the systems studied in Refs. [9] (blue) and [10] (red).

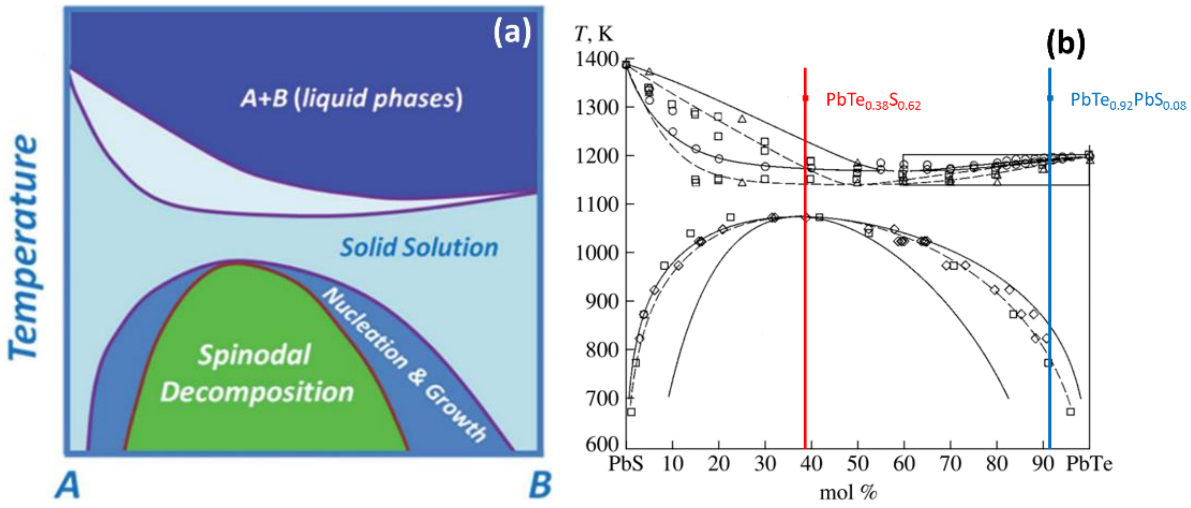

Figure 2.10: (a) A ternary diagram of an A-B system, showing temperature-dependent solubility of B in the A matrix [3], and (b) an adapted PbTe-PbS phase diagram highlighting compositions that will undergo spinodal decomposition (red) and nucleation and growth (blue) mechanisms of phase formation. (Modified from Ref. [6])

Conventional synthesis of these compounds involves heating precursor materials above the melting point for homogenisation, followed by rapid quenching [11]. For the $PbTe_{0.92}PbS_{0.08}$ system, quenching of the melt brings the compound into the nucleation and growth region of the phase diagram. Nucleation of precipitates was observed in the 400-500 K temperature range, with smaller coherent particles ranging in size from 2-10 nm, and larger incoherent particles with an average size of 100 nm [9]. Fig. 2.11(a) shows a scanning transmission electron microscopy (STEM) bright field image of both types of precipitates. However for $PbTe_{0.38}S_{0.62}$, upon quenching and annealing of the melt an entirely lamellar microstructure forms, as shown in Fig. 2.11(b). X-ray diffraction confirmed the decomposition as a eutectoid transformation, which involves the parent phase decomposing into two distinct crystallographic phases. In this case, two distinct phases were identified as PbTe and PbS with 41.2 mol% PbTe

in the composite, which is ~3 mol% more PbTe than the theoretical value for the nominal composition [10].

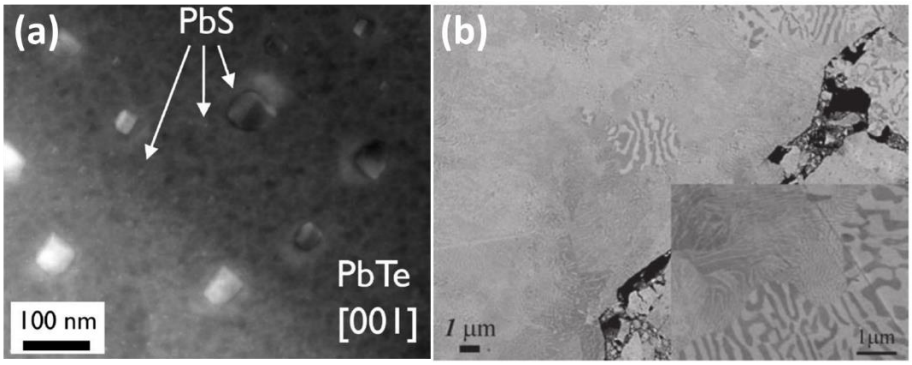

Figure 2.11: (a) Bright field STEM image of $PbTe_{0.92}PbS_{0.08}$ along the [001] direction [9]. (b) Back-scattered electron image of spinodally decomposed phase in $PbTe_{0.38}S_{0.62}$. The bright phase corresponds to PbTe and the dark phase to PbS [10].

In many cases for systems utilising bulk nanostructuring to improve TE performance, little emphasis has been placed on verifying the lifetime of reproducible TE performance. The effect nanostructuring has on the lattice thermal conductivity is based on interfaces between phases, though thermodynamic driving forces act to eliminate interfaces at elevated temperatures in these materials [58]. Further, in ternary and quaternary compounds of PbTe-PbS and PbTe-PbS-PbSe, dopant segregation between the matrix and precipitate phases has been found [14, 15, 50]. The stability of these compounds at the operating temperatures of TE generators needs to be properly assessed to ensure both that nanostructured bulk TEs can sustain adequate TE performance in a practical setting and to better understand the diffusion mechanics of dopants between phases in these materials.

2.5.3 Correlating Fabrication Methods with Performance

The most widely used method to fabricate bulk lead chalcogenide TEs involves homogenisation of precursors above the melting point inside an evacuated sealed quartz ampoule, and quenching the melt after a predetermined time. The steps between quenching of the melt and measurement of TE properties is less uniform within the literature.

Wu *et al.* [46] achieved a reported zT of 2.3 in 3% Na-doped $(PbTe)_{0.8}(PbS)_{0.2}$ by reacting precursors in an evacuated, carbon coated quartz tube at 1323 K for 10 h. This was then quenched, and the resulting ingots were ground into powder followed by densification using spark plasma sintering (SPS) at 40MPa for 10 minutes. SPS is analogous to hot pressing, only the pressed powder is heated by Joule heating from a pulsed DC current (Fig. 2.12). This allows very

fast heating and cooling rates, making the sintering process quite fast. Both SPS and hot press allow for densification of fine powders while retaining nanosized polycrystalline materials (grain size typically ~5-10 nm), allowing lower thermal conductivities to be retained [59]. In this study, Wu *et al* attribute reduced lattice thermal conductivity to the formation of extra Pb-vacancies (which are favourable p-type point defects, allowing further p-type doping) and a higher concentration of grain boundary interfaces when compared to cast ingots [46]. Similar preparation methods have been utilised in bulk nanostructured *p*-type PbSe-MSe (M = Ca, Sr, Ba) [60].

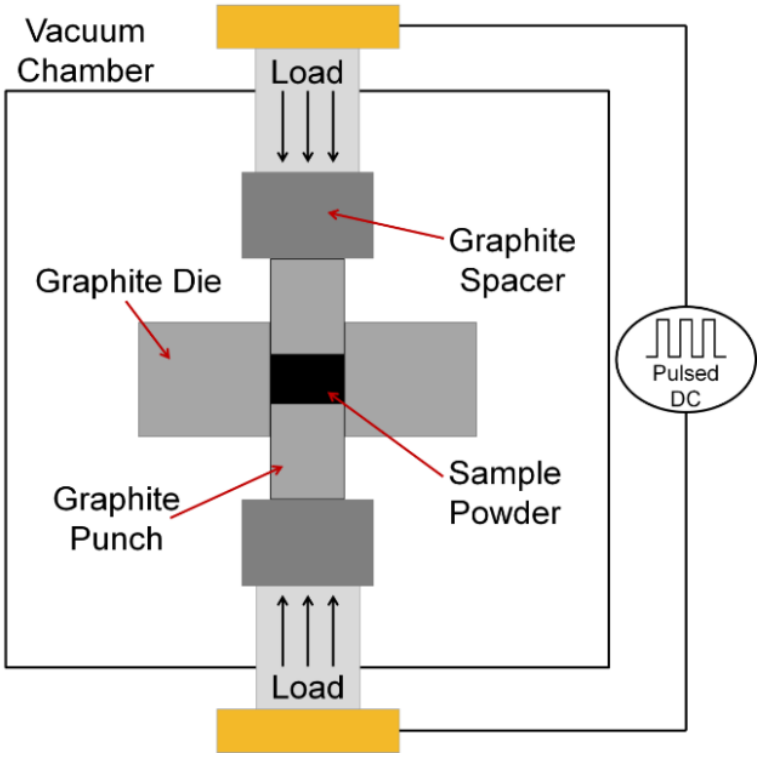

Figure 2.12: Spark plasma sintering (SPS) compresses TE powder between two graphite punches, and is heated by a pulsed DC current under a set pressure.

Another approach is to anneal the quenched sample prior to any form of hot pressing, or to allow the ingot to cool in slowly in the furnace following homogenisation. These approaches have been utilised in $PbCl_2$ doped $(PbS)_{1-x}(PbTe)_x$ [48], $(PbS)_{1-x}Cl_x$ [39], Na-doped $(PbTe)_{0.88}(PbS)_{0.12}$ [27], and $PbCl_2$ doped $(PbSe)_{1-x}(PbS)_x$ [49]. To better understand the implications of each of the methods of preparation on the TE performance of *p*-type $(PbTe)_{0.55}(PbS)_{0.35}(PbSe)_{0.1}$, Aminorroaya *et al*. [11] investigated the TE properties and evolution of microstructures in three samples prepared via quenching the melt (Q), quenching and annealing the melt at 823 K for 72 hours (QA) and slowly cooling the melt in the furnace (FC) prior to SPS.

XRD analysis was conducted prior to sintering, revealing a single phase for the Q sample and two phases in the QA and FC samples. Two phases were identified for the Q sample following sintering. Rietveld refinement showed 26.9 ± 2.5 wt% precipitates in the matrix for all sintered samples. The measured *z*T of Q and QA samples was ~1.5, but ~1 for the FC sample. Hysteresis *z*T response during heating and cooling was observed for all samples, but was most significant in the Q sample. A previous study describes this anomaly as a product of segregation of sodium between the matrix and the PbS precipitates [50]. PbS was found to be sodium rich; upon dissolution of PbS during transport property measurements a release of dopants into the matrix enhances the carrier concentrations, and could modify the band structure or introduce point defects and dislocations. TE property measurements were repeated three times for each sample to assess reproducibility. Repetition of electrical resistivity measurements highlighted irreproducible measurements in the Q sample, with the resistivity decreasing during each subsequent measurement (Fig. 2.13).

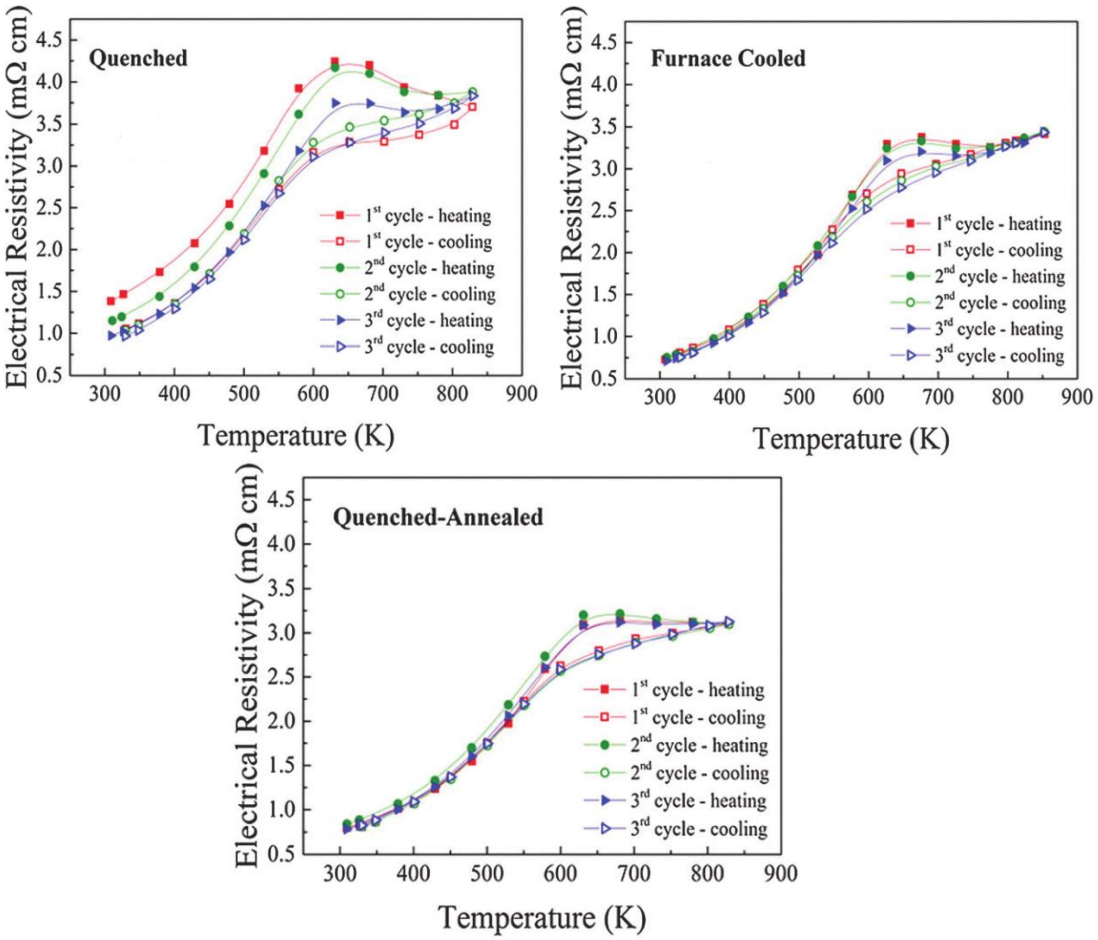

Figure 2.13: Temperature dependent electrical resistivity for the Q, FC and QA samples as a function of repeated measurement cycles [11].

The sample microstructures are shown in Fig. 2.14, and these show that the metastable Q sample contained the finest precipitates, which were subject to coarsening during transport property measurements. The FC sample contained a high concentration of precipitates with an area greater than ~1 um^2, whereas the QA sample predominantly had precipitates less than ~1 um^2 in area. The microscopy analysis for this study was conducted during preliminary work for this PhD project.

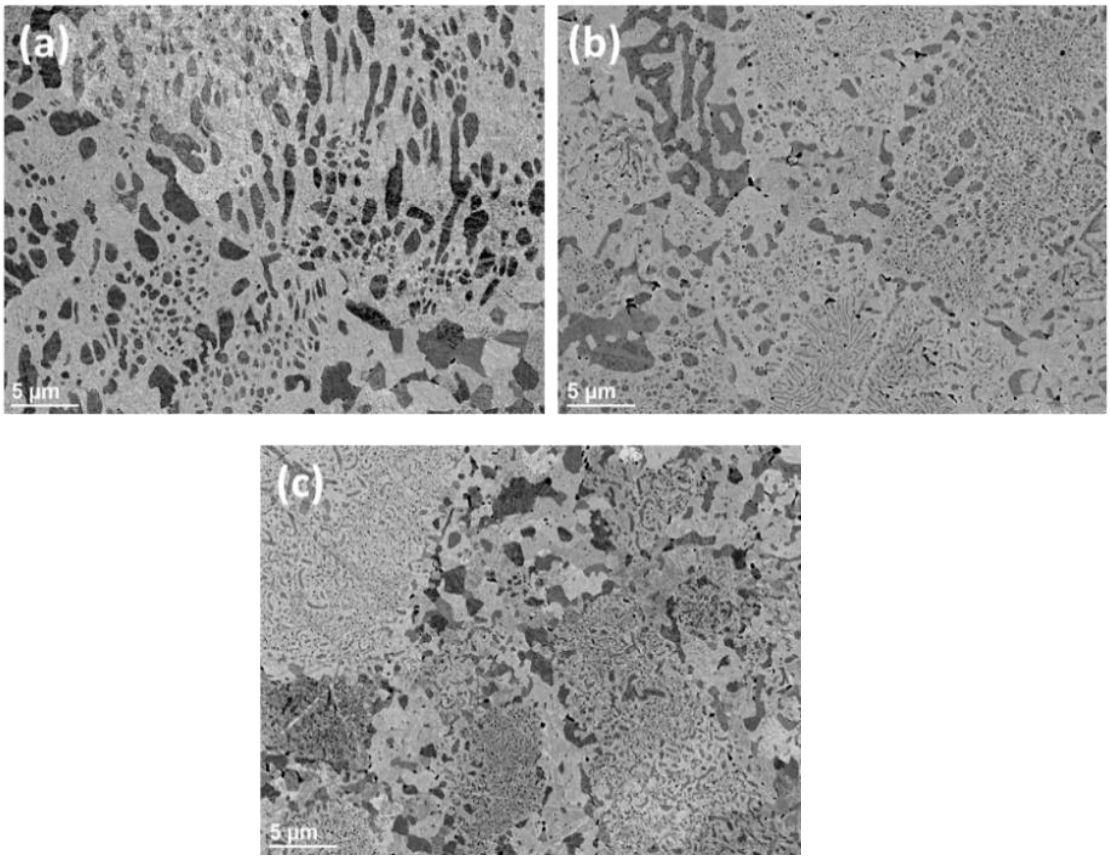

Figure 2.14: Typical SEM micrographs of sintered (a) FC, (b) QA and (c) Q samples [11].

As a result of thermal cycling during transport property measurement, the performance of the Q sample degraded to a value similar to that of the thermally stable samples. QA samples proved to have the most stable and highest overall value for zT (Fig. 2.15), due to a slightly higher carrier concentration achieved compared to the Q and FC samples [11].

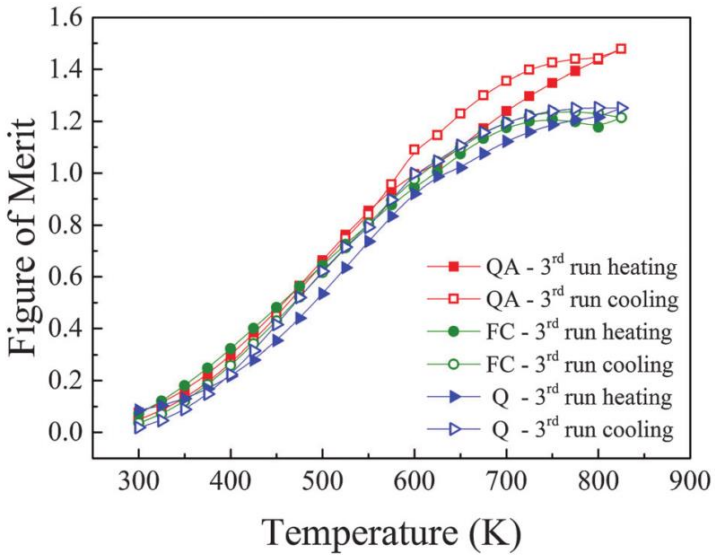

Figure 2.15: The temperature dependent TE figure of merit (zT) for QA, FC and Q sodium doped $(PbTe)_{0.55}(PbS)_{0.35}(PbSe)_{0.1}$ after 3 thermal cycles [11].

2.6 Advanced Microscopy

As it has been described thus far, the TE properties of a TE material correlates very closely with its chemical and electronic properties, which are dictated by alloy composition, dopant type and fabrication method. The microstructure of a TE also has a strong influence on its properties, and thus needs to be well studied to better understand the behaviour of a particular material. By utilising visible light microscopy (LM), scanning electron microscopy (SEM), transmission electron microscopy (TEM) and scanning transmission electron microscopy (STEM), information ranging from particle size and morphology, chemical composition of phases, crystal orientation of phases and grains, dislocation density and much more can be obtained. An example of some of the useful information obtained with STEM is highlighted in Fig. 2.16. The following section will discuss how some of these techniques have been utilised in TE material research.

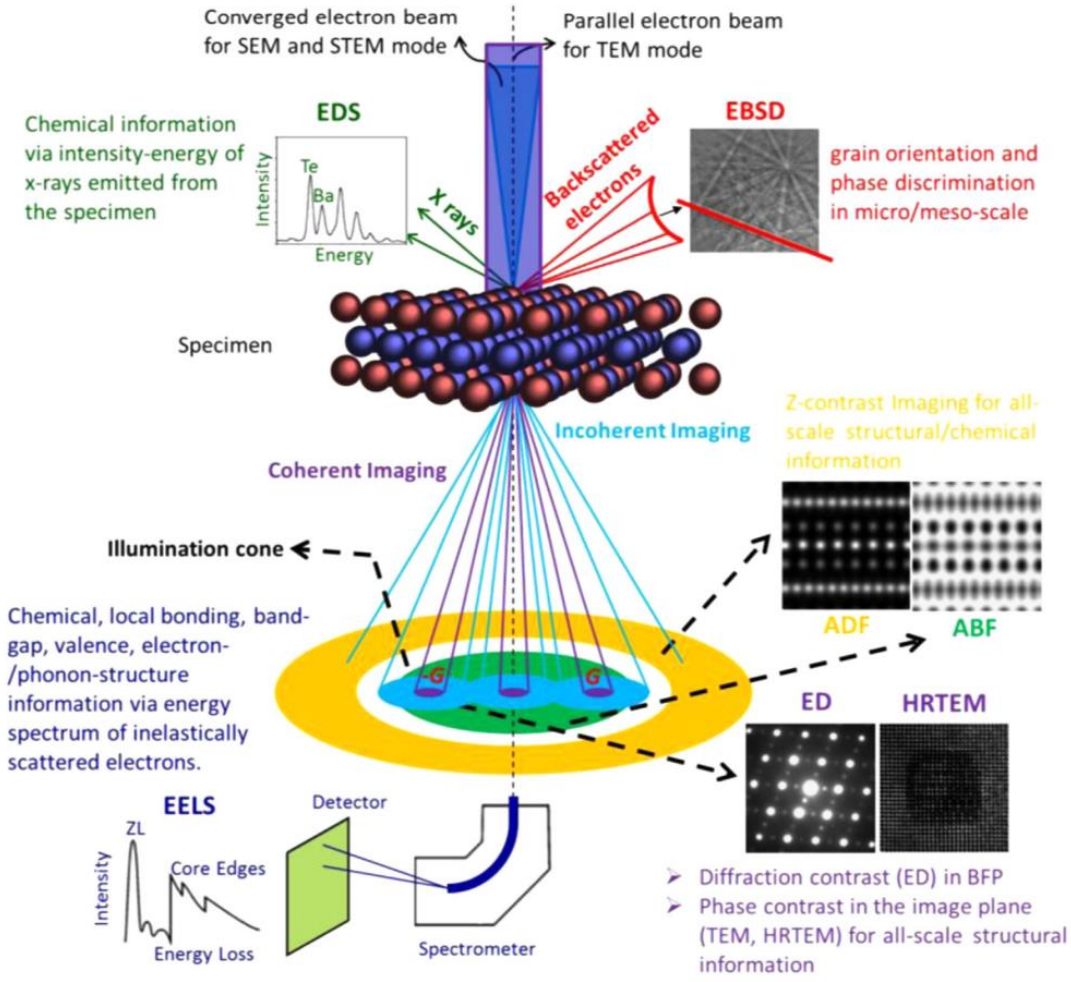

Figure 2.16: The possible information gained from STEM of TE materials. The terms used are abbreviated from energy dispersive X-ray spectroscopy (EDS), electron energy loss spectroscopy (EELS), electron diffraction (ED), electron back-scattered diffraction (EBSD), high resolution transmission electron microscopy (HRTEM), annular bright field (ABF) and annular dark field (ADF) [12].

2.6.1 Electron Back-scattered Diffraction Microscopy (EBSD)

With the boom of bulk nanostructuring in TE research, it is necessary to employ electron microscopy techniques to sufficiently characterise these materials. Ikeda *et al.* [61] utilised SEM-EBSD, a technique that allows distinction of phase and grain orientation and composition, to investigate how cooling rates influenced the microstructures formed in the PbTe-Sb_2Te_3 pseudo binary system. (001) lamellar platelets of Sb_2Te_3 and $Pb_2Sb_6Te_{11}$ oriented parallel to their (001) basal planes and dendritic PbTe were identified, with microstructural feature size changing with cooling rate and composition. Similar studies have been conducted on BiCuSeO to identify anisotropic transport properties due to the formation of layered structures [62].

2.6.2 Selected Area Electron Diffraction

Selected area electron diffraction (SAED) is a tool that is useful for analysing phase boundaries, dislocations and precipitates. Kim *et al.* [13] investigated dislocation arrays embedded in the grain boundaries of $Bi_{0.5}Sb_{1.5}Te_3$ prepared through a liquid-phase compacting process. When comparing stoichiometric melt spun samples (S-MS) to melt spun samples with excess Te (Te-MS), highly crystalline grains were observed with periodic dislocation arrays at grain boundaries in Te-MS. These dislocation arrays were found to have a high efficiency of phonon scattering while doing little to scatter charge carriers; an ideal situation in TE materials. SAED is also effective at identifying orientation relationships between phase and grain boundaries. In some cases, diffractograms of areas in HRTEM images (obtained by carrying out fast Fourier transforms on the relevant area) can resolve similar orientation relationships between phases or grains [63]. The grain boundaries in this study were identified as low energy grain boundaries (effective at scattering midfrequency phonons) due to the observed *d*-spacing mismatch of ~0.15 Å (4.5%) between adjacent grains. Fig. 2.17(D) and (I) shows high resolution TEM (HRTEM) images of a twist-type grain boundary and a tilt-type grain boundary respectively. The diffractograms of grains either side of the boundary (shown in the corners of each image) confirms the plane orientation of each grain and hence allows characterisation of the grain boundary type, lattice spacing and *d*-spacing mismatch between the grains. This technique has been utilised as a characterisation tool in a number of TE studies [7, 9, 15, 50, 64]. In each of these cases, SAED has proven to be an essential tool in identifying the mechanism by which enhanced TE performance has been achieved.

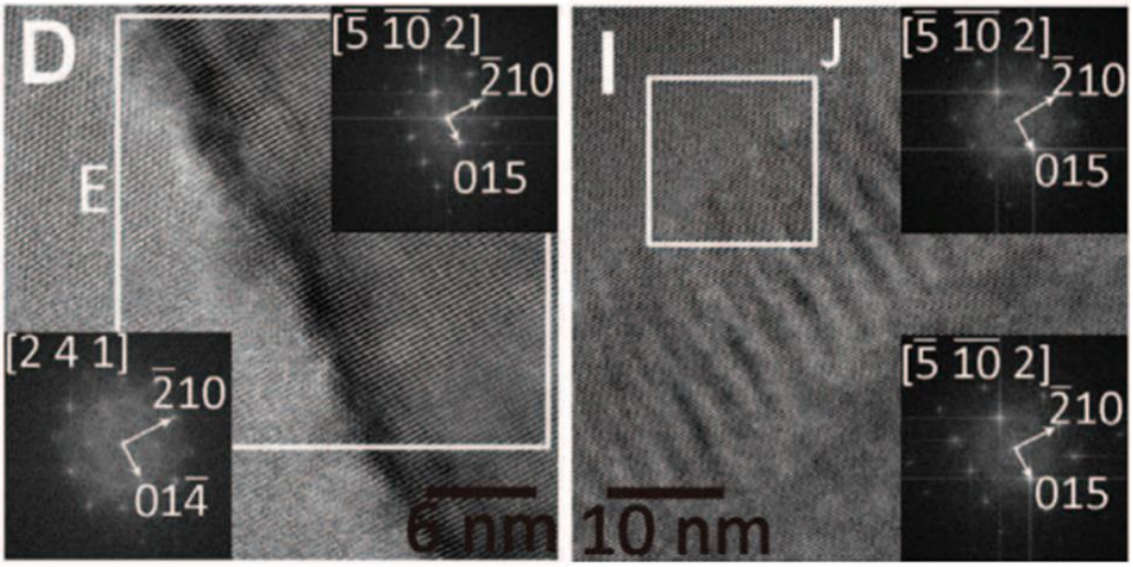

Figure 2.17: (D) HRTEM of a twist-type grain boundary in S-MS, with diffraction information, and (I) HRTEM of a tilt-type grain boundary in S-MS, with diffraction information [13].

2.6.3 Atomic Resolution Microscopy and Analysis

HRTEM observations have proven to be effective for studies interested in particle size, density, distribution and morphology [14, 65-67]. It was recently proposed that controlling the type and concentration of dopant in the PbTe-PbS system allows precise control over precipitate morphology [14]. Low magnification TEM analysis of PbTe-PbS with varying concentrations of PbS can be seen in Fig. 2.18. Hexagonal faceting is observed along the PbTe [110] direction for x = 0.30 and 0.16, while square and rectangular faceting parallel to the [100] axis for x = 0.12 and 0.08, and irregular morphologies for x = 0.04. The number density of precipitates was also seen to decrease with PbS concentration. Morphology was also observed to change with respect to Na concentration, suggesting that the Na/PbS ratio determines precipitate morphology.

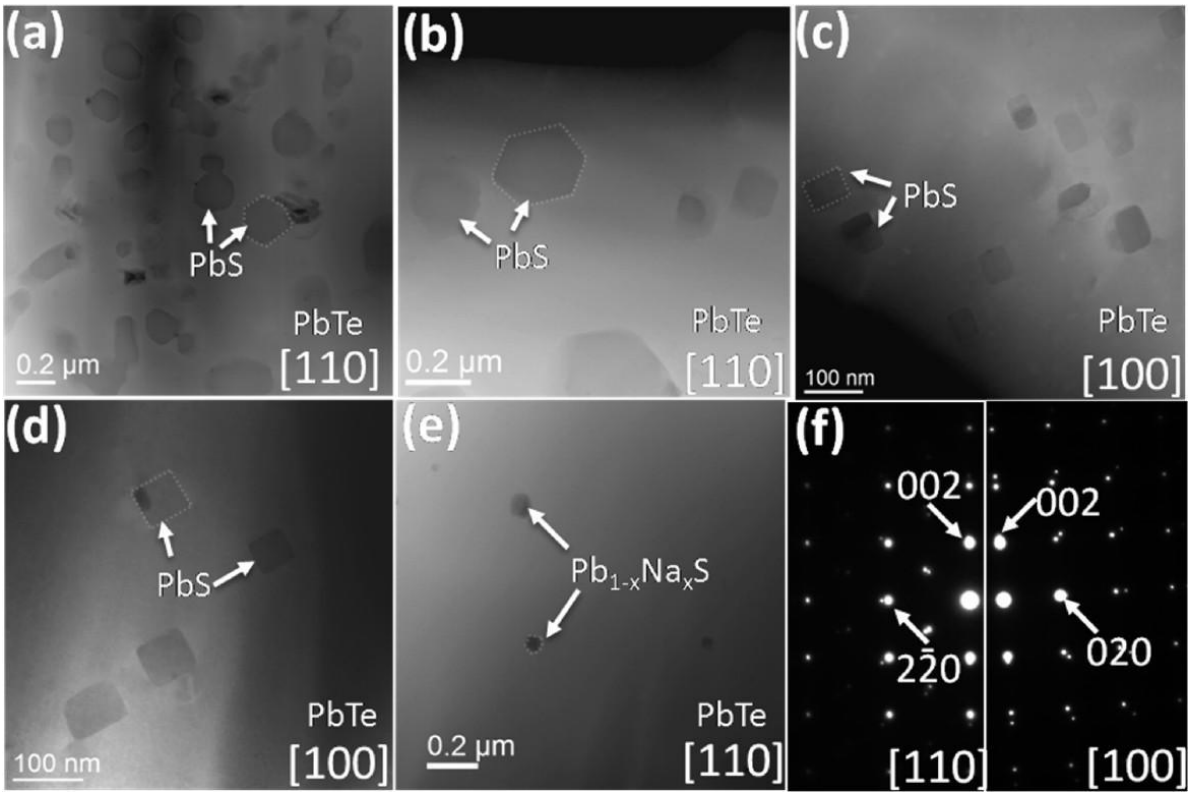

Figure 2.18: Low magnification TEM bright field micrographs of 2 mol% Na $(PbTe)_{1-x}(PbS)_x$, for (a) x = 0.30, (b) x = 0.16, (c) x= 0.12, (d) x = 0.08 and (e) x = 0.04. (f) SAED of the precipitate and matrix [14].

HRTEM and compositional analysis using atom probe tomography were used to resolve the mechanism of precipitate formation. Fig. 2.19a shows a HRTEM image of a PbS precipitate in the 2 mol% Na $(PbTe)_{0.92}(PbS)_{0.08}$ compound. Misfit dislocation contrast is observed at the PbTe/PbS interface. The regularly distributed misfit dislocations were confirmed with

geometric phase analysis (GPA) [68], as in Fig. 2.19b, with Burgers vector 1/2 along [101] with 4 nm spacing. Figs. 2.19c and 2.19d show STEM high angle annular dark-field (HAADF Z-contrast) of the 2 mol% Na $(PbTe)_{0.88}(PbS)_{0.12}$ compound, highlighting interfacial contrast and the presence of edge dislocations. The role of Na in the control of precipitate morphology was attributed to Na partitioning between the PbS and PbTe phases. This observation has been made in a number of studies through EDS analysis [5, 7], and has even been found to enhance TE performance through a modulation doping mechanism [15]. Here, the author has found through atom-probe tomography (a technique allowing atomic resolution chemical analysis of phases) that Na segregates preferentially to the PbTe side of the PbTe/PbS (100) coherent interface, and that the energy of this interface is reduced by the addition of Na at the PbS side of the interface [14]. Semi-quantitative elastic modelling was used to compare the elastic energies of cuboidal and spherical precipitates in the matrix, which suggested that cuboidal precipitates are more energetically favourable across larger precipitates.

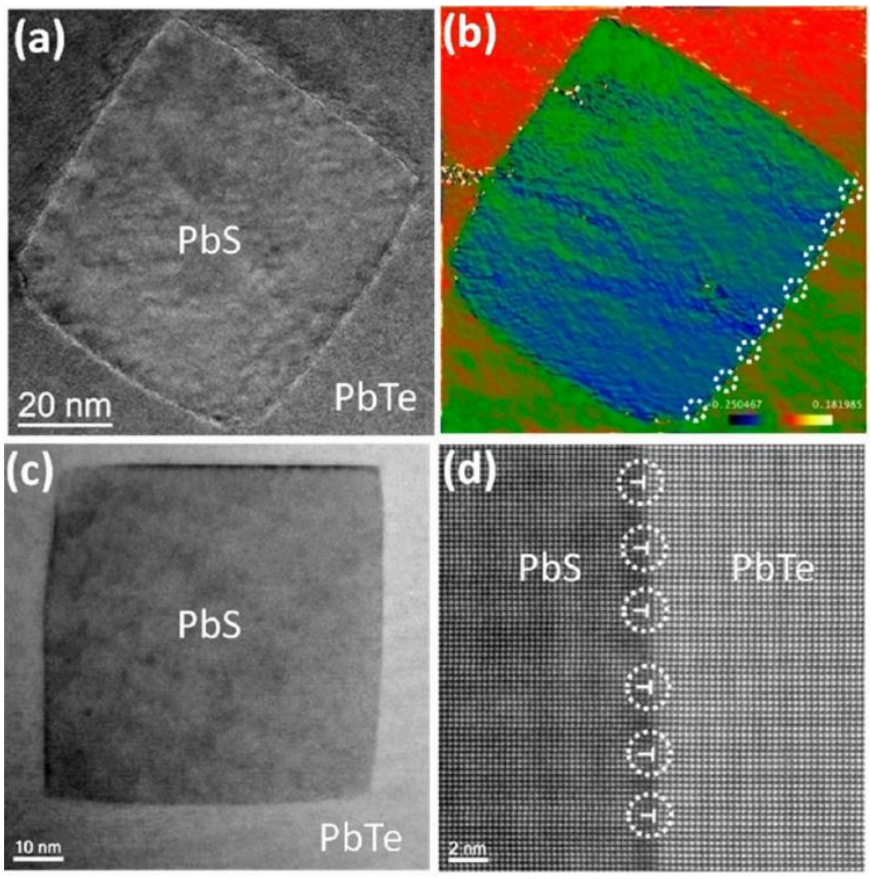

Figure 2.19: (a) HRTEM of a PbS precipitate in 2 mol% Na $(PbTe)_{0.92}(PbS)_{0.08}$, (b) GPA analysis of a PbS precipitate with misfit dislocation cores highlighted with circles, (c) STEM HAADF image of 2 mol% Na $(PbTe)_{0.88}(PbS)_{0.12}$, and (d) Detail of the PbS-PbTe interface, with dislocation cores highlighted [14].

In these described cases, atomic resolution imaging and elemental analysis of precipitates has provided insight into the formation mechanisms of precipitates and the distribution of elements between phases – both of which are essential when considering the development of novel TE systems. It is equally important to assess the viability of such findings for commercial TE devices, if that is the goal. In the study described above, few details are given on the thermal history of the samples. It is explained that samples are homogenised above the melting temperature of the precursors, yet failed to disclose if the melt was quenched, annealed or even sintered post-fabrication. As we now understand [11], these details have a significant influence on the thermal stability of the compound, and may influence how Na dopant partitions between the phases. It is thus important to consider not only how these precipitates form, but how they evolve in situations analogous to TE generation applications. Further, no correlation of precipitate morphology is made with measured transport properties of the system. While these findings appear to be significant for understanding the formation mechanism of PbS in the described system, it sheds little light on the true relevance of precipitate control on TE performance.

2.6.4 Imaging dynamic microstructures

The importance of understanding how TE materials evolve during thermal treatment has been highlighted above. Using in-situ STEM, live imaging of microstructures evolving in response to stimuli (such as thermal, electric and magnetic) can further our understanding of how these materials respond to such stimuli [12]. Aminorroaya *et al.* [15] investigated the heterogeneous distribution of sodium dopant in quaternary PbTe-PbSe-PbS using standard characterisation techniques, such as HRTEM and EDS, as well as in situ heating experiments using STEM. Precipitates in $(PbTe)_{0.65}(PbS)_{0.25}(PbSe)_{0.1}$ were identified as sulphur-rich, with precipitate sizes ranging from 50-300 nm in diameter. Fig. 2.20a shows EDS derived elemental maps of a PbS precipitate in the PbTe matrix. A cube/cube orientation relationship between the precipitate and matrix phases exists, and a lattice mismatch of 7% between the phases was confirmed with SAED, as in Fig. 2.20c. This describes a semi-coherent interface between the PbS and PbTe phases with dislocations accommodating the strain, shown in Fig. 2.20d.

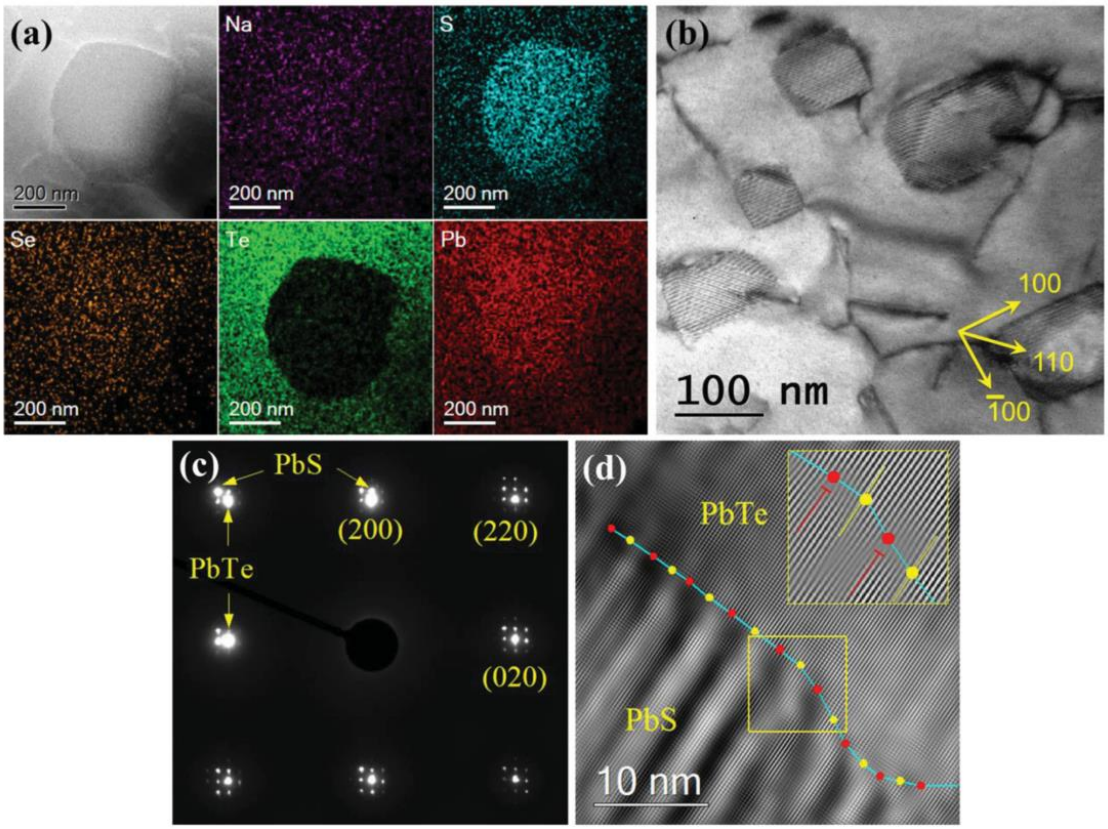

Figure 2.20: (a) HAADF STEM image of a PbS-rich precipitate in a PbTe-rich matrix, identified with EDS for Pb, S, Se, Te and Na. (b) Bright field TEM image of cuboidal PbS precipitates in a PbTe matrix. (c) SAED of PbS precipitate in a PbTe matrix, with beam parallel to [001]. (d) HRTEM of the cube/cube oriented PbS/PbTe interface [15].

Transport property measurements saw a reduction in electrical resistivity and Seebeck coefficient above 600 K for samples doped with 2.5 at% and 3.0 at% Na, achieving zT's of ~1.6 and 2.0 respectively at 850 K. This was a significant improvement over 1 at% Na doped samples, which reached a zT of ~0.9 at 850 K. Heavily doped samples were found to have a step-function increase in Hall carrier mobility at 600 K (which was not present in lightly doped compounds). STEM-EDS analysis was used to resolve this anomaly. EDS analysis of 3.0 at% Na doped $(PbTe)_{0.65}(PbS)_{0.25}(PbSe)_{0.1}$ indicates a comparatively larger concentration of sodium in the PbS precipitate. Alloying of PbSe increases the solubility of sodium in the matrix [69]. As such, sodium was completely dissolved in the alloy with preferential partitioning to the precipitates in heavily doped samples, where the sodium concentration exceeds the solubility limit of the matrix.

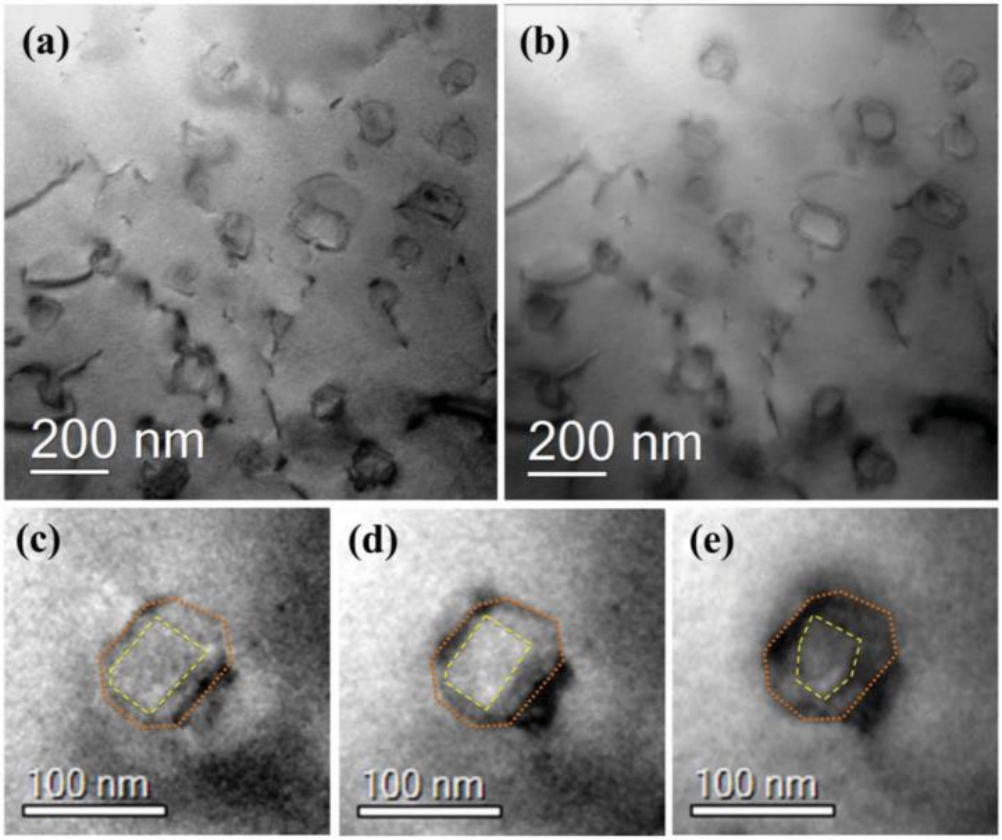

Figure 2.21: In situ heating TEM experiment: (a) PbS-rich precipitates in a PbTe-rich matrix and line dislocation at room temperature, (b) same as (a) at 873 K, (c-e) The same precipitate at room temperature, 623 and 873 K respectively [15].

The influence of temperature on precipitate behaviour was analysed with in situ heating experiments, at 50 K increments up to 573 K, and 25 K increments up to 873 K. Fig. 2.21a and b show the same region of the sample at room temperature and 873 K respectively. No obvious movement of dislocation or dissolution of PbS was observed up to 873 K. However, reshaping of PbS particle interfaces was observed, as shown for a 100nm particle at room temperature, 623 K and 873 K in Fig. 2.21c, 2.21d and 2.21e respectively. Widening of oblique facets above 623 K suggests restructuring of the PbS/PbTe interface to reduce interfacial energy [15]. It is proposed that the step-function behaviour in Hall carrier mobility is due to a redistribution of sodium atoms between the precipitate and matrix phases. The diffusion coefficient of sodium in PbTe and PbS increases exponentially with temperature, meaning diffusion across the interface is possible. The Hall carrier concentration is decreased above 600 K, suggesting that sodium segregates to PbS precipitates and that the matrix dominates the transport properties of the alloy [15]. Investigating dynamic microstructural evolution through STEM has provide insight into the diffusion mechanics of dopants within a multiphase TE system through correlation with measured transport properties.

Chapter 3

Experimental Methods

3.1 Materials Fabrication

3.1.1 Lead Chalcogenides

Polycrystalline samples of *p*-type $Pb_{0.97}Na_{0.03}Te_{0.65}S_{0.25}Se_{0.1}$ were prepared through homogenisation of precursor materials. Polycrystalline samples of PbS were prepared by mixing high purity Pb (99.999%) and dried S (99.9%) in vacuum sealed quartz ampoules at a residual pressure of $\sim 10^{-4}$ Torr. These components were reacted at high temperature to produce the high purity PbS precursor material. The final polycrystalline $Pb_{0.97}Na_{0.03}Te_{0.65}S_{0.25}Se_{0.1}$ samples were synthesised by mixing stoichiometric quantities of Pb, Te, PbS and Se, with Na as the dopant. A final mass of 10 g was sealed in a carbon-coated quartz tube under vacuum, and heated to 1373 K with a heating rate of 100 K per hour. Samples were held at 1373 K for 10 hours, immediately quenched in cold water and annealed at 823 K for 72 hours. The ingots produced from the synthesis procedure were hand-ground to powder with agate mortar and pestle.

SPS was used to sinter powdered samples into 12 mm disk shaped pellets at 773 K and an axial pressure of 40 MPa for half an hour under vacuum. Following sintering, samples thermally aged at 823 K for different time periods to allow comparison thermal history on electronic and structural properties. An as sintered sample was also prepared which was subject to no further thermal ageing. The remaining samples were aged for 1 week, 2 weeks, 4 weeks and 8 weeks.

3.2 Materials Characterisation

3.2.1 X-Ray Diffraction

XRD analysis was performed on lead chalcogenide samples to confirm a consistent lattice parameter and variation of phase ratio was achieved between each of the lead chalcogenide samples. Analysis was conducted using a MACScience X-Ray diffractometer with Cu Kα radiation (λ = 1.544 Å, 40 kV, 25 mA). XRD samples were prepared by grinding ingots or sintered samples into a fine powder using an agate mortar and pestle. A thin, uniform layer of this powder was deposited onto a quartz substrate. The quartz substrate was mounted into the X-Ray diffractometer, and scanned over $20° < 2\theta < 80°$ at a rate of 1°/min.

XRD analysis probes the crystal structure of samples by measuring the angles at which incident radiation is diffracted by a powdered sample. Monochromatic X-Ray radiation is produced via cathode ray tube and focussed at the sample surface during the scan. Diffraction of radiation through the crystalline sample corresponds to its lattice spacing, as described by Bragg's Law [70]:

$$n\lambda = 2d\ sin\theta \tag{3.1}$$

where n is an integer value corresponding to the order of the diffraction peak, λ is the wavelength of incident radiation, d is the atomic displacement in the crystal lattice and θ is the angle of incidence. When Bragg's Law is met, constructive interference occurs and a peak in the X-Ray diffraction pattern is observed. Observing peaks in the diffraction pattern across the 2θ range allows the *d*-spacing to be determined, which is a materials property characteristic of each unique crystal structure. As such, the chemical identity of the sample can be determined through Rietveld refinement and matching to reference XRD data [70].

3.2.2 Thermal Conductivity

The thermal conductivity of a sample defines its ability to conduct heat. The thermal conductivity of lead chalcogenide samples was calculated from Equation 3.2:

$$\kappa = \rho D_T C_p \tag{3.2}$$

Where κ is the thermal conductivity, ρ is the density of the sample ($g.cm^3$), D_T is the thermal diffusivity ($cm^2.s^{-1}$) and C_P is the specific heat capacity ($J.K^{-1}$). The thermal diffusivity (D_T) of samples was determined using the laser flash method (Linseis LFA 1000). Thermal diffusivity measurements are conducted on sintered disc samples. Samples are mounted onto a sample carrier system that is loaded into a furnace. When the sample reaches a predetermined temperature, an energy burst from a pulsed laser is fired at the sample surface. The temperature difference of the front and rear side of the sample is measured with infrared detectors as a function of time, and measurement software uses this data to determine thermal diffusivity.

The density (ρ) was calculated from the measured weight and dimensions of the sample, using Equation 3.3:

$$\rho = \frac{m}{V} \tag{3.3}$$

Where the mass (m) and volume (V) were determined from the weight, thickness and diameter of sintered samples prior to thermal diffusivity measurement. The specific heat capacity (C_p) was determined from Equation 3.4 [71, 72]:

$$C_p\ (k_B\ per\ atom)\ =\ 3.07 + 4.7\ \times\ 10 - 4 \times (T/K\ -\ 300) \qquad 3.4$$

C_p (k_B per atom) = 3.07 + 4.7 × 10^{-4} × ((T/K) – 300), which is understood to be accurate for lead chalcogenides [43, 73].

For crystalline materials, the total thermal conductivity is mainly a product of two mechanisms. These are the lattice thermal conductivity (κ_L) and the electronic contribution to thermal conductivity from charge carriers (κ_E). Therefore, the total thermal conductivity is given by [74]:

$$\kappa = \kappa_E + \kappa_L \qquad 3.5$$

The Wiedemann-Franz law directly relates the electronic conductivity to the electronic contribution to thermal conductivity [74]:

$$\kappa_E = L\sigma T \qquad 3.6$$

Where L is the Lorenz number. The Lorenz number was determined from the approximation [16]:

$$L = 1.5 + exp\left[\frac{|S|}{116}\right] \qquad 3.7$$

Experimental measurements of the electrical conductivity and Seebeck coefficient were then used with equation 3.6 and 3.7 respectively to determine κ_E. From this, rearrangement of equation 3.5 could be used to determine the approximate value of κ_L across a temperature range.

3.2.3 Seebeck Coefficient and Resistivity Measurements

The Seebeck coefficient and resistivity of lead chalcogenide samples was measured using a Linseis LSR-3 instrument. Sintered disk samples are cut into a parallelepiped and polished with #1200 mesh polishing paper. Fig. 3.1 shows the measurement configuration, which is contained within the LSR furnace. Here, the sample is placed between the upper and lower electrode block. The furnace is heated to a specified temperature, at which the lower electrode block applies a temperature gradient across the sample. Two thermocouples are then placed in contact with the sample to measure the temperature gradient. Wires placed at the thermocouple positions measure the change in voltage across the sample, allowing the

resistivity and Seebeck coefficient to be determined. All lead chalcogenide samples were measured from room temperature to 850 K under 0.1 atm of helium, using the slope method.

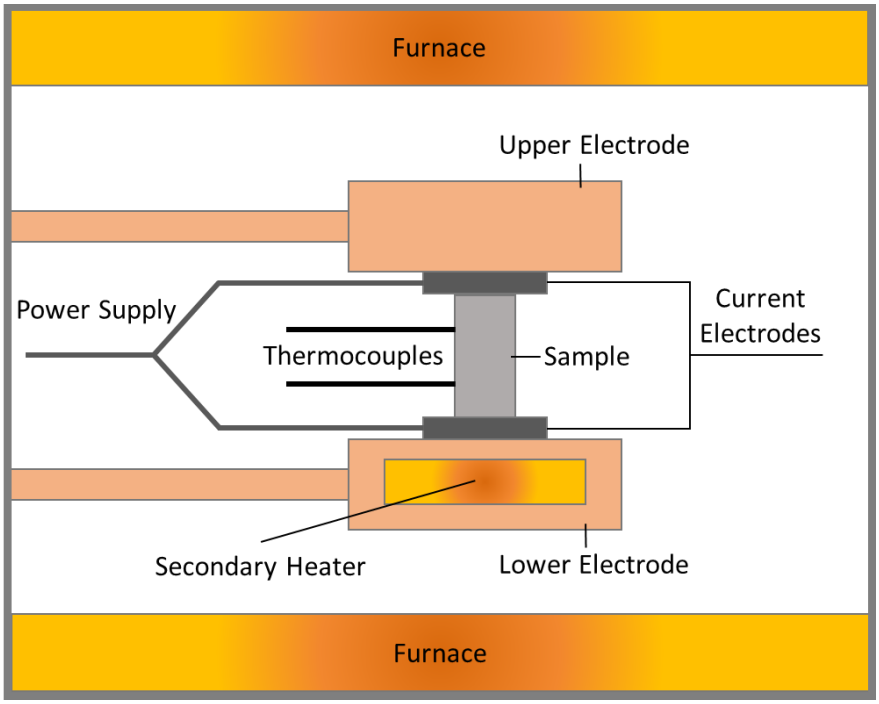

Figure 3.1: Visualisation of the apparatus used for measurement of the Seebeck coefficient.

3.2.4 Optical and Scanning Electron Microscopy Analysis

Light (Leica DM6000) and scanning electron microscopy (JEOL JSM-7001F) analysis requires samples to be finely polished. Cross section segments of sintered and annealed samples of lead chalcogenides and bismuth telluride were mounted in PolyFast resin with a Struers Citopress-20. Once mounted, samples were polished via a multi-stage procedure with a Struers Tegramin-20 auto-polisher. Samples were first polished with a #1200 mesh paper, followed by 15 µm, 3 µm and 1 µm diamond abrasives. Alcohol based lubricant DP-Lubricant Yellow was used for lead chalcogenide samples, and water based lubricant DP-Lubricant Green was used for bismuth telluride samples. Finally samples were Ar-ion milled with the Leica RES101 ion milling system to achieve a defect free surface. For general imaging and EDS analysis, samples were milled at a 2˚ milling angle, 2 kV gun voltage and 4 mA gun current for ~10 minutes. For EBSD analysis, samples were instead milled for ~60 minutes.

Optical microscopy (Leica DM6000) analysis was primarily used for confirmation of polish quality and to identify areas of interest for SEM analysis. SEM (JEOL JSM-7001F) and energy dispersive X-ray (EDS) analysis was the primary tool used for the investigation of sample morphology, particle size distribution and phase composition. Routine imaging of lead

chalcogenide samples was conducted at an accelerating voltage of 15 kV and a probe current of ~3.1 nA. Backscatter electron imaging was primarily used to enhance phase contrast in lead chalcogenide samples. Electron backscatter diffraction spectroscopy (EBSD) was conducted for bismuth telluride samples at an accelerating voltage of 15 kV and a probe current of ~5.5 nA.

3.2.5 Transmission Electron Microscopy Analysis

Scanning transmission electron microscopy (STEM) analysis of lead chalcogenide samples was conducted with a JEOL JEM-ARM200F aberration corrected microscope. STEM analysis requires samples that are polished and milled to electron transparency. To achieve this, samples were prepared via focussed ion beam (FIB). The FIB samples were prepared using an FEI Helios CX G3 with a protecting layer of Pt/C deposited *via* electron beam at 2kV and 5.5nA and ion beam deposited at 30kV and 40pA. Coarse milling was performed at 30kV and 9.3nA with approximate trench widths of 20um, 15um long and 7.5um deep. Single pass cross-sectioning was performed at 30kV and 2.5nA to thin lamella to ~1um prior to J-cut and in-situ lift out.

After welding, lamella were thinned to electron transparency using progressively lower currents from 2.5nA to 0.23nA with incident tilt angles of ±0.3°. The final polish was performed using a single pass cross-sectioning strategy at 5kV and 15pA (~60 seconds per side) and 2kV at 23pA (~60 seconds per side) at a tilt of ±2.5°. Thinning and polishing was monitored *via* electron beam using simultaneous low and high angle annular dark field transmission imaging at 30kV alternating with monitoring approximate film thickness at 5kV with the in-chamber secondary detector through enhanced secondary electron yield from forward scattering.

Chapter 4

Thermoelectric performance changes of thermally aged bulk nanostructured thermoelectrics – a case study of quaternary lead chalcogenides

The mid-range temperature (600–900 K) TE material PbTe has been the focus of many recent studies [25, 28, 35, 41, 67, 75, 76], due to an exceptional base TE performance ($zT \sim 1.4$) which can be significantly improved with alloying [77, 78]. The TE performance of single phase quaternary Pb chalcogenides has proven to be superior to binary and ternary analogues, where the electronic band structure was tuned by PbS alloying, and phonon scattering on high mass contrast solute atoms reduced the thermal conductivity of the alloy [25]. The introduction of nanoscale secondary phases to the bulk TE material has also been utilised to enhance phonon scattering in PbTe alloys [14, 27, 79, 80]. Nanostructures in PbTe alloys have been shown to reduce lattice thermal conductivity with limited influence on electrical conductivity, resulting in improved TE performance [57, 81]. In many cases, nanostructured TE materials samples are quenched from the melt with no further annealing [14, 45, 46]. This technique often provides the most impressive TE efficiency, but does not explore how reliable these efficiencies are in a practical setting.

Thermal stability over the operating temperature range is of vital importance to the success of TE materials [82]. When applied to TE generators, it is necessary to understand how TE performance varies with respect to time at operational temperatures. This is particularly significant for nanostructured TE alloys, as they are subject to evolving microstructures when thermally cycled, based on the fabrication method utilised [11]. We have recently shown the importance of intermediate annealing of multiphase PbTe-based TEs by demonstrating reversible TE performance for annealed p-type $(PbTe)_{0.55}(PbS)_{0.35}(PbS)_{0.1}$ [11, 83, 84]. Quenched and spark plasma sintered (SPSed) samples without intermediate annealing processes yield larger zT values, though TE properties are not reproducible after the samples have been thermally cycled to 823 K for three cycles [11].

The influence of post-fabrication thermal ageing has been explored for nanostructured *n*-type $Ag_{0.8}Pb_{22.5}SbTe_{20}$ [85] and *p*-type $Pb_{0.975}Na_{0.025}S$ with 3.0 at. % SrS and CaS [86]. In each case, thermal ageing of up to 30 and 15 days, respectively, was shown to not only stabilise the zT at high temperatures, but to slightly improve zT in both cases [85, 86]. In the former study, the redistribution of Ag^{+} and Sb^{3+} ions during annealing is said to produce phonon-scattering

nanoscopic inhomogeneities, which improve the zT [85]. The latter study highlights a zT improvement due to reduced thermal conductivity of thermally aged samples, though does not explore the mechanism of improvement in detail [86]. In this chapter, this investigation is furthered by investigating the long-term thermal stability of *p*-type multiphase quaternary $Pb_{0.97}Na_{0.03}Te_{0.65}S_{0.25}Se_{0.1}$, which previously demonstrated an impressive zT of ~2 over the 700-850 K temperature range. Samples are prepared and subject to thermal ageing at 823 K to simulate typical device operation temperatures (823 K) for lead chalcogenides. The TE and microstructural stability of the as sintered sample is compared to samples aged for periods of 1 day, 1 week, 2 weeks, 4 weeks and 8 weeks.

It is shown that by employing appropriate sample fabrication methods for $Pb_{0.97}Na_{0.03}Te_{0.65}S_{0.25}Se_{0.1}$, an impressive zT of ~1.7-1.9 in the 700-850 K temperature range is achieved at all stages of thermal ageing. A redistribution of Na-dopant between phases above ~630 K is believed to explain an increasing electrical resistivity in aged samples. This is balanced by a reduced total thermal conductivity as thermal ageing time increases, possibly due to an increased concentration of nanoscale precipitates in 8 week aged samples. Intermediate annealing of nanostructured *p*-type lead chalcogenides has been shown to be an effective means of preparing highly thermally stable, high performance TE materials.

4.1 Compositional Analysis

The quaternary PbTe-PbS-PbSe system has a microstructure that is analogous to the ternary PbTe-PbS system. This is due to unlimited solubility of PbTe and PbS in PbSe, with a miscibility gap present only in the PbTe-PbS system [6]. Alloying PbS beyond its solubility limit in $(PbTe)_{0.9}(PbSe)_{0.1}$ (~8 at%) causes formation of PbS-rich precipitates in a PbTe matrix [25]. The quaternary $(PbTe)_{0.65}(PbS)_{0.25}(PbS)_{0.1}$ compound can be described as a solid solution of $(PbTe)_{0.9}(PbSe)_{0.1}$ to which PbS is alloyed beyond its solubility limit, causing precipitation of PbS precipitates. The PbS-rich phase forms in the PbTe-rich matrix phase of $Pb_{0.97}Na_{0.03}Te_{0.65}S_{0.25}Se_{0.1}$ through nucleation and growth.

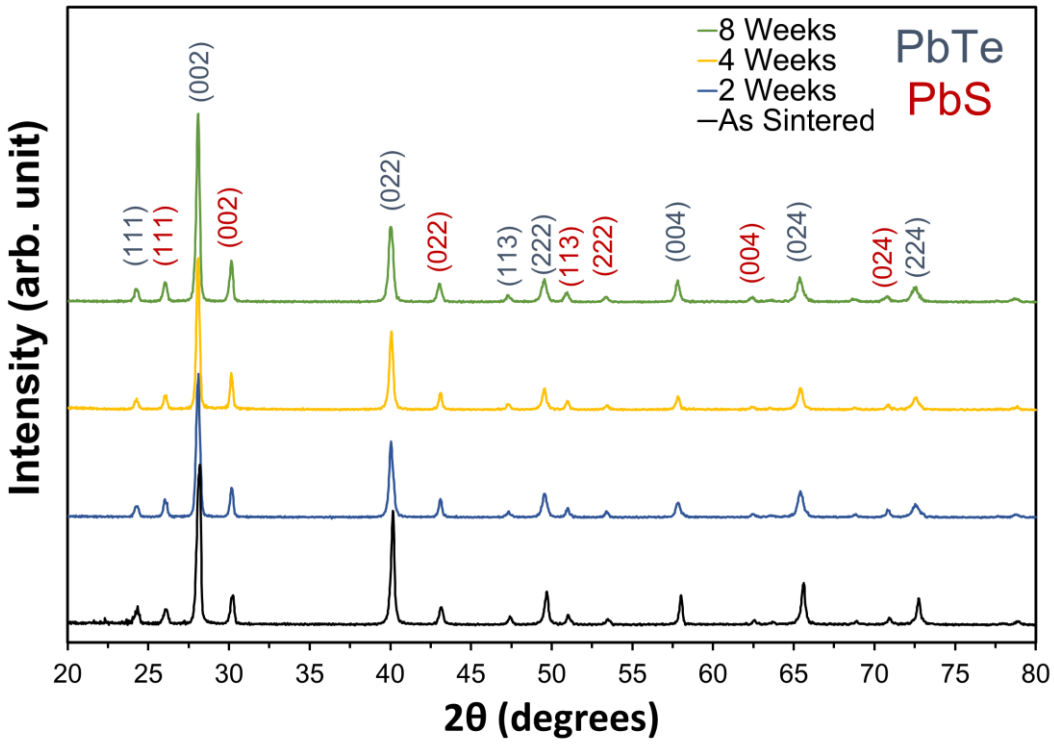

Figure 4.1: Room temperatures X-ray diffraction patterns for $Pb_{0.97}Na_{0.03}Te_{0.65}S_{0.25}Se_{0.1}$ as sintered and thermally aged at 823 K for 2 weeks, 4 weeks and 8 weeks.

Powder X-ray diffraction (XRD) was conducted for samples prior to thermal ageing, confirming the presence of a PbTe-rich phase and a PbS-rich phase. It is also noted that no distinct change in lattice parameter or phase fraction was found following thermal ageing, regardless of ageing time (Fig. 4.1). The chemical composition of each phase in $Pb_{0.97}Na_{0.03}Te_{0.65}S_{0.25}Se_{0.1}$ was confirmed via energy dispersive X-ray spectroscopy (EDS) mapping and point quantitative analysis. Fig. 4.2 shows example TEM-EDS elemental maps of the 4 week aged sample, confirming a PbS rich secondary phase and a PbTe rich matrix. Point quantitative analysis confirmed a higher concentration of Se in precipitates than the matrix, though it can found in both phases. It is difficult to determine the precise concentration of Na via TEM-EDS, due to its low atomic number and beam-induced evaporation. However, previous studies of this alloy have shown partitioning of sodium at phase boundaries, and higher concentrations of sodium in the secondary phase [15, 83]. Precise phase compositions have also been determined previously via atom probe tomography [83]. The matrix and precipitate phases were confirmed to be $PbTe_{0.83}Se_{0.09}S_{0.08}$ and $PbS_{0.8}Se_{0.14}Te_{0.06}$, with sodium concentrations of ~0.6 at% and ~2.9 at% respectively [83]. TEM-EDS analysis of as sintered, 4 week and 8 week annealed samples confirmed that the phase composition remained constant with annealing time.

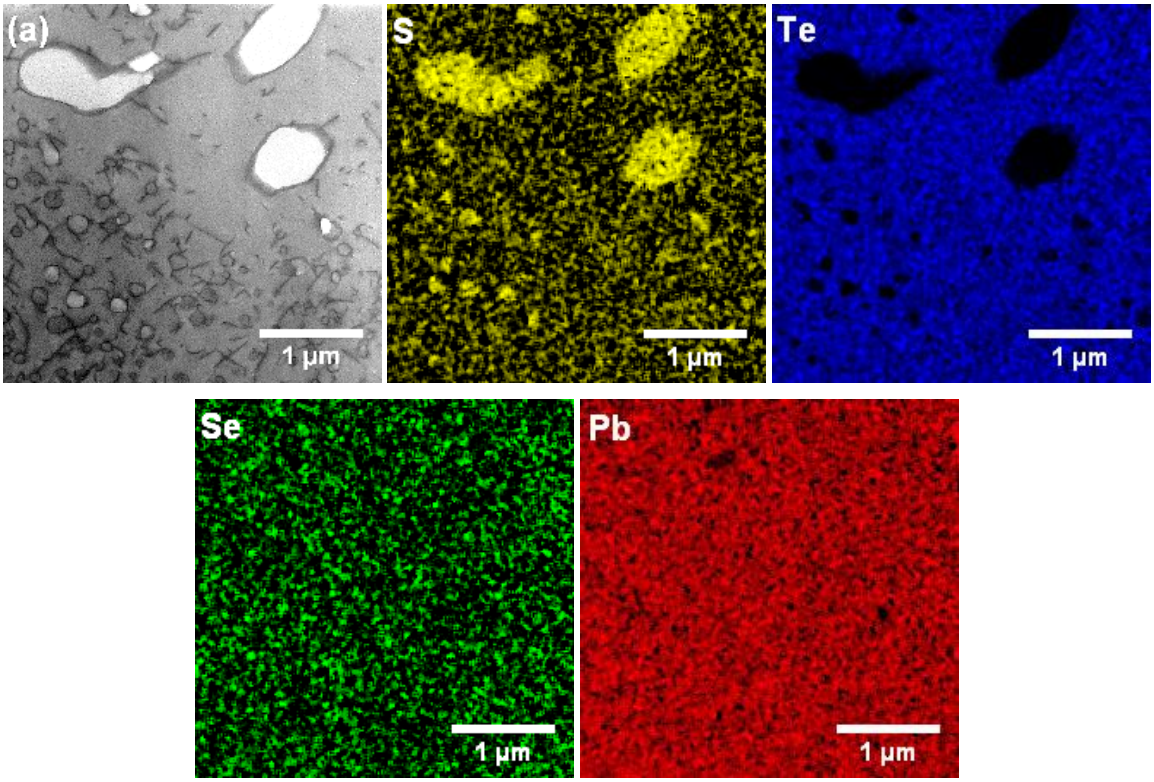

Figure 4.2: EDS characterization: (a) Bright field TEM image of 4 week aged $Pb_{0.97}Na_{0.03}Te_{0.65}S_{0.25}Se_{0.1}$ showing secondary phases within the PbTe-rich matrix, with EDS elemental mapping for Pb, Te, Se and S. The secondary phase is identified as PbS-rich, while selenium is present in both phases.

The Gibbsian interfacial sodium concentrations have previously been compared for equivalent samples of different nominal sodium concentrations, showing a correlation between excess sodium at interfaces and increasing nominal Na concentration [83]. This suggested non-equilibrium segregation of sodium atoms was responsible for excess Na in the secondary phase. It is expected that due to high concentrations of sodium that exceed the solubility limit of the matrix [14, 57], some equilibrium segregation is prevalent at low temperatures. When approaching device operational temperatures (~823 K), the increased mobility of atom-vacancy complexes and dislocations further promotes solute atom segregation [7, 87]. Consequently, rearrangement of sodium at the precipitate/matrix interface has been observed during transport property measurements, which correlate with improved TE efficiencies [15].

4.2 Microstructural Analysis

The evolution and control of secondary phases in bulk TEs has been the focus of many attempts to reduce $\kappa_{lat,}$ and as such improve zT, in recent studies [9, 14, 81, 88]. In nanostructured, multiphase systems κ_{lat} is primarily dictated by the degree of phonon scattering

from atomic scale point defects, nanoscale precipitates and meso-scale grain boundaries [8]. In Pb chalcogenides ~25% of κ_{lat} is from scattering of phonon modes with mean free path (MFP) less than 5 nm (solid solution scattering), 55% from phonon modes with MFP 5 – 100 nm (nanoscale precipitates and interfaces) and ~ 20% from phonon modes with MFP 0.1 – 1 μm (mesoscale grains). For phonon scattering to occur, the dimensions of these features must be similar in magnitude to the phonon MFP length [3]. For solid solution and nanostructured multiphase lead chalcogenides, the influence of nanostructuring on κ_{lat} has been proven to be counterbalanced by a reduction in Hall carrier mobility [7, 15, 89, 90]. The reductions in κ_{lat} were mostly significant at room temperature and are slightly higher than single phase quaternary Pb chalcogenides at operating temperatures [7, 15]. This suggests that the influence of phonon scattering from selenium and sulphur atoms in the matrix is negligible at operating temperatures. To understand how the influence of phonon scattering from nanoprecipitates is affected by thermal ageing time, the coarsening behaviour of $Pb_{0.97}Na_{0.03}Te_{0.65}S_{0.25}Se_{0.1}$ was explored.

The coarsening behaviour of $Pb_{0.97}Na_{0.03}Te_{0.65}S_{0.25}Se_{0.1}$ was investigated by thermally ageing sintered samples at 823 K for periods of 1 week, 2 weeks, 4 weeks and 8 weeks. The influence of post-fabrication annealing was investigated with optical microscopy, SEM and TEM. Fig. 4.3 (a-e) shows typical microstructures of each sample, clearly showing coarsening of secondary phases with aging time. Fig 4.4 shows the precipitate size distribution for each of the corresponding samples. Precipitate statistics were obtained from ImageJ analyses of optical and scanning electron micrographs. Measurements of optical micrographs omitted precipitates less than ~300 nm due to resolution limits of the technique. Scanning and transmission electron micrographs were used for analysis of precipitates smaller than 300 nm. The combined analyses area for each sample was ~ 62 000 μm^2.

The as sintered sample (Fig. 4.3a) has a narrow precipitate size distribution when compared to aged samples, with sizes typically ranging from 0.3 - 1 μm (Fig. 4.4). Within grains spherical PbS precipitates can be observed that are mostly ~350 nm in size. Coarsening of spherical precipitates is most prominent at grain boundaries, with spherical and elongated precipitates typically greater than 1 μm in size. Vacancies are present in the sample, which have likely been introduced during annealing and spark plasma sintering of samples. Following ageing at 823 K for 1 week (Fig. 4.3b) further coarsening at grain boundaries increases the frequency of precipitates greater than ~0.7 μm in size (Fig. 4.4). The fine spherical precipitates present within grains in AS are also less abundant. At this stage of thermal ageing it is clear that a bimodal distribution of precipitates has formed – fine particles reside within grains while distinctly larger precipitates form at grain boundaries.

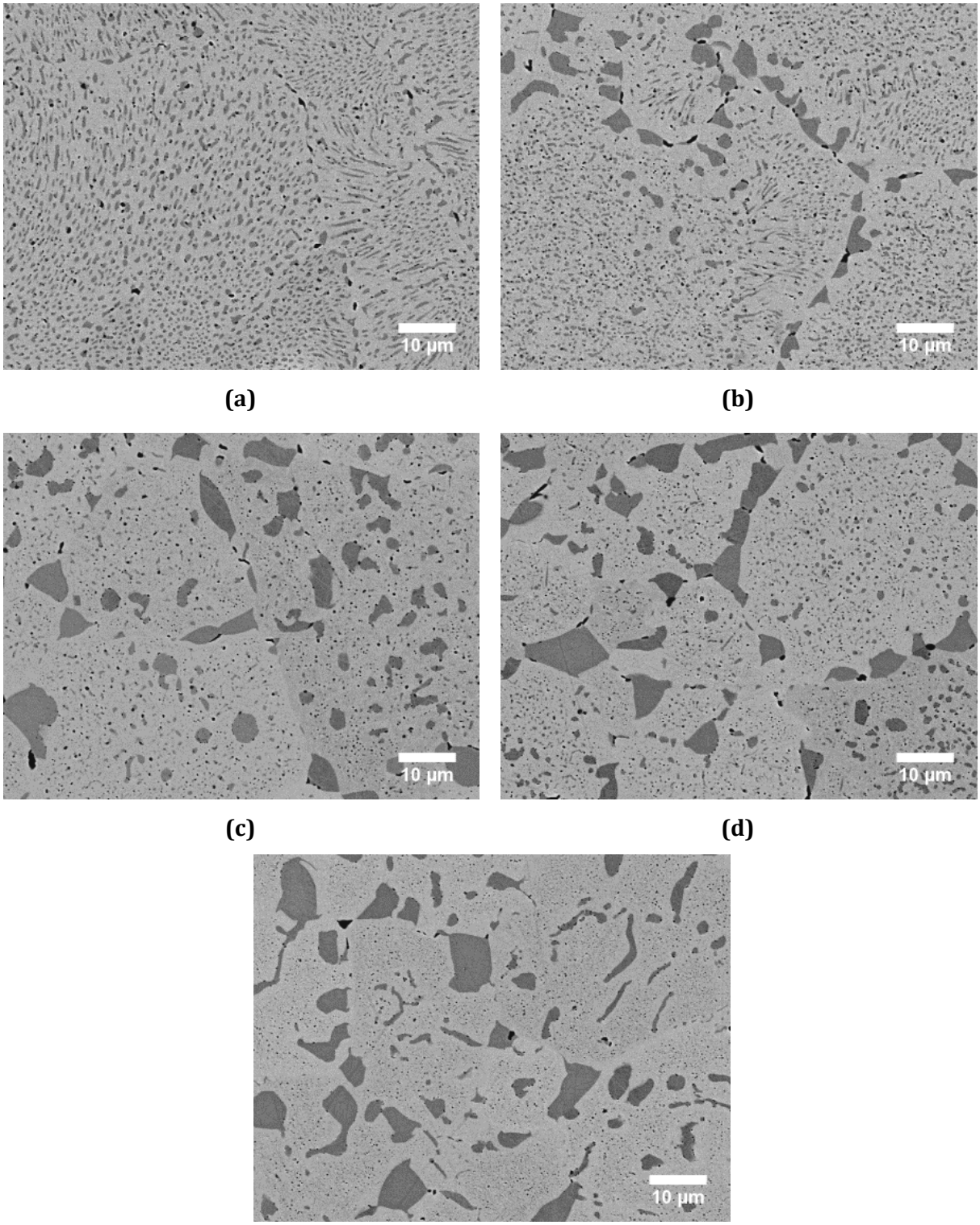

Figure 4.3: Back-scattered electron micrographs of the (a) as sintered sample and samples thermally aged for (b) 1 week, (c) 2 weeks, (d) 4 weeks, and (e) 8 weeks.

After 2 weeks (Fig. 4.3c) the number density of precipitates drops significantly as grain boundary precipitates coalesce while intragrain precipitates shrink via Ostwald ripening. Due to the relative increase of precipitates < 0.3 μm in size, the size distribution of precipitates is dominated by these smaller precipitates (Fig. 4.4). The relative density of precipitates > 2 μm increases after 2 weeks. From 2 weeks to 4 weeks of ageing, the maximum precipitate size remained at ~ 13 μm. Further dissolution and coalescence of 0.3 – 0.7 μm precipitates provided an increase in concentration of 1 – 2 μm sized precipitates. The number of precipitates > 2 μm showed little change from 2 weeks to 4 weeks, though appears smaller in Fig. 4.4 due to the relative increase in 0.7 – 2 μm precipitates. From 4 weeks to 8 weeks ageing the size distribution shows peaks above 2 μm and below ~ 0.4 μm. Ostwald ripening has caused low to mid-range precipitates to drastically decrease in size at the expense of larger, more energetically stable precipitates. Consequently, the size distribution is dominated by the high density of precipitates < 0.4 μm present at this stage of coarsening. A more homogeneous distribution of precipitates > 2 μm are present after 8 weeks ageing, though the max precipitate size remained at ~ 13 μm.

During thermal ageing, the PbS-rich secondary phase coarsens via Ostwald ripening. As such, the internal energy of the system is lowered by redistributing sulphur and sodium from higher surface energy small precipitates to the more energetically stable large precipitates [91]. As shown, the distribution of precipitates is homogenous following sintering, but continues to widen with thermal ageing time. The bimodal distribution of precipitates present with longer thermal ageing time is likely facilitated by grain boundary diffusion of sulphur. Atomic diffusion is well understood to occur more rapidly along grain boundaries than through the crystal lattice below the melting point of crystalline materials, due to reduced activation energy for diffusion at grain boundaries [92-94]. For example, it has been shown that the diffusion coefficient for Pb in Pb increases from 0.28 cm^2/sec for the volume to 0.8 cm^2/sec along grain boundaries [94]. Thus far, diffusion studies on lead chalcogenides have focussed on self-diffusion and inter-diffusion of elements in single crystals. This makes it difficult to assess the significance of grain boundary diffusion of solute atoms compared to that in the matrix, as grain boundary diffusion coefficients cannot be estimated from, for example, self-diffusion coefficients of S in PbS [93] or Na in PbTe [87]. Regardless, it is clear that grain boundary diffusion has a clear impact on the coarsening process in $Pb_{0.97}Na_{0.03}Te_{0.65}S_{0.25}Se_{0.1}$.

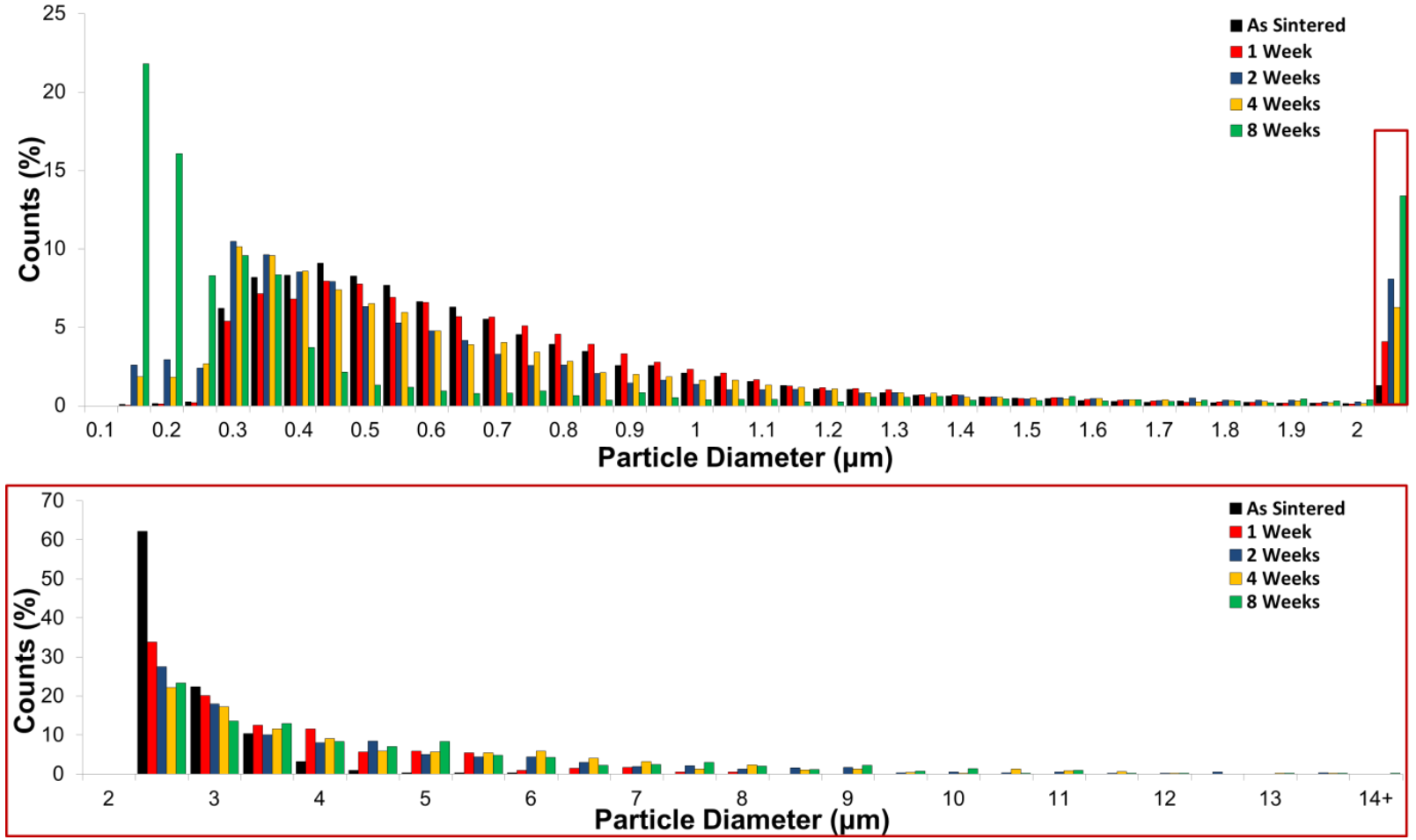

Figure 4.4: Particle size distributions of the as sintered sample and samples annealed for 1 week, 2 weeks, 4 weeks and 8 weeks. The data highlighted in red (above) combines the counts of all particles >2 µm in size. The particle size distribution of these particles >2 µm in diameter is shown below, also highlighted in red. Particle size distributions were obtained through statistical analysis optical and SEM images of sample areas of ~62 000 µm^2.

Through analysis of optical and scanning electron micrographs at each stage of thermal ageing, a coarsening rate for PbS-rich precipitates could be determined. The coarsening rate of the system is dictated by the rate that solute diffuses through the matrix or through short circuit paths from shrinking precipitates to growing precipitates [95]. The Lifshitz-Slyozov-Wagner theory predicts that average precipitate radius, $\bar{r}$, grows with time t according to the equation [95]:

$$\bar{r}^3 - \bar{r}_0^3 = kt$$

where $\bar{r}_0$ is the average precipitate radius at t = 0. The rate constant, k, is given by [95]:

$$k = \frac{2\gamma_i D C_e V_m^2}{\rho_c^2 RT}$$

where $\gamma_i$is the precipitate-matrix interfacial energy, D is the diffusion coefficient of the solute in the matrix, C_e is the concentration of solute in equilibrium with a precipitate of infinite size, V_m is the molar volume of the precipitate, ρ_c is constant related to precipitate size distribution, R is the universal gas constant and T is absolute temperature. Here, k was determined by analysis of the mean precipitate size over the course of annealing.

The mean size of precipitates over the course of annealing is shown in Fig. 4.5. The relationship of average diameter to (annealing time)$^{1/3}$ is linear, as expected. All error bars included were derived from statistical treatments at 95 % confidence. The magnitude of the error in mean diameter for 2 week, 4 week and 8 week samples is a product of the bimodal distribution of precipitates with progressive growth in particle size distribution range with respect to annealing [91]. The slope of the least squares regression fit for Fig. 4.5 returned the coarsening rate constant, k, of 0.0206 μm/h$^{1/3}$. This coarsening rate predicts that after 26 and 52 weeks of thermal ageing, average precipitate diameters of ~1 μm and ~1.1 μm will be achieved, respectively. Precipitates >~100 nm are believed to be much weaker phonon scatterers, and as such are assumed to have little impact on the lattice thermal conductivity of TEs [8, 96]. While the growth of average precipitate size with thermal ageing suggests phonon scattering will be reduced with time, we have shown that coarsening of precipitates at grain boundaries occurs in conjunction with shrinking of intragrain precipitates.

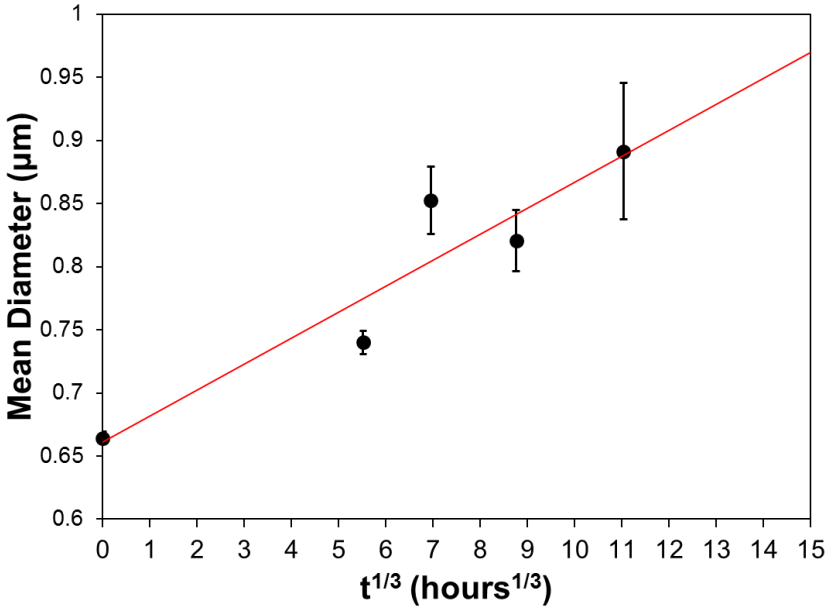

Figure 4.5: Mean particle diameter measurements of as sintered $Pb_{0.97}Na_{0.03}Te_{0.65}S_{0.25}Se_{0.1}$ and analogous samples annealed for 1 week, 2 weeks, 4 weeks and 8 weeks at 550°C. Error bar values were derived from statistical treatments at 95 % confidence.

TEM analysis of the as sintered, 4 week and 8 week aged samples highlighted the changes in morphology of the nanoscale precipitates with respect to annealing time. Fig. 4.6 shows high resolution TEM images from each of the respective samples. Precipitates in the as sintered sample were most commonly irregularly shaped and in the 200-300 nm size range, with very little evidence of precipitates <200 nm in size. Faceted, cuboidal nanoscale precipitates ~50-100 nm in size become prevalent after annealing for 4 weeks (Fig. 4.6b). Further shrinkage of fine precipitates during Ostwald ripening appears to occur, with a greater number density of precipitates in the 20-50 nm size range present after 8 weeks annealing. The previously discussed bimodal distribution of precipitates was confirmed for 4 and 8 week annealed samples with low magnification TEM analysis (Figs. 4.6d and 4.6e). Line dislocations are present in the matrix for each of the samples, and do not appear to pin precipitates. These are likely a product of sample milling for spark plasma sintered discs, the sintering process itself or the Ar-ion milling of TEM samples. It is beyond the scope of this study to conclusively determine the origin of these defects. A coherent interface with a lattice mismatch of 7% has previously been identified at phase boundaries for $Pb_{0.97}Na_{0.03}Te_{0.65}S_{0.25}Se_{0.1}$ [15]. With extended annealing beyond 8 weeks it is expected that a higher concentration of precipitates in the 1-20 nm range will temporarily be present, though this was not explored in this study.

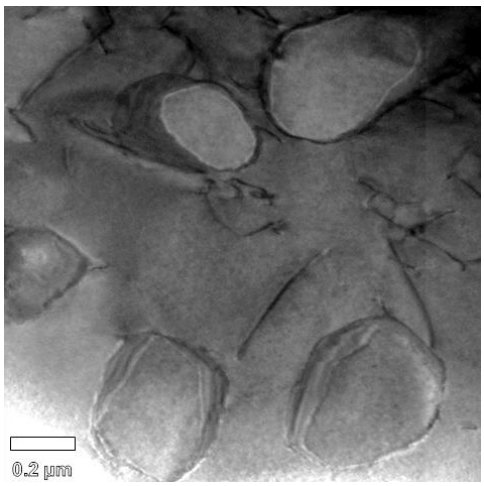

(a)

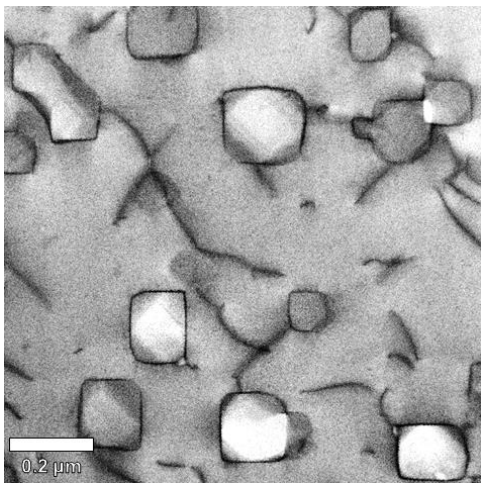

(b)

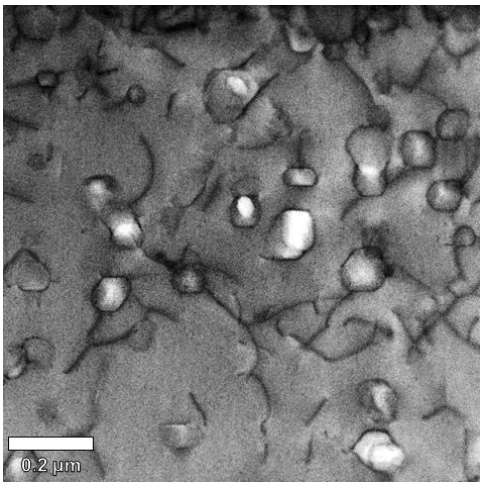

(c)

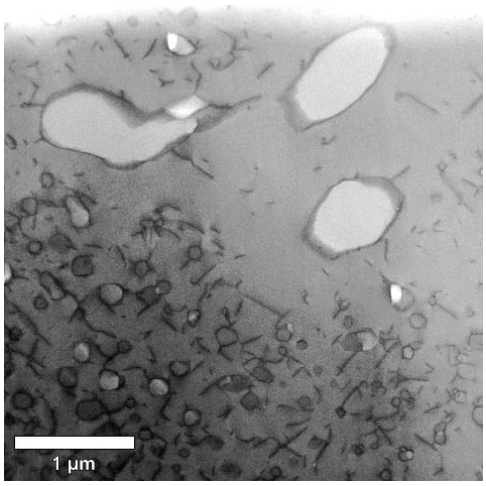

(d)

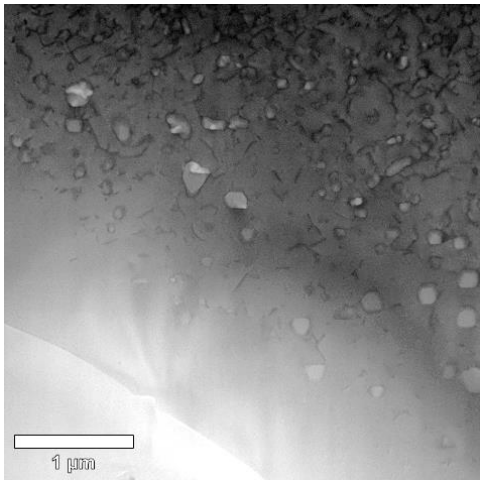

(e)

Figure 4.6: Bright field high-mag TEM images of the (a) as sintered sample and samples thermally aged for (b) 4 weeks and (c) 8 weeks. Bright field low-mag TEM images of samples thermally aged for (d) 4 weeks and (e) 8 weeks. A bimodal distribution of precipitates can be seen in (d and e), with precipitates > 1 µm present alongside nanoprecipitates.

4.3 Thermoelectric Transport Properties

All samples prepared were doped as *p*-type materials with composition $Pb_{0.97}Na_{0.03}Te_{0.65}S_{0.25}Se_{0.1}$. The Seebeck coefficient, resistivity, total thermal conductivity (κ_T), lattice thermal conductivity (κ_L), electronic thermal conductivity (κ_E) and zT over the 300 – 850 K temperature range are shown in Fig. 4.7. Fig. 4.7a shows that Seebeck coefficients increase with temperature, which is typical behaviour of degenerate semiconductors. Above 630 K, the Seebeck coefficient of the AS sample reaches a maximum of ~ 260 μV/K before decreasing to ~ 240 μV/K at 850 K. With annealing in excess of 4 weeks, it appears that the Seebeck coefficient simply reaches a maximum at ~630 K and retains this value up to 850 K. The plateau in Seebeck effect above 630 K is understood to be a product of the two-valence band model in alloys of PbTe [22, 43]. A light valence band and heavy Σ-band are present in these alloys, and the energy of these bands converge as temperature increases. The observed plateau in Seebeck coefficient is due the ability for carriers to access chemical potential states in both the light and heavy valence bands [22, 43].

Comparison of the resistivity (Fig. 4.7b) similarly shows little deviation between samples below ~630 K. Above ~630 K, the as sintered sample reaches a maximum of ~ 3 mΩ cm and then decreases to ~ 2.8 mΩ cm at 850 K. From 1-4 weeks ageing this maximum is maintained from 630 – 850 K. After 8 weeks ageing, the resistivity curve instead increases from ~ 2.8 mΩ cm at 630 K to ~ 3.7 mΩ cm at 850 K. To explain why resistivity above 630 K increases with annealing time, diffusion effects must be considered. It has been previously shown that at high temperatures the Hall carrier mobility of $Pb_{0.97}Na_{0.03}Te_{0.65}S_{0.25}Se_{0.1}$ is larger than that of less heavily doped analogues [15]. Further, the nature of resistivity and Seebeck curves for $Pb_{0.97}Na_{0.03}Te_{0.65}S_{0.25}Se_{0.1}$ suggests that the TE properties are dominated by the matrix phase [15]. As dopant concentration decreases, resistivity curves show a similar trend to those shown in Fig. 4.7b. Heavily doped samples reach a maximum at ~630 K before reaching a minimum at 873 K. With decreasing dopant concentration (or in this case increasing annealing time), resistivity begins to plateau between 630 K and 873 K before eventually continuing to rise above 630 K.

Previous studies have shown that diffusion at the precipitate/matrix interface explains anomalous behaviour of resistivity above 600 K, and can also been observed in the Hall coefficient and carrier mobility [15, 50]. Hot stage TEM highlighted that heating up to 872 K causes redistribution of the interface, which either facilitates or is caused by redistribution of sodium between the phases [15]. Reduced Hall carrier concentrations above 600 K suggests that sodium segregates to the secondary phase during the partial dissolution of precipitates [15, 50].

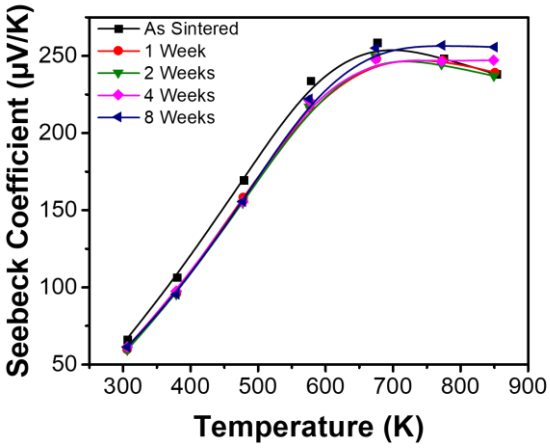

(a)

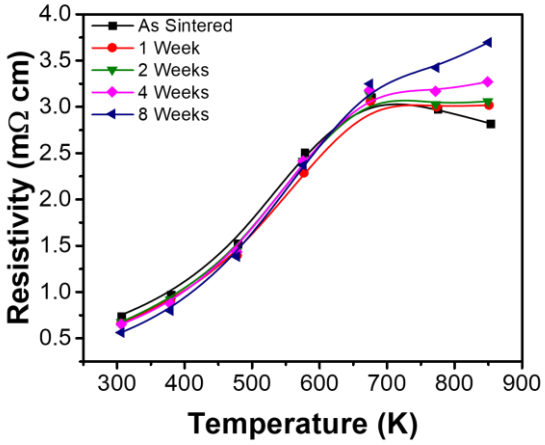

(b)

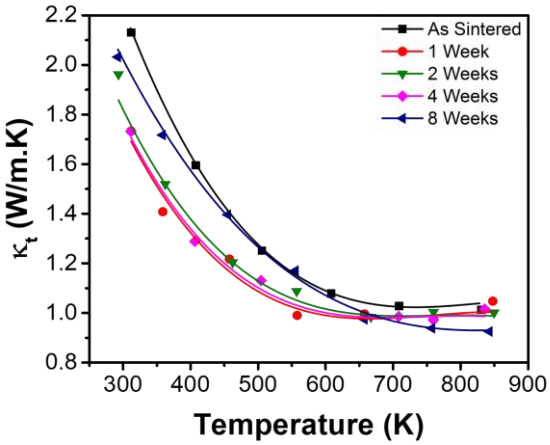

(c)

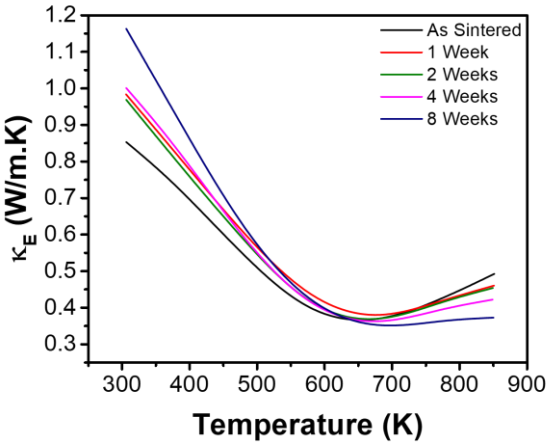

(d)

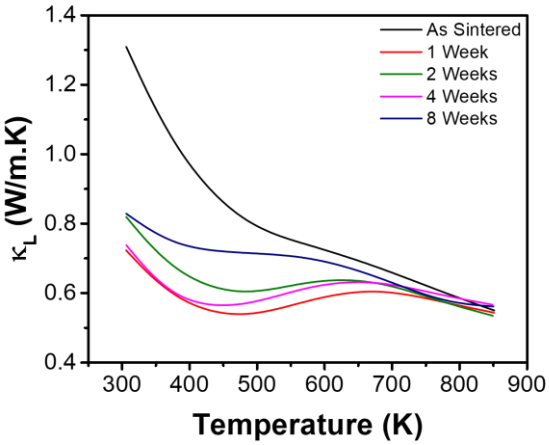

(e)

Figure 4.7: Temperature dependent (a) Seebeck coefficient (μV/K), (b) resistivity (mΩ cm), (c) total thermal conductivity (W/mK), (d) electronic thermal conductivity (W/mK), (e) lattice thermal conductivity (W/mK).

Here, the ageing process acts to stabilise and eventually increase resistivity above 600 K after as little as 1 week of annealing. The influence of the redistribution of dopants appears to decrease with annealing time for a number of possible reasons. Coarsening of the microstructure reduces both the number of secondary phase precipitates present, while reducing the relative surface area of these precipitates. Since smaller, high surface area precipitates have a higher concentration of sulphur and sodium than the surrounding matrix, these precipitates will continue to shrink at the expense of larger, low relative surface area precipitates. Due to the number density of precipitates decreasing with annealing time, it is expected that less sodium segregates to the secondary phase due to less significant dissolution of small secondary phase precipitates. Consequently, at 850 K we observe an increase in the resistivity of samples ranging from ~2.8 mΩ cm for AS to ~3.7 mΩ cm after 8 weeks of annealing. At room temperature the resistivity of samples decreases with ageing time from ~0.74 mΩ cm for the AS sample and to ~0.55 mΩ cm after 8 weeks annealing. This suggests that while annealing has limited impact on the room temperature resistivity of the sample, the influence of increased matrix carrier density is significant at operational temperatures of ~650 K and above.

The total thermal conductivity of samples aged for different lengths of time have been compared in Fig. 4.7c. At room temperature the thermal conductivity of samples appears to follow no distinct trend. The as sintered and 8 week aged have thermal conductivities of ~2.2 $Wm^{-1}K$ and 1.9 $Wm^{-1}K$, respectively. Room temperature thermal conductivities of 1, 2 and 4 week aged samples are ~1.7 $Wm^{-1}K$. At ~850 K total thermal conductivity decreases with respect to ageing time. The as sintered sample has a thermal conductivity of ~1.1 $Wm^{-1}K$, which decreases to ~0.9 $Wm^{-1}K$ after 8 weeks of annealing. The lattice thermal conductivity was determined by subtracting the electronic component from total thermal conductivity. The electronic thermal conductivity (Fig. 4.7d) was determined via the Weidmann-Franz relation, $\kappa_E = LT/\rho$, where ρ is the resistivity and L is the Lorenz number.

The Lorenz number was approximated over the temperature range using two methods. The first is an approximated model related to the absolute Seebeck coefficient, and is described in Ref [16]. The second estimates the Lorenz number, assuming a single parabolic band (SPB) and acoustic phonon scattering over the desired temperature range. The latter method employs the Fermi integral:

$$F_j(\eta) = \int_0^\infty f\varepsilon^j d\varepsilon = \int_0^\infty \frac{\varepsilon^j d\varepsilon}{1+\exp(\varepsilon-\eta)} \quad 4.1$$

where η is the reduced chemical potential, which is determined from the Seebeck coefficient using Eq. 4.2:

$$S = \frac{k}{e}\left(\frac{2F_i(\eta)}{F_0(\eta)} - \eta\right) \quad 4.2$$

Correct fitting of η to Eq. 4.2 allows calculation of L through Eq. 4.3:

$$L = \left(\frac{k}{e}\right)^2 \frac{3F_0(\eta)F_2(\eta) - 4F_1(\eta)^2}{F_0(\eta)^2} \quad 4.3$$

Lorenz number estimations assume chemically homogeneous samples with uniform electronic properties, as it is calculated from band structure estimations of the sample. This is not the case for multiphase systems, and as such some error is included in the calculation. Determination of the Lorenz number and subsequent calculation of κ_E was conducted for the as sintered sample using both the approximation method described by Ref [16], and the SPB model (Fig. 4.8). κ_E varied by < 2% across the 325 – 875 K temperature range, and as such the approximation method was employed for all subsequent κ_E calculations.

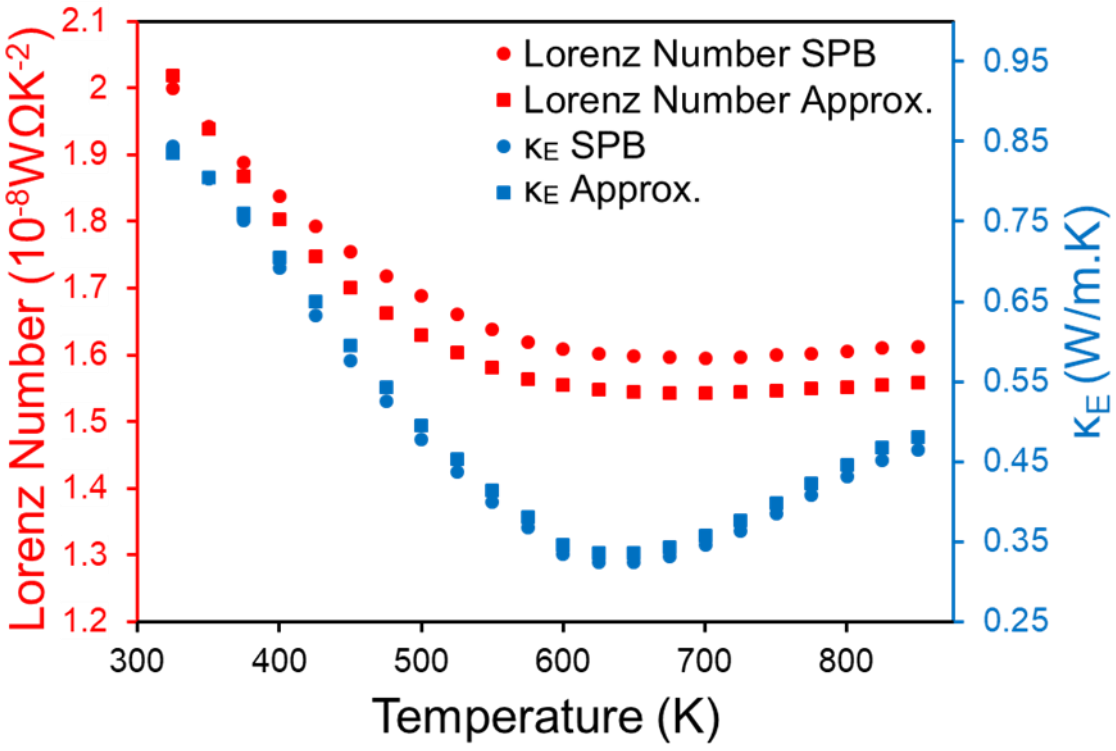

Figure 4.8: Comparison of the Lorenz number for as sintered $Pb_{0.97}Na_{0.03}Te_{0.65}S_{0.25}Se_{0.1}$ across the 325-875 K temperature range, calculated via the single parabolic band model and an approximation based on the Seebeck coefficient (from Ref. [16]). Subsequent calculation of κ_E across the 325-875 K temperature range shows discrepancies of <2% between the two methods used.

Fig. 4.7e compares the lattice thermal conductivity of each sample. As with the total thermal conductivity, no distinct trend is observed relating room temperature lattice thermal conductivity to ageing time. The room temperature lattice thermal conductivity of the as sintered sample is ~1.3 $Wm^{-1}K$, which is considerably higher than that of the aged samples which range from ~0.7-0.8 $Wm^{-1}K$. This significant reduction of lattice thermal conductivity is likely a result of the increased density of nanoscale precipitates introduced as samples are aged [3, 97]. At device operational temperatures of 823 K, the lattice thermal conductivity of all samples converges at ~0.6 $Wm^{-1}K$. As this is not the

observed behaviour in the total thermal conductivity, it suggests that electronic contributions to thermal conductivity dominate above ~630 K. A study of annealed, nanostructured PbTe−4 mol % SrTe doped with 2 mol % Na showed similar convergence of lattice thermal conductivity at high temperatures [98]. It is suggested that the coarsening of Na nanoprecipitates is primarily responsible for reduction in charge carrier concentration and electrical conductivity. Phonon scattering is instead primarily dictated by coarsening of $SrTe_{1-x}O_x$. In this case, nanoprecipitates were primarily in the 1-2 nm size range, with further coarsening reducing the number density of particles available to scatter phonons [98]. In the current study, the Ostwald ripening process instead introduced some phonon scattering precipitates due to the wide size distribution of precipitates present prior to annealing. As such, the room temperature lattice thermal conductivity of as sintered and annealed samples is likely a product of varying number densities of phonon scattering precipitates present at each stage of annealing. This suggests that when considering $Pb_{0.97}Na_{0.03}Te_{0.65}S_{0.25}Se_{0.1}$ for application in a TE module, nanostructuring is likely not the determining factor for performance at operation temperatures.

The TE figure of merit (Fig. 4.9) shows similar behaviour all samples in the 300-850 K temperature range. The as sintered and 8 week aged sample appear to show a most impressive zT of ~1.9 at 850 K. While the 2 week aged sample shows a zT of ~1.7 at 850 K, likely due to a comparatively low Seebeck coefficient across between 300-850 K and the increase of resistivity with annealing. Further annealing from 4 to 8 weeks introduces phonon scattering nanoprecipitates into the system, though this has little effect on the lattice thermal conductivity above 800 K. 4 and 8 weeks of annealing was shown to reduce the resistivity due to a lower concentration of sodium redistributing to the matrix phase above 650 K. However, this affect also reduced the electronic thermal conductivity of samples as ageing time increased. As such, the 4 and 8 week annealed samples boasted high *z*T's of ~1.9 at 850 K due to reduced total thermal conductivity and an improved Seebeck coefficient. The stability in zT of $Pb_{0.97}Na_{0.03}Te_{0.65}S_{0.25}Se_{0.1}$ over 8 weeks of ageing at 823 K confirms that the fabrication method used is suitable for the fabrication of materials applicable in TE generators. Further, this highlights that despite the constantly evolving microstructure of $Pb_{0.97}Na_{0.03}Te_{0.65}S_{0.25}Se_{0.1}$ throughout thermal ageing, the TE performance remained impressive with or without significant contribution from fine nanostructured precipitates. Instead, the driving force of impressive TE performance for $Pb_{0.97}Na_{0.03}Te_{0.65}S_{0.25}Se_{0.1}$ appears to be from the dissolution of the precipitated phase and redistribution of dopant between the phases above ~630 K.

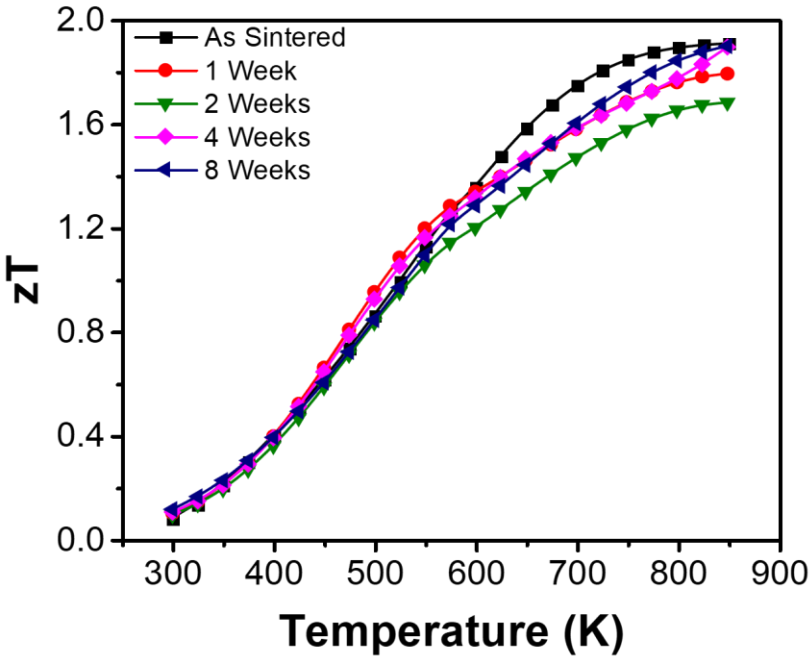

Figure 4.9: Temperature dependent figure of merit (zT) for as sintered and annealed $Pb_{0.97}Na_{0.03}Te_{0.65}S_{0.25}Se_{0.1}$ samples.

Chapter 5

Assessing phase discrimination via the segmentation of an elemental energy dispersive X-ray spectroscopy map: A case study of Bi_2Te_3 and Bi_2Te_2S

Over the last decade, bismuth telluride based alloys have been heavily investigated due to their exceptional performance as a room temperature TE cooler or generator. Recent studies have shown that multiphase TE compounds exhibit higher conversion efficiencies than their single-phase counterparts [13, 15, 99, 100]. In the case of Bi-Te-S (stoichometrically referred to as $Bi_2Te_{2.5}S_{0.5}$), the alloy system comprises two phases; namely, $Bi_2Te_3$and Bi_2Te_2S. Both phases have a trigonal crystal structure (space group 166, $R\bar{3}m$) with the following lattice parameters: $a = b = 4.39$ Å, $c = 30.47$ Å (Bi_2Te_3), $a = b = 4.18$ Å, $c = 29.45$ Å (Bi_2Te_2S) with α = β = 90° and γ = 120°. Bi_2Te_3 consists of five layers in three blocks in the sequence $[Te_2\text{-}Bi\text{-}Te_1\text{-}Bi\text{-}Te_2]_0$ - $[Te_2\text{-}Bi\text{-}Te_1Bi\text{-}Te_2]_{1/3}$ - $[Te_2\text{-}Bi\text{-}Te_1\text{-}Bi\text{-}Te_2]_{2/3}$ with subscript fractions indicating the z translation of the blocks within the hexagonal unit cell [101]. In the case of Bi_2Te_2S, the S atoms are substituted at the Te_1 sites [102].

In order to understand how the electronic transport properties of multiphase $Bi_2Te_{2.5}S_{0.5}$ are influenced by the microstructure, micro-texture and fractions of individual phases, accurate phase discrimination is an essential first step. However, the above close correspondence in the crystal structure and lattice parameters of Bi_2Te_3 and Bi_2Te_2S renders phase discrimination via electron back-scattering diffraction patterns impossible[1].

In this regard, energy dispersive X-ray spectroscopy (EDS) coupled with EBSD provides the appropriate solution. Here the user pre-defines reference spectra corresponding to the unique chemistries of each phase prior to mapping. Consequently, when the electron beam rasters across the sample surface during mapping, the characteristic X-rays emitted at each dwell point (based on a user-defined step size) first identify a phase based on its unique chemistry; following which the indexing of the electron back-scattering diffraction pattern is undertaken. In the case of Bi_2Te_3 and Bi_2Te_2S, their reference spectra are distinct enough to effectively discriminate the two phases during map acquisition.

In cases when reference spectra are not distinct to discriminate phases during map acquisition, post-processing of EBSD map is undertaken to segment the phases. In this past, phase segmentation often relied on thresholding or multi-peak mathematical modelling of the frequency distribution of the

[1] As a general rule of thumb, effective phase discrimination using electron back-scattering diffraction patterns is only possible when individual phases have either distinct crystal structures or a minimum ~10% difference in their lattice parameters [101].

band contrast (BC, or image/pattern quality, IQ, PQ) or band slope (BS) of the acquired electron backscattering patterns (EBSPs) or the size, aspect ratio, internal misorientation and boundary misorientation profiles of subgrains/grains [104-107]. While these methods have been reviewed in detail in Ref.[108], the main drawbacks of phase segmentation using EBSD –based parameters are summarised as follows. (i) Since each EBSD map tends to be unique based on microscope set-up and map acquisition parameters, it causes issues when delineating unique greyscale contrast ranges (in the case of BC/IQ/PQ/BS thresholding) for the various phases over multiple samples. (ii) Sub-dividing IQ/PQ/BC distributions based on multi-peak mathematical modelling is based on the assumption that each phase comprises symmetric, Gaussian sub-distributions and does not provide any means to account for overlaps between phases in the distributions

Alternatively, a recently developed segmentation methodology discriminated granular bainite and bainitic ferrite (phases whose crystal structure and lattice parameters are very similar to alpha-iron) during the post-processing of a combined EDS+EBSD map of a transformation induced plasticity steel [108]. The variation in carbon-K counts in the X-ray emission data between granular bainite and bainitic ferrite was exploited via a combination of: (i) grayscaling, (ii) image binarising, (iii) inverting the binary image, (iv) local neighbourhood density thresholding and dilation of individual pixels and (v) median filtering; in order to effectively discriminate them.

In Ref. [108] Monte-Carlo simulations of electron beam-sample interactions showed that even though carbon (a low density element at 2.267 gm/cm^3) was used to segment the phases, the carbon X-ray emission data: (i) was obtained from localised volumes were smaller than the smallest resolved substructures. (ii) did not suffer from plural scattering events arising from neighbouring phases and, (iii) did not contain channelling artefacts as anomalously high X-ray emissions and strong preferred orientations were absent.

While Ref. [108] clearly showed that phase discrimination using low density elemental data is possible, no analyses of the absolute error associated with the segmentation methodology was undertaken. Thus, the present case study of Bi_2Te_3 and Bi_2Te_2S provides an ideal opportunity to critically assess the efficacy of the segmentation methodology as a means to discriminate phases. The counts of the sulphur-K peak in the X-ray emission data (sulphur is a similarly low density element at 2.067 gm/cm^3) are significantly higher for Bi_2Te_2S compared to Bi_2Te_3. Consequently, the segmentation methodology can be used to exploit the variation in the sulphur X-ray emission data and enable phase discrimination via post-processing the image of the elemental map. In this chapter, the efficacy of the segmentation methodology assessed through application to the $Bi_2Te_{2.5}S_{0.5}$ alloy system to discriminate the Bi_2Te_3 and Bi_2Te_2S phases. Comparing the phase maps obtained after map acquisition and segmentation on a per-pixel basis shows that when the segmentation parameters are optimised, the absolute error in phase discrimination via segmentation is ~5%.

5.1 Combined EDS+EBSD mapping

Combined EDS+EBSD mapping was undertaken for a 485.95 × 368.70 μm^2 area in the centre of the $Bi_2Te_{2.5}S_{0.5}$ surface using a JEOL JSM-7001F field emission gun – scanning electron microscope operating at 15 kV accelerating voltage and ~5.5 nA probe current. X-ray emission spectra and electron back-scattering diffraction patterns were collected by the Oxford Instruments (OI) 80 mm^2 X-Max EDS and Nordlys-S(II) EBSD detectors, respectively; both of whom interface with the Oxford Instruments Aztec software suite.

The EBSD mapping conditions were optimised prior to mapping by assigning 49 and 46 reflectors for the Bi_2Te_3 and Bi_2Te_2S phases respectively, 4×4 binning, 1 background frame, a Hough resolution of 60 while concurrently indexing up to 8 bands of individual electron back-scattering patterns via the "Refined Accuracy" algorithm. The obtained EBSD achieved an overall indexing rate of 94.37% with most zero solutions occurring at grain boundaries.

A step size of ~0.24 μm was equivalent to an EDS map resolution of 2040 × 1530 pixels. A 20 keV energy range, auto-selection of number of channels, a process time of 3 and detector dead time of ~48-55% were used during mapping. Reference spectra corresponding to the unique chemistries of each phase were obtained prior to EDS+EBSD mapping (Fig. 5.1a). Sulphur is present in both phases due to its ease of diffusion at the temperatures imposed during sample fabrication. Over the full 'TruMap' area, the sulphur-K counts returned a Gaussian distribution (relative frequency versus counts per second (cps)) with the highest and maximum count rates of 1,450 cps and 21,650 cps respectively. When multiplied by the mean dwell time of 0.0247 s/pixel, 36 and 534 counts were returned as the highest and maximum counts, respectively.

5.2 Post-processing of the combined EDS+EBSD map

The EBSD map was cleaned using the OI Channel-5 software suite via methods described elsewhere [108-110]. Wild orientation spikes were eliminated and zero solutions filled-in through cyclic extrapolation down to 5 neighbours. Herein, low-angle grain boundaries (LAGBs) are defined as misorientations between 2° to 15° and high-angle grain boundaries (HAGBs) as misorientations >15°. Subgrain reconstruction involved setting a minimum misorientation angle of 2° to improve the angular resolution limit and retain orientation contrast information. A constant minimum spatial resolution of 7 times the nominal step size was maintained to define the smallest substructure. The post-processed phase map (Fig. 5.1c) was binarised as shown in Fig. 5.1d. The latter figure was used to calculate the absolute error in the phase maps obtained by segmentation (Fig. 5.2). The segmentation methodology and subsequent absolute error analysis is detailed in the following sections.

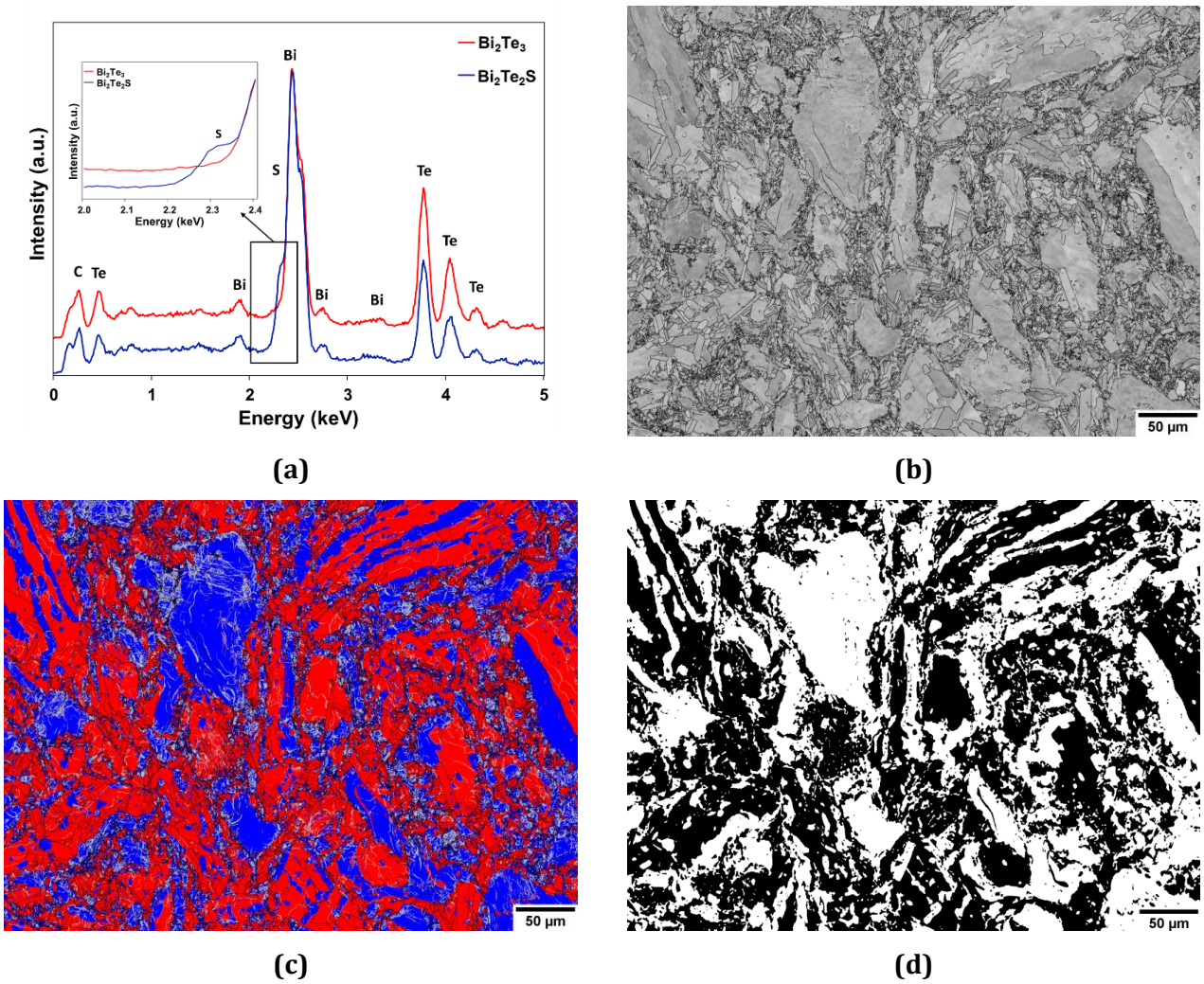

Figure 5.1: (a) Reference EDS spectra of Bi_2Te_3 (red) and Bi_2Te_2S (blue) obtained prior to mapping and used to distinguish the phases during combined EDS+EBSD mapping. (b) Band contrast and (c) phase distribution maps of Bi_2Te_3 (red) and Bi_2Te_2S (blue). (d) Binarised phase distribution map of Bi_2Te_3 (black) and Bi_2Te_2S (white). In (c), LAGBs = silver, HAGBs = black. The map in (d) is the reference phase map used to calculate the absolute error in the phase map obtained from segmentation (Fig. 5.2e) on a per-pixel basis.

5.3 Phase discrimination via segmentation of the sulphur X-ray emission map

Fig. 5.2 is representative of an example workflow for phase discrimination via segmentation[2]. The sulphur-K map obtained in OI Channel-5 was exported as a TIFF image (Fig. 5.2a). Thereafter, the image was imported into Gatan DigitalMicrograph in order to undertake phase discrimination via the freeware scripts [111] as follows. Grayscaling of the image was achieved by converting from RGB to a real image using the intensity of the green colour channel (Fig. 5.2b).

[2] The images shown in Figs. 5.2c-5.2e were obtained using the optimised conditions described in Table 1 and highlighted in gray.

The “Interactive Thresholding” script was used to limit the grayscale threshold between 200 and 255. Thereafter, the image was binarised by assigning values of 0 and 1 to black and white pixels, respectively. The “Invert Image Contrast” script was then used to invert the binary image (Fig. 5.2c).

Following this, the “Local Neighbourhood Density Threshold and Dilation” script was invoked. In this step, a local neighbourhood surrounding a pixel of interest (placed in the centre of a square grid) is defined as a 3×3 matrix of 8 first neighbour pixels, 5×5 matrix of 8+16=24 first and second neighbour pixels or a 7×7 matrix of 8+16+24=48 first, second and third neighbour pixels and so on. The user-defined neighbourhood size determines the neighbourhood search perimeter in which thresholding occurs.

For example, employing a local neighbourhood density threshold within 7×7 neighbourhood matrix investigates all 8 first neighbour pixels as well as pixels along the horizontal, vertical and diagonals of the second, third and other neighbours are interrogated. If a user defined density of white pixels are found within the search perimeter, the central pixel is assigned as a white pixel. Alternatively, if a user defined density of white pixels are not found within the search perimeter, the central pixel is assigned as a black pixel. Fig. 5.2d shows the result of the application of a local neighbourhood threshold of 1 in a 3×3 neighbourhood matrix to the inverted binary map in Fig. 5.2c. Following local neighbourhood density thresholding, a dilation kernel may or may not be applied around the central white pixel. During dilation, the binary value of each pixel is investigated. If the pixel in question has a binary value of 1 (i.e. the pixel is white), a dilation kernel is applied which expands the pixel size. For example, a dilation kernel of 3 means that a 3×3 matrix of 8 first neighbour pixels, as well as the central white pixel, are designated as white pixels. If the investigated pixel has a value of 0 (i.e. the pixel is black), no dilation occurs. Finally, the “Median Filter” script was applied to all combinations with a filter size of 3. Each pixel is filtered by taking the binary value of pixels in a surrounding 3×3 pixel matrix, sorting them in order and replacing its value with the median of pixel values (i.e. the central pixel). This acts to tidy up the edges and remove any remaining black pixels within white regions (Fig. 5.2e).

Since this study aims to assess the efficacy of segmentation, various combinations of neighbourhood matrix size, neighbourhood density threshold and dilation kernel size were applied (Table 5.1) to the TIFF image of the sulphur-K map (Fig. 5.2c). It should be noted that the grayscale threshold range of 200 to 255 at the beginning of segmentation and the median filter size of 3 applied at the end of segmentation was kept constant.

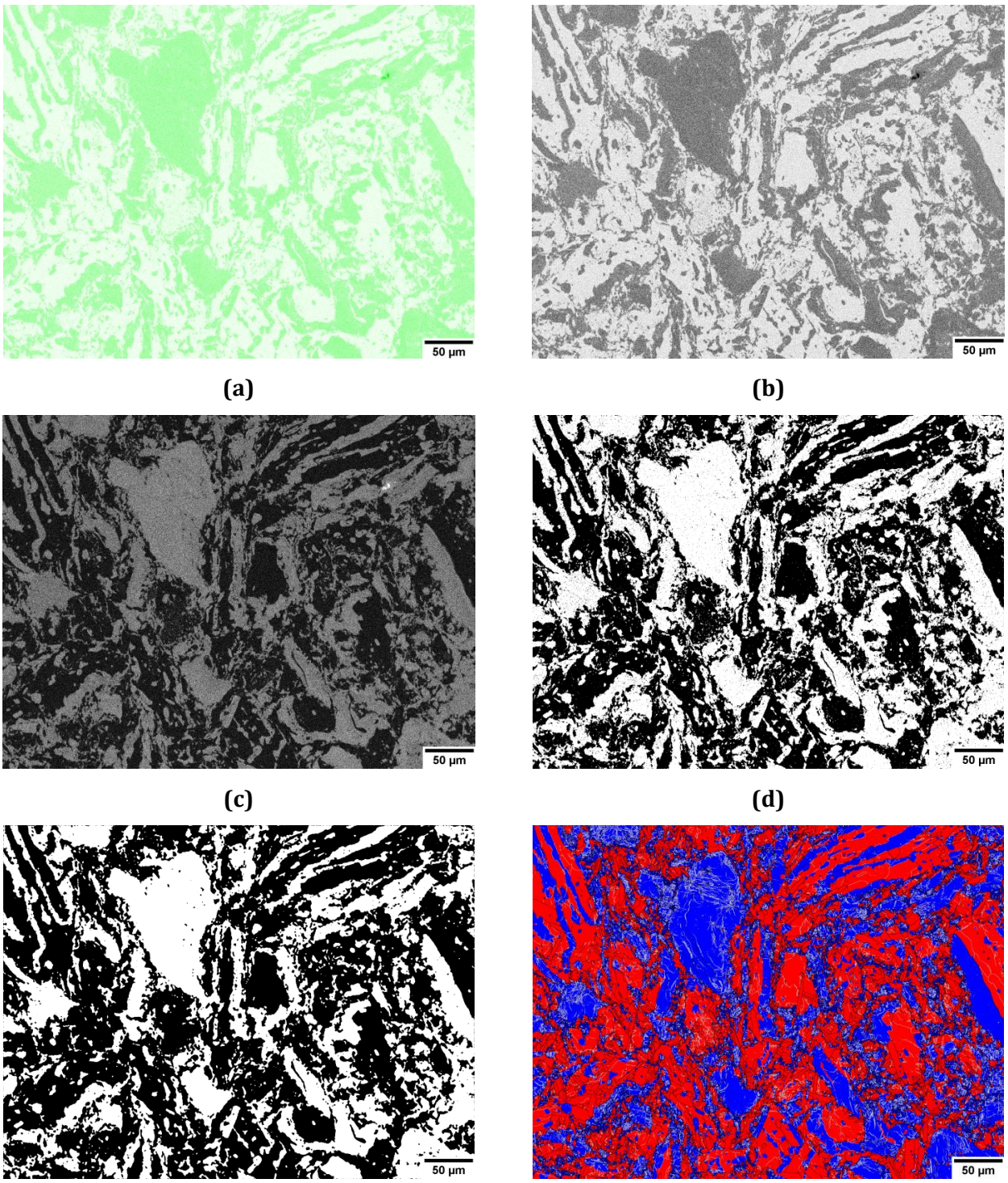

Figure 5.2: An example workflow for phase discrimination via segmentation. (a) The TIFF image of the map of relative distribution of sulphur-K counts imported into Gatan DigitalMicrograph. (b) Greyscaling of the image in (a). (c) Interactive thresholding between 200 and 255, binarising and inverting the contrast of the image in (b). (d) Applying a local neighbourhood density threshold of 1 white pixel in a 3×3 neighbourhood matrix of 8 first neighbour pixels to the image in (c). (e) Applying a median filter of size 3 to the image in (d). (f) Re-assigning white and black pixels as red (Bi_2Te_3) and blue (Bi_2Te_2S) for qualitative comparison with Fig. 5.1c. In (f), LAGBs = silver, HAGBs = black.

Table 5.1: The various combinations of neighbourhood matrix size, neighbourhood density threshold and dilation kernel size applied to the sulphur-K map shown in Fig. 5.2c. The absolute error in the phase map obtained from segmentation of the sulphur-K map was determined by computing the absolute difference between it and the reference phase map obtained by combined EDS+EBSD (Fig. 5.1d) on a per-pixel basis.

Neighbourhood matrix	Neighbourhood density threshold	Dilation kernel size	Absolute Error (%)
3×3	1	0	5.3
		3	12.6
		5	20.6
	2	0	7.2
		3	7.5
	3	0	15.8
		3	5.7
5×5	1	0	6.4
		3	9.4
	2	0	14.1
		3	6.1
	3	0	31.2
		3	9.1
7×7	1	0	9.3
		3	8.1
	2	0	30.0
		3	7.7
	3	0	40.2
		3	15.6

The absolute error in the phase map from segmentation (Table 5.1) was determined by calculating the absolute difference between this segmented map and the reference phase map obtained by combined EDS+EBSD (Fig. 5.1d) on a per-pixel basis using the 'Image Calculator' function in ImageJ. The absolute difference between Figs. 5.1d and 5.2e resulted in the image shown in Fig. 5.3a. The resultant image contains white pixels wherever a mismatch in binary pixels was detected in Figs. 5.1d and 5.2e. Consequently, the absolute error is defined as a percentage of the number of mismatched white pixels to the total number of pixels (Table 5.1).

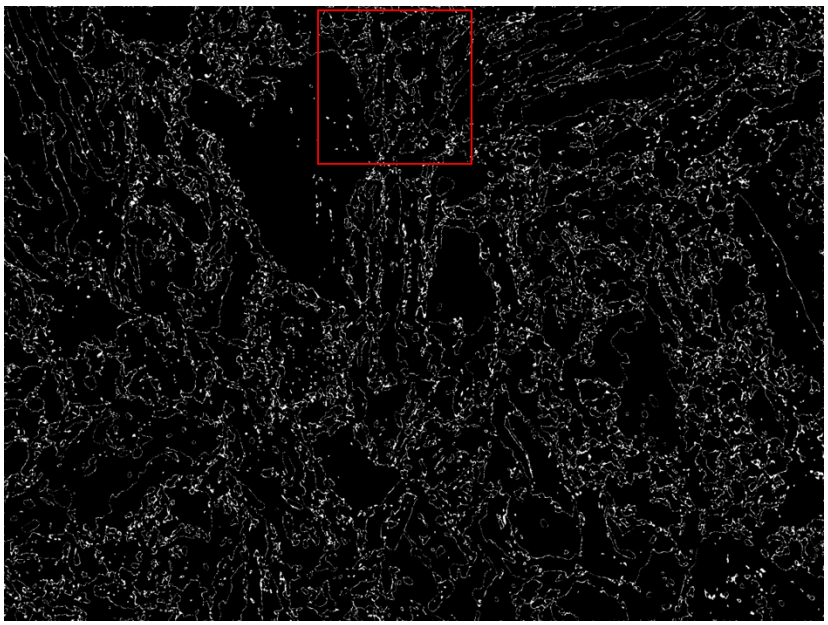

(a)

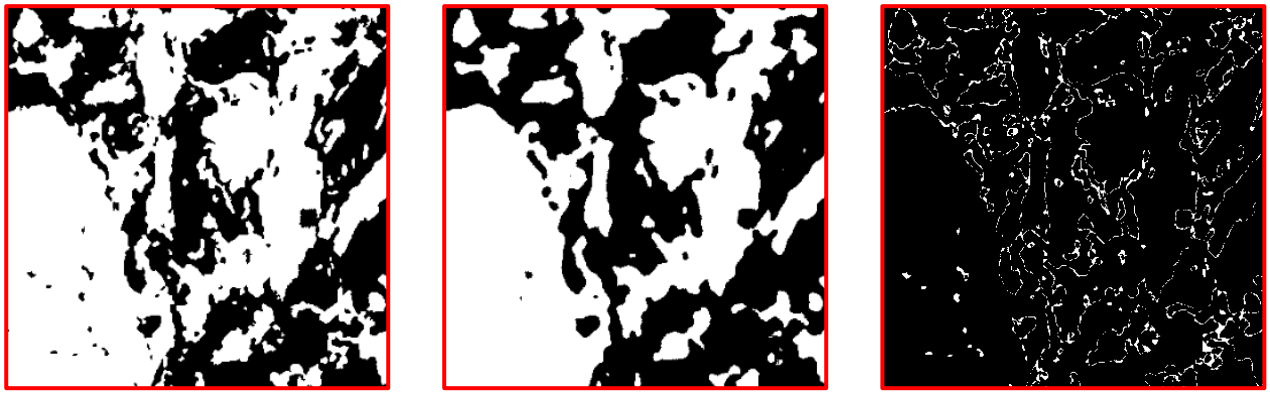

(b)

Figure 5.3: (a) The resultant absolute difference image obtained from Fig. 1d (the reference phase map) and Fig. 2e (the phase map from segmentation) on using the 'Image Calculator' function in ImageJ. (b) Zoomed-in views of regions highlighted in red in Figs. 1d (far left) and 2e (middle) that result in the absolute difference image (far right). The absolute difference image (far right) returns black pixels when the images on the far left and middle are equivalent and white pixels when they differ.

5.3 Considerations of combined EDS+EBSD mapping

During conventional EDS mapping the electron beam rasters over an area of interest multiple times for a fixed time period or a user-defined number of counts in order to obtain statistically relevant information on elemental distribution. On the other hand, during combined EDS+EBSD mapping the beam rasters over an area of interest only once for a given mean dwell time per pixel.

Given the high sample tilt, the associated interaction volume effects and the rather limited EDS-data acquisition conditions, the absolute elemental counts recorded by the phases during

combined EDS+EBSD may be prone to error. However, despite the limitations imposed by combined EDS+EBSD mapping, when phases have similar crystal structures and lattice parameters, the relative variation in their elemental counts can be exploited to effectively discriminate them. Thus, given optimised EDS+EBSD acquisition parameters and unique phase chemistries, even a relatively low-density element (sulphur-K in the present study) can be used to successfully undertake phase discrimination during mapping (Fig. 5.1c).

5.4 The efficacy of the segmentation methodology

The value of the absolute error associated with phase discrimination via the segmentation methodology is heavily dependent on the user-defined thresholds for grayscaling of the initial sulphur-K map (Fig. 5.2c), the neighbourhood matrix size, the neighbourhood density threshold and the dilation kernel size (Fig. 5.2d). The absolute errors associated with various combinations of thresholding parameters are listed in Table 5.1. It should be noted that although a range of grayscale thresholds were applied to this image, they are not reported here. All subsequent analyses and absolute error calculations are based on a grayscale threshold between 200 and 255, as this threshold returned the lowest absolute error following segmentation.

As shown in Table 1, larger absolute errors can most commonly associated with large neighbourhood density thresholds, dilation kernel sizes and neighbourhood matrix sizes. The neighbourhood density threshold is particularly sensitive at interfaces of high and low sulphur counts (Fig. 5.2a); which in turn correspond to the Bi_2Te_2S and Bi_2Te_3 phases (Figs. 5.1c and 5.2f) as well as white and black pixels (Figs. 5.1d and 5.2e). In the interests of simplifying explanations, the following discussion refers to white and black pixels only.

Fig. 5.4a shows a zoomed-in view of a region of interest from the binarised reference phase map shown in Fig. 5.1d. The former will be used to discuss the implications of increasing the neighbourhood matrix sizes, neighbourhood density thresholds and dilation kernel sizes when segmenting for phase discrimination.

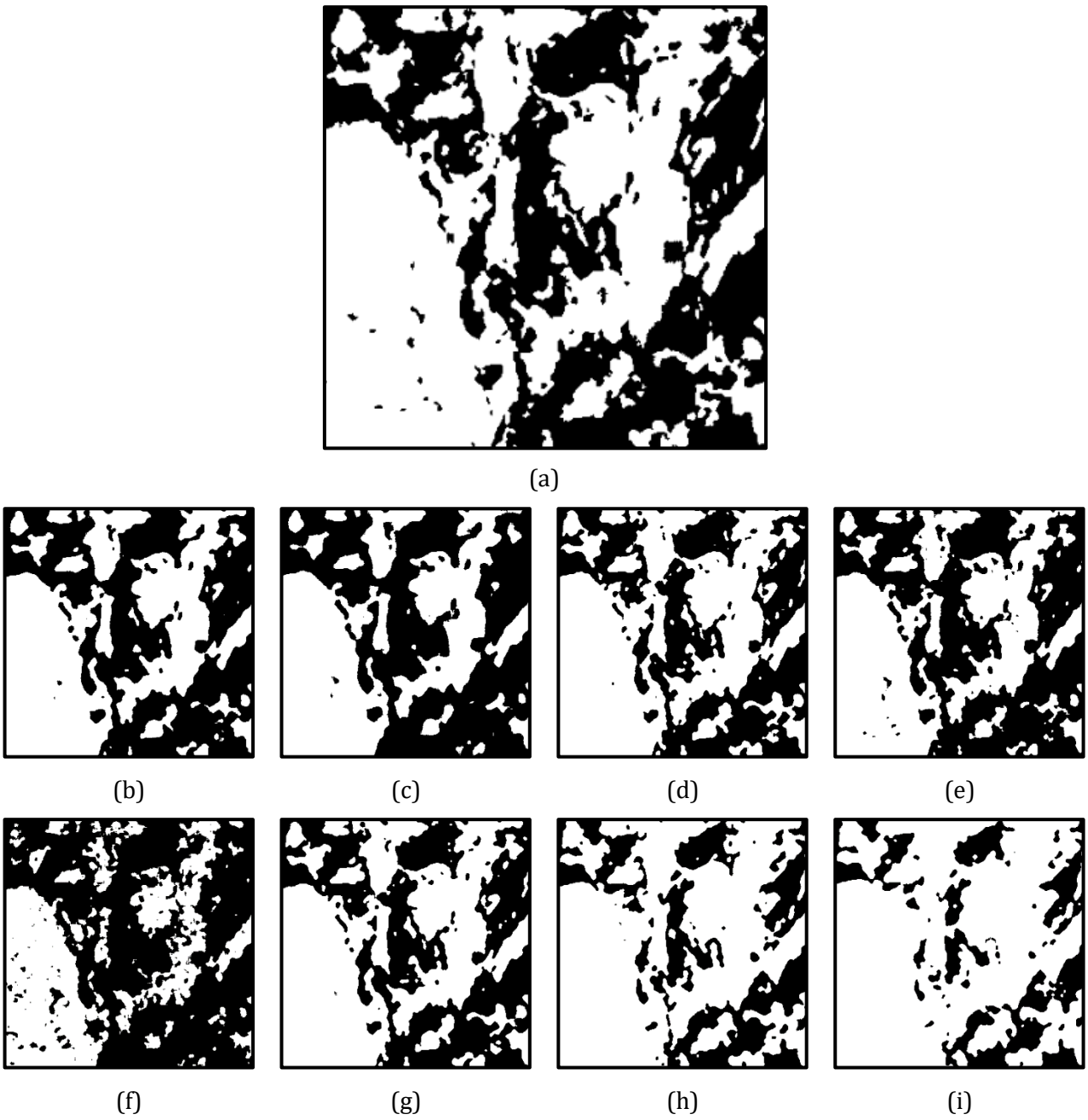

Figure 5.4: (a) A zoomed-in view of a region taken from the binarised reference phase map shown in Fig. 1d. (b, c) The equivalent region when a neighbourhood density threshold of 1, no dilation kernel, and a 5×5 and 7×7 neighbourhood matrix size are respectively used for phase segmentation. (d-f) The equivalent region when a 3×3 neighbourhood matrix size, no dilation kernel and a neighbourhood density threshold of 1, 2 and 3 are respectively used for phase segmentation. (g) The equivalent region when a neighbourhood density threshold of 3, a 3×3 neighbourhood matrix size and a dilation kernel size of 3 is used for phase segmentation. (h, i) The equivalent region when a neighbourhood density threshold of 1, a 3×3 neighbourhood matrix size and a dilation kernel size of 3 and 5 are respectively used for phase segmentation. A median of size 3 was applied to all maps shown.

The use of neighbourhood matrix sizes larger than 3×3 appeared to have limited success; regardless of the associated neighbourhood density threshold and dilation kernel applied thereafter. For example, Figs 5.4b and 5.4c are representative examples of the results obtained when a 5×5 and 7×7 neighbourhood matrix sizes are applied within which a neighbourhood density threshold of 1 was used. No kernel dilation was applied thereafter. It is evident that as the neighbourhood matrix size increases, contiguous white pixel regions shrink while approximately retaining their interfaces. The absolute error involved with larger neighbourhood matrix sizes often improves when coupled with neighbourhood density thresholds greater than 2 (Table 5.1). However, in this case, the interfaces are compromised.

Figs. 5.4d to 5.4f are representative examples of the results obtained when a 3×3 neighbourhood matrix size within which neighbourhood density thresholds of 1, 2 and 3, respectively are applied. No kernel dilation was applied thereafter. In general, while larger neighbourhood density thresholds retain the size and shape of coarse, contiguous white pixel regions, the regions comprising small groups of white pixels are often eliminated. Compared to Fig. 5.4a, it is immediately apparent that the fraction of black pixels increases steadily with increasing neighbourhood density threshold values (Figs. 5.4d to 5.4f). To serve as a further example, in Figs. 5.4e and 5.4f, significant erosion of white pixels is apparent both at interfaces (edges comprising border regions of white and black pixels) and within contiguous white pixel regions. It follows that Figs. 5.4e and 5.4f subsequently return higher absolute error values compared to Fig. 5.4d (Table 5.1).

It is pointed out that larger neighbourhood density thresholding can still result in reduced absolute errors of ~≤10% when a dilation kernel is used thereafter (Table 5.1). For instance, if the results obtained when a 3×3 neighbourhood matrix size within which a neighbourhood density threshold of 3 is applied, followed by dilation kernel size of 3, the absolute error improves by ~10% (compare absolute errors of 15.8% and 5.7% in Table 1). However, it must be understood that while the absolute error is reduced, the integrity of interfaces is often severely compromised (Fig. 5.4g). In this case, it is the responsibility of the user to determine whether large neighbourhood density thresholding followed by application of a dilation kernel is suitable for the data set in question.

Figs. 5.4h and 5.4i are representative examples of the results obtained when a 3×3 neighbourhood matrix size within which a neighbourhood density threshold of 1 is applied, followed by dilation kernel sizes of 3 and 5, respectively. Compared to Fig. 5.4a, the application of a small neighbourhood density threshold coupled with larger dilation kernel sizes greatly exaggerates the size of coarse contiguous, white pixel regions by promoting the coalescence and incorporation of small groups of white pixels into them (Figs. 5.4h and 5.4i).

Table 1 shows that the application of dilation kernels can result in reduced absolute errors when neighbourhood density thresholds of 2 or higher are applied. As discussed previously, the

application of large neighbourhood density thresholds can erroneously reduce the fraction of white pixels while severely compromising interfaces. Thereafter, the use of large dilation kernel sizes merely serves to compensate for the loss of white pixels from the previous neighbourhood density threshold step while retaining the erroneous interfaces. It was deemed unnecessary to report the absolute error associated with the application of a dilation kernel size of 5 for the majority of cases due to its tendency to visibly and severely compromise the boundary interface between the two phases.

For all combinations of parameters shown in Table 1, the application of a median filter of size 3 constituted the final step of the segmentation methodology. If a median filter were not applied, an erroneously large density of black pixels within white regions or vice-versa would remain in the segmented image. The application of median filters greater than 3 were also tested, and disregarded due to the elimination of an erroneously high fraction of fine white pixel regions. A comparison of Figs. 5.2d and 5.2e highlights the necessity of applying a median filter; such that a filter size 3 effectively removes artefacts and smooths interfaces. It should also be noted that while median filtering may have the adverse effect of reducing or eliminating small pixel groups, the overall accuracy of the segmented image is improved following median filtering. For example, prior to the application of a median filter, the segmented phase map (Fig. 5.2d) had an absolute error of 7.45% relative to the reference phase map. Upon applying a median filter of size 3, the absolute error reduced to 5.3%.

The above assessment of the parameters employed during the segmentation methodology suggests that user discretion is required to ensure the smallest absolute error between the segmented and reference phase maps. However, for an optimised combination of segmentation parameters (as detailed in Section 3), an absolute error of ~5% between the segmented and reference phase maps can be returned. Error is most commonly localised in the 2-4 pixel region at the boundary interface between phases. In the context of this study, the error is detrimental for fine sulphur-rich regions and is in part, attributed to the large area of the EBSD map and the employed step size. In cases where interface integrity is particularly important, EBSD maps should be acquired using lower accelerating voltage and probe current at higher magnification and even smaller step sizes. It follows that such an approach would be a suitable means to reduce the absolute error associated with phase segmentation even further. This result, and the strategy to further reduce the absolute error, demonstrates the overall efficacy of the segmentation methodology as a means to discriminate phases via the post-processing of elemental maps.

Chapter 6

Concluding Summary

In summary, two case studies have been presented that highlight the pivotal role that advanced microscopy has in the investigation of TE systems.

The primary case study illuminated the influence of TE device operational temperatures (~823 K) on the microstructure multiphase quaternary $Pb_{0.97}Na_{0.03}Te_{0.65}S_{0.25}Se_{0.1}$, and how these changes corresponded to the electronic transport properties of the material. It was found that the TE performance of the alloy proved to be stable with a zT of ~1.7-1.9 in the 700-850 K temperature range over the course of thermal ageing at 823 K for up to 8 weeks. It was shown that despite the constantly evolving microstructure of the alloy during thermal ageing, the presence of nanoscale precipitates after 1-2 weeks of thermal ageing had little impact on the lattice thermal conductivity of the alloy at operational temperatures. The dissolution of precipitates and redistribution of dopant between phases above ~630 K is understood to explain the variation in resistivity above ~630 K for aged samples. The balance of increasing resistivity and reduced total thermal conductivity as ageing times increase appears to allow the alloy to maintain an impressive zT in the 700-850 K temperature range for all investigated ageing times. This finding reinforced prior studies [11], highlighting the importance of employing a suitable fabrication method to maintain TE performance over extended time periods at operational temperatures.

The secondary case study presented in this thesis described a phase segmentation methodology capable of distinguishing the structurally similar yet chemically unique phases of Bi_2Te_3 and Bi_2Te_2S. The efficacy of the employed phase segmentation methodology was assessed by comparing phase segmented maps to reference phase maps obtained through combined EDS+EBSD mapping. It was determined that during application of the phase segmentation methodology, the most significant factors influencing the efficacy of the segmentation process were associated with the neighbourhood matrix size, neighbourhood density threshold and dilation kernel applied to the initial sulphur-K map required for segmentation. Once optimised, phase maps obtained via the described phase segmentation methodology achieved an absolute error of ~5% in relation to the reference phase map. The phase segmentation methodology described provides an alternative approach to the segmentation of phases for EBSD analysis, enabling comprehensive texture analysis and correlation to TE properties for future studies of multiphase TE materials.

Future Work

The findings of this thesis and the literature investigating multiphase quaternary lead chalcogenides [11, 15, 50, 83, 84] provides a comprehensive insight into the behaviour of phase boundaries and the distribution of *p*-type dopant sodium between the PbTe-rich matrix and PbS-rich precipitates. Equivalent studies for *n*-type quaternary lead chalcogenides could provide further valuable insight into TE design. However, due to the comparatively lower maximum *z*T achieved for *n*-type quaternary lead chalcogenides [25], only limited studies have been conducted. An effort to understand phonon scattering mechanisms in potassium doped PbTe, PbSe and PbS highlighted reduced lattice thermal conductivities when compared to sodium doped analogues [112]. This study emphasised the relationship between precipitate size and morphology on lattice thermal conductivity reductions via phonon scattering. Further studies could involve similarly investigating *n-type* quaternary lead chalcogenides. Augmenting this with atom probe tomography would provide detailed insight how the nature of nanoscale precipitates, phase boundaries and the diffusion of *n*-type dopants influence the TE properties of the system.

References

[1] J. Pawelski, P07440: Next Generation Thermo-Electric Systems - Family of Projects, RIT, Multidisciplinary Engineering @ RIT, 2006.
[2] T.M. Tritt, M.A. Subramanian, Thermoelectric Materials, Phenomena, and Applications: A Bird's Eye View, MRS Bull., 31 (2006) 188-198.
[3] L.-D. Zhao, V.P. Dravid, M.G. Kanatzidis, The panoscopic approach to high performance thermoelectrics, Energy Environ. Sci., 7 (2014) 251-268.
[4] G.J. Snyder, E.S. Toberer, Complex thermoelectric materials, Nature Materials, 7 (2008) 105-114.
[5] S. Aminorroaya Yamini, H. Wang, Z.M. Gibbs, Y. Pei, S.X. Dou, G.J. Snyder, Chemical composition tuning in quaternary p-type Pb-chalcogenides–a promising strategy for enhanced thermoelectric performance, Phys. Chem. Chem. Phys., 16 (2014) 1835-1840.
[6] A.A. Volykhov, L.V. Yashina, V.I. Shtanov, Phase relations in pseudobinary systems of germanium, tin, and lead chalcogenides, Inorg. Mater., 42 (2006).
[7] S. Aminorroaya Yamini, H. Wang, Z.M. Gibbs, Y. Pei, D.R. Mitchell, S.X. Dou, G.J. Snyder, Thermoelectric performance of tellurium-reduced quaternary p-type lead–chalcogenide composites, Acta Mater., 80 (2014) 365-372.
[8] H. Jiaqing, G.K. Mercouri, P.D. Vinayak, High performance bulk thermoelectrics via a panoscopic approach, Materials Today, 16 (2013).
[9] S.N. Girard, J. He, C. Li, S. Moses, G. Wang, C. Uher, V.P. Dravid, M.G. Kanatzidis, In Situ Nanostructure Generation and Evolution within a Bulk Thermoelectric Material to Reduce Lattice Thermal Conductivity, Nano Lett., 10 (2010) 2825-2831.
[10] S. Aminorroaya Yamini, A.Z. Williams, D. Attard, G. Dou, G.J. Snyder, Thermoelectric Properties and Microstructure Studies of Spinodally Decomposed PbTe0. 38S0. 62 Alloy, Science of Advanced Materials, 6 (2014) 1453-1459.
[11] S. Aminorroaya Yamini, M. Brewis, J. Byrnes, R. Santos, A. Manettas, Y.Z. Pei, Fabrication of thermoelectric materials - thermal stability and repeatability of achieved efficiencies, J. Mater. Chem. C, 3 (2015) 10610-10615.
[12] H. Wu, F. Zheng, D. Wu, Z.-H. Ge, X. Liu, J. He, Advanced electron microscopy for thermoelectric materials, Nano Energy, 13 (2015) 626-650.
[13] S.I. Kim, K.H. Lee, H.A. Mun, H.S. Kim, S.W. Hwang, J.W. Roh, D.J. Yang, W.H. Shin, X.S. Li, Y.H. Lee, G.J. Snyder, S.W. Kim, Dense dislocation arrays embedded in grain boundaries for high-performance bulk thermoelectrics, Science, 348 (2015) 109-114.
[14] J. He, I.D. Blum, H.-Q. Wang, S.N. Girard, J. Doak, L.-D. Zhao, J.-C. Zheng, G. Casillas, C. Wolverton, M. Jose-Yacaman, D.N. Seidman, M.G. Kanatzidis, V.P. Dravid, Morphology Control of Nanostructures: Na-Doped PbTe-PbS System, Nano Lett., 12 (2012) 5979-5984.
[15] S. Aminorroaya Yamini, D.R. Mitchell, Z.M. Gibbs, R. Santos, V. Patterson, S. Li, Y.Z. Pei, S.X. Dou, G. Jeffrey Snyder, Heterogeneous Distribution of Sodium for High Thermoelectric Performance of p-type Multiphase Lead-Chalcogenides, Adv. Energy Mater., 5 (2015).
[16] H.-S. Kim, Z.M. Gibbs, Y. Tang, H. Wang, G.J. Snyder, S.G. J., T.E. S., Characterization of Lorenz number with Seebeck coefficient measurement, APL Materials, 3 (2015) 041506.
[17] H.J. Goldsmid, The Thermoelectric and Related Effects, Introduction to Thermoelectricity, Springer Berlin Heidelberg, Berlin, Heidelberg, 2010, pp. 1-6.
[18] L.E. Bell, Cooling, heating, generating power, and recovering waste heat with thermoelectric systems, Science, 321 (2008) 1457-1461.
[19] T.M. Tritt, Thermoelectric Phenomena, Materials, and Applications, Annual Review of Materials Research, 41 (2011) 433-448.
[20] C. Han, Z. Li, S. Dou, Recent progress in thermoelectric materials, Chin. Sci. Bull., 59 (2014) 2073-2091.
[21] S.M. Sze, Physics of Semiconductor Devices, John Wiley & Sons, 1981.
[22] I.U.I. Ravich, B.A. Efimova, I.A. Smirnov, Semiconducting Lead Chalcogenides [by] Yu. I. Ravich, B.A. Efimova, and I.A. Smirnov, Plenum Press, 1970.

[23] C.C. Lin, D. Ginting, R. Lydia, M.H. Lee, J.S. Rhyee, Thermoelectric properties and extremely low lattice thermal conductivity in p-type Bismuth Tellurides by Pb-doping and PbTe precipitation, Journal of Alloys and Compounds, 671 (2016) 538-544.
[24] Y. Cao, X. Zhao, T. Zhu, X. Zhang, J. Tu, Syntheses and thermoelectric properties of Bi2Te3/Sb2Te3 bulk nanocomposites with laminated nanostructure, Appl. Phys. Lett., 92 (2008).
[25] S. Aminorroaya Yamini, H. Wang, D. Ginting, D.R. Mitchell, S.X. Dou, G.J. Snyder, Thermoelectric Performance of n-Type (PbTe) 0.75 (PbS) 0.15 (PbSe) 0.1 Composites, ACS applied materials & interfaces, 6 (2014) 11476-11483.
[26] Q. Zhang, F. Cao, W. Liu, K. Lukas, B. Yu, S. Chen, C. Opeil, D. Broido, G. Chen, Z. Ren, Heavy doping and band engineering by potassium to improve the thermoelectric figure of merit in p-type PbTe, PbSe, and PbTe(1-y)Se(y), J. Am. Chem. Soc., 134 (2012) 10031-10038.
[27] S.N. Girard, J. He, X. Zhou, D. Shoemaker, C.M. Jaworski, C. Uher, V.P. Dravid, J.P. Heremans, M.G. Kanatzidis, High performance Na-doped PbTe-PbS thermoelectric materials: Electronic density of states modification and shape-controlled nanostructures, Journal of the American Chemical Society, 133 (2011) 16588-16597.
[28] Y.L. Pei, Y. Liu, Electrical and thermal transport properties of Pb-based chalcogenides: PbTe, PbSe, and PbS, Journal of Alloys and Compounds, 514 (2012) 40-44.
[29] Y. Zhang, X. Ke, P.R.C. Kent, J. Yang, C. Chen, Anomalous Lattice Dynamics near the Ferroelectric Instability in PbTe, Phys. Rev. Lett., 107 (2011) 175503.
[30] S. Kastbjerg, N. Bindzus, M. Søndergaard, S. Johnsen, N. Lock, M. Christensen, M. Takata, M.A. Spackman, B. Brummerstedt Iversen, Direct Evidence of Cation Disorder in Thermoelectric Lead Chalcogenides PbTe and PbS, Adv. Funct. Mater., 23 (2013) 5477-5483.
[31] E.S. Božin, C.D. Malliakas, P. Souvatzis, T. Proffen, N.A. Spaldin, M.G. Kanatzidis, S.J.L. Billinge, Entropically Stabilized Local Dipole Formation in Lead Chalcogenides, Science, 330 (2010) 1660-1663.
[32] T.C. Chasapis, Y. Lee, E. Hatzikraniotis, K.M. Paraskevopoulos, H. Chi, C. Uher, M.G. Kanatzidis, Understanding the role and interplay of heavy-hole and light-hole valence bands in the thermoelectric properties of PbSe, Physical Review B, 91 (2015).
[33] Y. Pei, H. Wang, G.J. Snyder, Band engineering of thermoelectric materials, Adv. Mater., 24 (2012) 6125-6135.
[34] A. Mehdizadeh Dehkordi, M. Zebarjadi, J. He, T.M. Tritt, Thermoelectric power factor: Enhancement mechanisms and strategies for higher performance thermoelectric materials, Materials Science and Engineering R: Reports, 97 (2015) 1-22.
[35] Y. Pei, A. Lalonde, S. Iwanaga, G.J. Snyder, High thermoelectric figure of merit in heavy hole dominated PbTe, Energy and Environmental Science, 4 (2011) 2085-2089.
[36] A.D. Lalonde, Y. Pei, H. Wang, G. Jeffrey Snyder, Lead telluride alloy thermoelectrics, Materials Today, 14 (2011) 526-532.
[37] A.D. LaLonde, Y. Pei, G.J. Snyder, Reevaluation of PbTe1-xIx as high performance n-type thermoelectric material, Energy & Environmental Science, 4 (2011) 2090-2096.
[38] Y. Pei, N.A. Heinz, A. LaLonde, G.J. Snyder, Combination of large nanostructures and complex band structure for high performance thermoelectric lead telluride, Energy & Environmental Science, 4 (2011) 3640-3645.
[39] H. Wang, E. Schechtel, Y. Pei, G.J. Snyder, High thermoelectric efficiency of n-type PbS, Adv. Energy Mater., 3 (2013) 488-495.
[40] E.G. Evola, M.D. Nielsen, C.M. Jaworski, H. Jin, J.P. Heremans, Thermoelectric transport in indium and aluminum-doped lead selenide, Journal of Applied Physics, 115 (2014) 053704.
[41] H. Wang, Y. Pei, A.D. Lalonde, G.J. Snyder, Heavily doped p-type PbSe with high thermoelectric performance: An alternative for PbTe, Adv. Mater., 23 (2011) 1366-1370.
[42] H. Wang, A.D. LaLonde, Y. Pei, G.J. Snyder, The Criteria for Beneficial Disorder in Thermoelectric Solid Solutions, Adv. Funct. Mater., 23 (2013) 1586-1596.
[43] Y. Pei, X. Shi, A. LaLonde, H. Wang, L. Chen, G.J. Snyder, Convergence of electronic bands for high performance bulk thermoelectrics, Nature, 473 (2011) 66-69.
[44] J. Androulakis, C.H. Lin, H.J. Kong, C. Uher, C.I. Wu, T. Hogan, B.A. Cook, T. Caillat, K.M. Paraskevopoulos, M.G. Kanatzidis, Spinodal decomposition and nucleation and growth as a means to bulk

nanostructured thermoelectrics: enhanced performance in Pb(1-x)Sn(x)Te-PbS, J. Am. Chem. Soc., 129 (2007) 9780-9788.
[45] C. Chang, Y. Xiao, X. Zhang, Y. Pei, F. Li, S. Ma, B. Yuan, Y. Liu, S. Gong, L.D. Zhao, High performance thermoelectrics from earth-abundant materials: Enhanced figure of merit in PbS through nanostructuring grain size, Journal of Alloys and Compounds, 664 (2016) 411-416.
[46] D. Wu, L.D. Zhao, X. Tong, W. Li, L. Wu, Q. Tan, Y. Pei, L. Huang, J.F. Li, Y. Zhu, M.G. Kanatzidis, J. He, Superior thermoelectric performance in PbTe-PbS pseudo-binary: Extremely low thermal conductivity and modulated carrier concentration, Energy and Environmental Science, 8 (2015) 2056-2068.
[47] L.D. Zhao, J. He, C.I. Wu, T.P. Hogan, X. Zhou, C. Uher, V.P. Dravid, M.G. Kanatzidis, Thermoelectrics with earth abundant elements: High performance p-type PbS nanostructured with SrS and CaS, Journal of the American Chemical Society, 134 (2012) 7902-7912.
[48] S. Johnsen, J. He, J. Androulakis, V.P. Dravid, I. Todorov, D.Y. Chung, M.G. Kanatzidis, Nanostructures boost the thermoelectric performance of PbS, Journal of the American Chemical Society, 133 (2011) 3460-3470.
[49] J. Androulakis, I. Todorov, J. He, D.Y. Chung, V. Dravid, M. Kanatzidis, Thermoelectrics from abundant chemical elements: High-performance nanostructured PbSe-PbS, Journal of the American Chemical Society, 133 (2011) 10920-10927.
[50] S. Aminorroaya Yamini, D.R.G. Mitchell, H. Wang, Z.M. Gibbs, Y. Pei, S.X. Dou, G.J. Snyder, Origin of resistivity anomaly in p-type leads chalcogenide multiphase compounds, AIP Advances, 5 (2015) 053601.
[51] M. Ohta, K. Biswas, S.-H. Lo, J. He, D.Y. Chung, V.P. Dravid, M.G. Kanatzidis, Enhancement of Thermoelectric Figure of Merit by the Insertion of MgTe Nanostructures in p-type PbTe Doped with Na2Te, Adv. Energy Mater., 2 (2012) 1117-1123.
[52] P. Lu, X. Wang, M. Lu, Largely enhanced thermoelectric properties of the binary-phased PbTe-Sb 2Te 3 nanocomposites, J. Mater. Res., 27 (2012) 734-739.
[53] L.D. Zhao, H.J. Wu, S.Q. Hao, C.I. Wu, X.Y. Zhou, K. Biswas, J.Q. He, T.P. Hogan, C. Uher, C. Wolverton, V.P. Dravid, M.G. Kanatzidis, All-scale hierarchical thermoelectrics: MgTe in PbTe facilitates valence band convergence and suppresses bipolar thermal transport for high performance, Energy and Environmental Science, 6 (2013) 3346-3355.
[54] L.D. Hicks, M.S. Dresselhaus, Effect of quantum-well structures on the thermoelectric figure of merit, Physical Review B, 47 (1993) 12727-12731.
[55] S.I. Kim, K.H. Lee, H.A. Mun, H.S. Kim, S.W. Hwang, J.W. Roh, D.J. Yang, W.H. Shin, X.S. Li, Y.H. Lee, Dense dislocation arrays embedded in grain boundaries for high-performance bulk thermoelectrics, Science, 348 (2015) 109-114.
[56] H. Wang, J.H. Bahk, C. Kang, J. Hwang, K. Kim, J. Kim, P. Burke, J.E. Bowers, A.C. Gossard, A. Shakouri, W. Kim, Right sizes of nano- and microstructures for high-performance and rigid bulk thermoelectrics, Proc. Natl. Acad. Sci. U.S.A., 111 (2014) 10949-10954.
[57] B. Kanishka, H. Jiaqing, D.B. Ivan, I.W. Chun, P.H. Timothy, N.S. David, P.D. Vinayak, G.K. Mercouri, High-performance bulk thermoelectrics with all-scale hierarchical architectures, Nature, 489 (2012).
[58] P.A. Sharma, J.D. Sugar, Obstacles to applications of nanostructured thermoelectric alloys, Frontiers in Chemistry, 2 (2014) 111.
[59] J.R. Sootsman, D.Y. Chung, M.G. Kanatzidis, New and old concepts in thermoelectric materials, Angewandte Chemie - International Edition, 48 (2009) 8616-8639.
[60] Y. Lee, S.H. Lo, J. Androulakis, C.I. Wu, L.D. Zhao, D.Y. Chung, T.P. Hogan, V.P. Dravid, M.G. Kanatzidis, High-performance tellurium-free thermoelectrics: All-scale hierarchical structuring of p-type PbSe-MSe systems (M = Ca, Sr, Ba), Journal of the American Chemical Society, 135 (2013) 5152-5160.
[61] T. Ikeda, S.M. Haile, V.A. Ravi, H. Azizgolshani, F. Gascoin, G.J. Snyder, Solidification processing of alloys in the pseudo-binary PbTe–Sb2Te3 system, Acta Mater., 55 (2007) 1227-1239.
[62] J. Sui, J. Li, J. He, Y.-L. Pei, D. Berardan, H. Wu, N. Dragoe, W. Cai, L.-D. Zhao, Texturation boosts the thermoelectric performance of BiCuSeO oxyselenides, Energy & Environmental Science, 6 (2013) 2916-2920.
[63] D.B. Williams, C.B. Carter, Diffracted Beams, Transmission Electron Microscopy: A Textbook for Materials Science, Springer US, Boston, MA, 2009, pp. 221-233.

[64] J.R. Sootsman, J. He, V.P. Dravid, S. Ballikaya, D. Vermeulen, C. Uher, M.G. Kanatzidis, Microstructure and Thermoelectric Properties of Mechanically Robust PbTe-Si Eutectic Composites†, Chemistry of Materials, 22 (2010) 869-875.
[65] H.J. Wu, L.D. Zhao, F.S. Zheng, D. Wu, Y.L. Pei, X. Tong, J.Q. He, Understanding the Role of Potassium Doping in PbTe-PbS Thermoelectrics, Microsc. Microanal., 20 (2014) 506-507.
[66] C. Kang, H. Wang, H. Kim, S.J. Kim, W. Kim, Effect of excess Na on the morphology and thermoelectric properties of Na x Pb1-x Te0.85Se0.15, J. Electron. Mater., 43 (2014) 353-358.
[67] S. Aminorroaya Yamini, A.Z. Williams, D. Attard, G. Shi Xue Dou, G. Jeffrey Snyder, Thermoelectric properties and microstructure studies of spinodally decomposed PbTe0.38S0.62 alloy, Science of Advanced Materials, 6 (2014) 1453-1459.
[68] M.J. Hÿtch, E. Snoeck, R. Kilaas, Quantitative measurement of displacement and strain fields from HREM micrographs, Ultramicroscopy, 74 (1998) 131-146.
[69] I. Kudman, Thermoelectric properties of p-type PbTe-PbSe alloys, Journal of Materials Science, 7 1027-1029.
[70] Introduction to Crystallography (Sands, Donald E.), J. Chem. Educ., 72 (1995) A42.
[71] A.S. Pashinkin, M.S. Mikhailova, A.S. Malkova, V.A. Fedorov, Heat capacity and thermodynamic properties of lead selenide and lead telluride, Inorg. Mater., 45 (2009) 1226-1229.
[72] R. Blachnik, Thermodynamische Eigenschaften von IV–VI-Verbindungen: Bleichalkogenide / Thermodynamic Properties of IV–VI-Compounds: Leadchalcogenides, Z. Naturforsch. B, 29 (1974).
[73] H. Wang, Y. Pei, A.D. LaLonde, G.J. Snyder, Weak electron–phonon coupling contributing to high thermoelectric performance in n-type PbSe, Proceedings of the National Academy of Sciences, 109 (2012) 9705-9709.
[74] J.P. Issi, J. Heremans, M.S. Dresselhaus, Electronic and lattice contributions to the thermal conductivity of graphite intercalation compounds, Physical Review B, 27 (1983) 1333-1347.
[75] J.Q. Li, X.X. Li, F.S. Liu, W.Q. Ao, H.T. Li, Enhanced thermoelectric properties of (PbTe)0.88(PbS) 0.12 Composites by Sb Doping, J. Electron. Mater., 42 (2013) 366-371.
[76] S.N. Girard, K. Schmidt-Rohr, T.C. Chasapis, E. Hatzikraniotis, B. Njegic, E.M. Levin, A. Rawal, K.M. Paraskevopoulos, M.G. Kanatzidis, Analysis of Phase Separation in High Performance PbTe–PbS Thermoelectric Materials, Adv. Funct. Mater., 23 (2013) 747-757.
[77] J. Luo, L. You, J. Zhang, K. Guo, H. Zhu, L. Gu, Z. Yang, X. Li, J. Yang, W. Zhang, Enhanced Average Thermoelectric Figure of Merit of the PbTe–SrTe–MnTe Alloy, ACS Appl. Mater. Interfaces, 9 (2017) 8729.
[78] Y. Pei, G. Tan, D. Feng, L. Zheng, Q. Tan, X. Xie, S. Gong, Y. Chen, J.F. Li, J. He, M.G. Kanatzidis, L.D. Zhao, Integrating Band Structure Engineering with All-Scale Hierarchical Structuring for High Thermoelectric Performance in PbTe System, Adv. Energy Mater., 7 (2017) 1601450.
[79] H. Jiaqing, A. John, G.K. Mercouri, P.D. Vinayak, Seeing Is Believing: Weak Phonon Scattering from Nanostructures in Alkali Metal-Doped Lead Telluride, Nano Lett., 12 (2012).
[80] J. He, S.N. Girard, M.G. Kanatzidis, V.P. Dravid, Microstructure-Lattice Thermal Conductivity Correlation in Nanostructured PbTe0.7S0.3 Thermoelectric Materials, Adv. Funct. Mater., 20 (2010) 764-772.
[81] S.-H. Lo, J. He, K. Biswas, M.G. Kanatzidis, V.P. Dravid, Phonon Scattering and Thermal Conductivity in p-Type Nanostructured PbTe-BaTe Bulk Thermoelectric Materials, Adv. Funct. Mater., 22 (2012) 5175-5184.
[82] S. LeBlanc, Thermoelectric generators: Linking material properties and systems engineering for waste heat recovery applications, Sustainable Materials and Technologies, 1-2 (2014) 26-35.
[83] S. Aminorroaya Yamini, T. Li, D.R.G. Mitchell, J.M. Cairney, Elemental distributions within multiphase quaternary Pb chalcogenide thermoelectric materials determined through three-dimensional atom probe tomography, Nano Energy, 26 (2016) 157-163.
[84] S. Aminorroaya Yamini, D. Mitchell, M. Avdeev, In-situ characterisation of nanostructured multiphase thermoelectric materials at elevated temperatures, Phys. Chem. Chem. Phys., (2016).
[85] M. Zhou, J.-F. Li, T. Kita, Nanostructured AgPbmSbTem+2 System Bulk Materials with Enhanced Thermoelectric Performance, Journal of the American Chemical Society, 130 (2008) 4527-4532.
[86] L.-D. Zhao, J. He, C.-I. Wu, T.P. Hogan, X. Zhou, C. Uher, V.P. Dravid, M.G. Kanatzidis, Thermoelectrics with Earth Abundant Elements: High Performance p-type PbS Nanostructured with SrS and CaS, Journal of the American Chemical Society, 134 (2012) 7902-7912.

[87] A.J. Crocker, B.F. Dorning, Diffusion of sodium in lead telluride, Journal of Physics and Chemistry of Solids, 29 (1968) 155-161.
[88] B. Qiu, H. Bao, G. Zhang, Y. Wu, X. Ruan, Molecular dynamics simulations of lattice thermal conductivity and spectral phonon mean free path of PbTe: Bulk and nanostructures, Computational Materials Science, 53 (2012) 278-285.
[89] H. Wang, J. Wang, X. Cao, G.J. Snyder, Thermoelectric alloys between PbSe and PbS with effective thermal conductivity reduction and high figure of merit, J. Mater. Chem. A, 2 (2014) 3169-3174.
[90] W. Heng, D.L. Aaron, P. Yanzhong, G.J. Snyder, The Criteria for Beneficial Disorder in Thermoelectric Solid Solutions, Adv. Funct. Mater., 23 (2013).
[91] L. Ratke, P.W. Voorhees, Growth and Coarsening: Ostwald Ripening in Material Processing, Springer, 2002.
[92] R.W. Balluffi, 6 - Grain Boundary Diffusion Mechanisms in Metals* A2 - MURCH, GRAEME E, in: A.S. Nowick (Ed.) Diffusion in Crystalline Solids, Academic Press, 1984, pp. 319-377.
[93] D. Shaw, Atomic Diffusion in Semiconductors, Springer US, 2012.
[94] J. Friedel, CHAPTER X - ANNEALING, POLYGONIZATION, RECRYSTALLIZATION, GRAIN BOUNDARIES, Dislocations, Pergamon, 1964, pp. 275-302.
[95] J.W. Martin, J.W. Martin, R.D. Doherty, B. Cantor, Stability of Microstructure in Metallic Systems, Cambridge University Press, 1997.
[96] D. Wu, L.-D. Zhao, F. Zheng, L. Jin, M.G. Kanatzidis, J. He, Understanding Nanostructuring Processes in Thermoelectrics and Their Effects on Lattice Thermal Conductivity, Adv. Mater., 28 (2016) 2737-2743.
[97] J. He, M.G. Kanatzidis, V.P. Dravid, High performance bulk thermoelectrics via a panoscopic approach, Materials Today, 16 (2013) 166-176.
[98] Y.-J. Kim, L.-D. Zhao, M.G. Kanatzidis, D.N. Seidman, Analysis of Nanoprecipitates in a Na-Doped PbTe–SrTe Thermoelectric Material with a High Figure of Merit, ACS Applied Materials & Interfaces, 9 (2017) 21791-21797.
[99] K. Biswas, J. He, I.D. Blum, C.-I. Wu, T.P. Hogan, D.N. Seidman, V.P. Dravid, M.G. Kanatzidis, High-performance bulk thermoelectrics with all-scale hierarchical architectures, Nature, 489 (2012) 414-418.
[100] Q. Zhang, B. Liao, Y. Lan, K. Lukas, W. Liu, K. Esfarjani, C. Opeil, D. Broido, G. Chen, Z. Ren, High thermoelectric performance by resonant dopant indium in nanostructured SnTe, Proc. Natl. Acad. Sci. U.S.A., 110 (2013) 13261-13266.
[101] R.J. Cava, H. Ji, M.K. Fuccillo, Q.D. Gibson, Y.S. Hor, Crystal structure and chemistry of topological insulators, J. Mater. Chem. C, 1 (2013) 3176-3189.
[102] J.R. Drabble, C.H.L. Goodman, Chemical bonding in bismuth telluride, Journal of Physics and Chemistry of Solids, 5 (1958) 142-144.
[103] A.J. Schwartz, M. Kumar, B.L. Adams, D.P. Field, Electron Backscatter Diffraction in Materials Science, Springer US, 2010.
[104] A.W. Wilson, J.D. Madison, G. Spanos, Determining phase volume fraction in steels by electron backscattered diffraction, Scripta Mater., 45 (2001) 1335-1340.
[105] J. Wu, P.J. Wray, C.I. Garcia, M. Hua, A.J. Deardo, Image Quality Analysis: A New Method of Characterizing Microstructures, ISIJ Int., 45 (2005) 254-262.
[106] J. Wu, P.J. Wray, C.I. Garcia, M. Hua, A.J. DeArdo, On Achieving a Better Understanding of the Polygonal Ferrite Microstructure in IF Steel Using Image Quality Analysis, Mater. Manuf. Processes, 22 (2007) 281-285.
[107] A.W. Wilson, G. Spanos, Application of orientation imaging microscopy to study phase transformations in steels, Mater. Charact., 46 (2001) 407-418.
[108] A.A. Gazder, F. Al-Harbi, H.T. Spanke, D.R. Mitchell, E.V. Pereloma, A correlative approach to segmenting phases and ferrite morphologies in transformation-induced plasticity steel using electron back-scattering diffraction and energy dispersive X-ray spectroscopy, Ultramicroscopy, 147 (2014) 114-132.
[109] R. Srinivasan, K. McReynolds, N.W. Gothard, J.E. Spowart, Texture development during deformation processing of the n-type bismuth telluride alloy Bi2Se0.3Te2.7, Materials Science and Engineering: A, 588 (2013) 376-387.
[110] A.A. Gazder, M. Sánchez-Araiza, J.J. Jonas, E.V. Pereloma, Evolution of recrystallization texture in a 0.78 wt.% Cr extra-low-carbon steel after warm and cold rolling, Acta Mater., 59 (2011) 4847-4865.

[111] D.R.G.M. Mitchell, Scripting Resources for DigitalMicrograph, 2017.
[112] Z. Wang, X. Yang, D. Feng, H. Wu, J. Carrete, L.-D. Zhao, C. Li, S. Cheng, B. Peng, G. Yang, J. He, Understanding Phonon Scattering by Nanoprecipitates in Potassium-Doped Lead Chalcogenides, ACS Applied Materials & Interfaces, 9 (2017) 3686-3693.